11-7-2016

Experimental and Computational Study on Fracture Mechanics of Multilayered Structures

Hai Thanh Tran
University of South Florida, tranthanhhai_hanoi@yahoo.com

Experimental and Computational Study on Fracture Mechanics of Multilayered Structures

by

Hai Thanh Tran

A dissertation submitted in partial fulfillment
of the requirements for the degree of
Doctor of Philosophy
Department of Mechanical Engineering
College of Engineering
University of South Florida

Co-Major Professor: Wenjun Cai, Ph.D.
Co-Major Professor: Alex Volinsky, Ph.D.
Manh-Huong Phan, Ph.D.
Nathan Crane, Ph.D.
Alex Savachkin, Ph.D.

Date of Approval:
October 20, 2016

Keywords: Al-Mn alloy, thin film, polymer substrate, multilayer, fracture toughness, finite element simulation

DEDICATION

To my parents, especially my moms Hien Nguyen and Anh Hoang. Without their continuous and unconditional love and support, I would not have it. Words cannot express how grateful I am to them.

To my beloved wife and best friend Giang Ngo. She has been an unlimited source of love, support, encouragement and sympathy during this tough and long process.

To my beautiful children, Khang Tran and Vy Tran, who are my unlimited source of joy and happiness.

ACKNOWLEDGEMENTS

First, I would like to express my special appreciation and thanks to my co-advisor Professor Wenjun Cai for all of her guidance and advice during my Ph.D. Even though there were hard times, she was continuously supporting and being patient to me. I really appreciate all her contributions of time and funding of my study and research.

Second but not less important, I am so grateful to my co-advisor Professor Alex Volinsky. He is the one who helped enroll me in this program and rooted for me not only on campus but also in many other aspects of life. Especially, working under his instruction made me much more confident in research and writing papers.

Third, I would like to express special thanks to Professor Manh-Huong Phan. He has been always making himself available for any questions and concerns that I have had. The enthusiasm and joy he has towards science and research have motivated me so much.

I would also like to express my sincere gratitude to the other committee members Professor Nathan Crane and Professor Alex Savachkin, and the chair person of the defense Professor Dario Arena. They kindly spent their time for my dissertation.

Special thanks to my fellow lab-mate, Hesham Mraied, for being willing to give me help anytime I needed it. His knowledge and experimental skills have contributed significantly to my experimental results. I also want to thank Richard Everly for giving me trainings and help when I was doing experiments in NREC; Professor Ashok Kumar for kindly letting me use his lab and equipment.

Finally, I would like to acknowledge financial supports from Mechanical Engineering department of the University of South Florida and from the Vietnamese government.

TABLE OF CONTENTS

LIST OF TABLES

LIST OF FIGURES

ABSTRACT

Many devices in electronics are in the form of multilayered structures. These structures can fail catastrophically if they contain defects or cracks. Enhancing their fracture properties is therefore critical to improve the reliability of the systems. The interface-dominated fracture mechanics of multilayered structure was studied using experiments and finite element (FE) modeling by considering two examples: thin films on polymer substrates in flexible electronics and Cu leadframe/epoxy molding compound (EMC) in micro-electronics packaging.

In the first example, aluminum-manganese (Al-Mn) thin films with Mn concentration up to 20.5 at.% were deposited on polyimide (PI) substrates. A variety of phases, including supersaturated fcc (5.2 at.% Mn), duplex fcc and amorphous (11.5 at.% Mn), and completely amorphous phase (20.5 at.% Mn) were obtained by adjusting alloying concentration in the film. In comparison with crystalline and dual phase counterparts, the amorphous thin film exhibits the highest fracture stress and fracture toughness, but limited elongation. Based on a fracture mechanism model, a multilayer scheme was adopted to optimize the ductility and the fracture properties of the amorphous film/PI system. Tensile deformation and subsequent fracture of strained Al-Mn films on PI were investigated experimentally and by FE simulations. It was found that by sandwiching the amorphous film (20.5 at.% Mn) between two ductile copper (Cu) layers, the elongation can be improved by more than ten times, and the interfacial fracture toughness by twenty four times with a limited sacrifice of the film's fracture toughness (less than

18%). This design provides important guidelines to obtain optimized mechanical properties of future flexible electronics devices.

The reliability of amorphous brittle Al-Mn (20.5 at.% Mn) thin films deposited on PI substrates is strongly influenced by the film/substrate interface adhesion. Some strategies to improve the adhesion of the interface were conducted, including roughening the surface of the PI substrate, adding a buffer layer and then tuning its thickness. Tensile testing and FE analysis of amorphous Al-Mn thin films with and without buffer layers coated on intact and plasma etched rough PI were investigated. It was found that by adding a chromium buffer layer of 75 nm on a rough PI substrate, the interface adhesion of the film/substrate can increase by almost twenty times. The obtained results would thus shed light on the interfacial engineering strategies for improving interface adhesion for flexible electronics.

In the second example, a systematic investigation and characterization of the interfacial fracture toughness of the bimaterial Cu leadframe/EMC was carried out. Experiments and FE simulations were used to investigate delamination and interfacial fracture toughness of the biomaterial system. Two dimensional simulations using computational fracture mechanics tools, such as virtual crack closure technique, virtual crack extension and J-integral proved to be computationally cheap and accurate to find the interfacial fracture toughness of the bimaterial structures. The effects of temperature, moisture diffusion and mode-mixity on the interfacial fracture toughness were investigated. Testing temperature and moisture exposure significantly reduce the interfacial fracture toughness, and its relationship with the mode-mixity was achieved by fitting the results with an analytic formula.

CHAPTER 1: INTRODUCTION

1.1 Background and Motivation

Fracture mechanics, as compared to traditional mechanics of solids approach, has gained great interest of mechanical designers and engineers because the failure can occur catastrophically when structures contain defects or cracks arising from manufacturing process or in service. In these cases, the consequences can be fatal. Many crack-related catastrophes were reported in automobiles, construction, ships, aeronautics, electronic devices, etc. Defects in electronics devices are inevitable because, together with production defects, most of the devices contain geometrical discontinuities, such as interfaces (i.e. a boundary between two dissimilar materials) and threaded connections, which are natural sources for crack initiation and propagation. While the study of microscopic and crystallographic defects of materials may inform about the origin of defect nucleation, fracture mechanics, on the other hand, is needed to elucidate the driving force of crack nucleation and propagation.

This dissertation focuses on studying the fracture mechanics of structures containing multiple layers of various materials. Layered structures are increasingly used in a wide variety of applications due to the ability to tailoring their specific properties through design and fabrication. While mechanical properties of bulk materials can be controlled through their micro-structures such as crystal structures, the mechanical properties of layered structures such as thin films on polymer substrates in flexible electronics or Cu leadframe/EMC in micro-electronics packaging are sensitive to interfaces. Fracture mechanisms of multilayered structures are different from the

bulk materials due to the geometrical constraint (e.g. interfaces) and mechanical properties mismatches. Therefore, the determination of the mechanical properties, such as critical strain, fracture strength, and interface fracture toughness of the systems is not just a straightforward extension of bulk counterparts. For example in thin films coated on substrates, together with the deformation caused by dislocation motion which is similar to bulk materials, the high ratio of surface to volume results in additional barriers for dislocation movement, which leads to higher strength of thin films compared to their bulk counterparts. One can find comprehensive reviews on this problem elsewhere (Evans et al. 1995; Hutchinson et al. 1991; Was et al. 1996). With the presence of interfaces, the fracture properties of multilayered structures can also be altered significantly. According to Was et al. (1996), plastic deformation has a strong effect on the fracture toughness of the interface in multilayered systems. A tough interface is normally attributed to extensive plastic work done at the crack tip during crack propagation. Therefore, materials with higher strength often exhibit higher fracture toughness. Nevertheless, the interfaces might affect the fracture toughness noticeably if the tensile strength of the material increases. For example, when the crack tip reaches the interface, the chance of the crack propagation strongly depends on how the stress at the crack tip is transferred to the other layer (Was et al. 1996). In addition, the interface may constrain the expansion of the plastic zone resulting in the increase in the stress at the crack tip. In another case, when the interface debonding (i.e. delamination) occurs, the stress at the crack tip is changed significantly resulting in the change in fracture resistance. Therefore, the reliability of such structures strongly depends on the interface adhesion.

As a specific example, interface-dominated fracture mechanics play significant role in the reliable performance of flexible electronic devices due to the large properties mismatch between

the metallic thin films and the flexible substrate underneath. Flexible electronics has gained great interest recently due to its potential applications such as wearable electronic devices (e.g. Fig. 1.1(a)) (Wagner et al. 2004), sensor skins (e.g. Fig. 1.1(b)) (Lumelsky et al. 2001), electronic textiles or smart textiles (e.g. Fig. 1.1(c)) (Bonderover et al. 2004), and flexible solar cells (e.g. Fig. 1.1(d)) (Brabec 2004), etc. In flexible electronics devices, where there typically exists a form of metallic interconnect thin films coated on polymer substrates, ductility mismatch between the films and flexible substrates have often led to limited elongation and fracture resistance, and thus hindering reliable performance of the system. While the polymer substrate can sustain a large elongation, metallic thin films themselves often fail at very small deformation, normally a few percent of strain. The situation is even worse when the metallic film is amorphous/glassy (e.g. Al-Mn alloy studied here) because of its intrinsic brittle properties due to lack of strain hardening mechanisms or any intrinsic crack propagation barriers, e.g. grain boundaries or secondary phase boundaries. When elongated, the glassy film cannot sustain the required co-deformation with the flexible substrate. Ameliorating this situation is requested, because compared with crystalline metallic materials, amorphous alloys have been proven to be outstanding candidates as functional materials due to their good metallic bonding ability (Chu et al. 2009; Inoue 2001; Wang 2009), excellent mechanical, corrosion (Chu et al. 2010; Moffat et al. 1993; Mraied et al. 2016a), and magnetic properties (McHenry et al. 1999; Phan et al. 2008). Therefore, understanding the fracture behavior of such systems is very important to increase the performance and reliability of flexible electronic devices. Such considerations have motivated the author to improve the mechanical properties of amorphous metal films coated on polymer substrates, focusing on optimizing the fracture toughness, interfacial adhesion and elongation.

Another example bearing similar consideration is the micro-electronic package systems, whose function is to provide a qualified surrounding environment for the electronics device. It includes powering, cooling down the device, as well as protecting the device from harmful environmental factors during service, such as heat, moisture, mechanical or chemical factors (Tummala 2001). Micro-electronic packages typically consist of multiple layers of materials with dissimilar physical properties. Stresses induced by mechanical and/or thermal loading can initiate and propagate interfacial debonding, especially near the free edges. Such interfacial delamination can lead to the multilayered micro-electronic package failure. For instance, Harries et al. (1999) studied interfacial delamination of very small peripheral packages by utilizing various methods to determine the ERR. Fan et al. (1999) performed numerical analysis of the delamination and cracking in the flip-chip modules, and proposed a criterion for predicting potential cracking sites. Hu et al. (1996) studied interfacial debonding of the multi-chip module thin film interconnects, and found that the debonding along the walls and polymer thin films can relieve thermal constraints, leading to a stress relaxation under thermal loading. Kamer et al. (2011) proposed a reliable, quantitative method for measuring adhesion of hard coatings on polymers. Among bimaterial systems used in micro-electronic packages, Cu leadframe and EMC (Fig. 1.2) is an important combination due to its widespread use. EMC is used to protect semiconductor chips from the external environment, such as physical forces, impact and pressure, chemical forces, moisture, heat, and ultraviolet rays, while electrically insulating the semiconductor devices (Komori et al. 2009). The importance of this system and its tendency to experience interfacial delamination has motivated the author to conduct a systematic investigation and characterization of interfacial fracture toughness of the bimaterial Cu leadframe/EMC system.

1.2 Organization of Dissertation

In this dissertation, the fracture behavior of multilayered structures was studied using experiments and computer simulations on two systems: brittle thin films (nanocrystalline and amorphous Al-Mn) coated on polymer substrate and Cu leadframe adhered to EMC. The chapters of the dissertation are organized as follows:

a. Chapter 2 - Fundamentals of fracture mechanics and computational methods in fracture mechanics

This chapter introduces fundamentals of fracture mechanics including some main approaches to find fracture toughness of materials and the corresponding fracture criteria. The approaches cover linear elastic as well as elasto-plastic materials. In addition, some cutting edge computational methods in fracture mechanics will be presented. Based on finite element method (FEM), those methods are mainly used to find energy release rates (ERR) or J-integrals and their corresponding critical values (i.e. fracture toughnesses) of the multilayerd materials.

b. Chapter 3 - Optimizing ductility and fracture properties of brittle metallic thin films on polymer substrates using multilayer schemes

Mechanical properties of Al-Mn alloys thin films (Al-5.2 at.% Mn, Al-11.5 at.% and Al-20.5 at.% Mn) coated on polyimide (PI) substrates, including critical strain, fracture stress and fracture toughness, were measured. Based on a fracture mechanism model, a multilayer scheme was adopted to optimize the ductility and the fracture properties of the amorphous Al-Mn alloy film/PI system by adding Cu buffer layers. The film's microstructure and composition were characterized using scanning electron microscopy (SEM), energy dispersive spectra (EDS), transmission electron microscopy (TEM), and selected area diffraction (SAD). Tensile stress-strain behavior (strain measured using digital image correlation (DIC) method) and fracture

properties of strained monolithic and multilayer films on PI were investigated experimentally and by finite element (FE) simulations. The most beneficial finding of this chapter is that by sandwiching the amorphous film (20.5 at.% Mn) between two ductile Cu layers, its ductility can be improved by more than ten times, and interfacial fracture toughness by twenty four times with a limited sacrifice of fracture toughness.

c. Chapter 4 - Effects of substrate roughness and buffer layer properties on the interface adhesion of brittle thin films on PI substrates

In this chapter, strategies including roughening the substrate, adding a buffer layer (Al or Cr) and tuning its thickness were conducted to improve the adhesion of the interface of brittle Al-Mn thin films deposited on PI substrates. Tensile tests of the thin films with and without buffer layers coated on intact and plasma etched rough PI were conducted experimentally and by FE simulations. The most beneficial finding of this chapter is that by adding a Cr buffer layer of 75 nm on a rough PI substrate of 100 nm Ra, the interface adhesion of the film/substrate can increase by almost twenty times.

d. Chapter 5 - Temperature, moisture and mode-mixity effects on Cu leadframe/epoxy molding compound interfacial fracture toughness

This chapter characterizes the fracture toughness of the interface of Cu leadframe/EMC. The temperature dependence of the interfacial fracture toughness of the structure was investigated using four point bending delamination (4PB) tests. In addition, with the use of four point-bend end-notched flexure (4ENF) tests, the effects of moisture diffusion and mode-mixity on interfacial fracture toughness were also studied. Together with the experimental critical force, some methods of finding ERR, including analytical and computational methods, such as virtual

crack closure technique (VCCT), virtual crack extension (VCE) and J-integral were used to get the results.

1.3 Tables and Figures

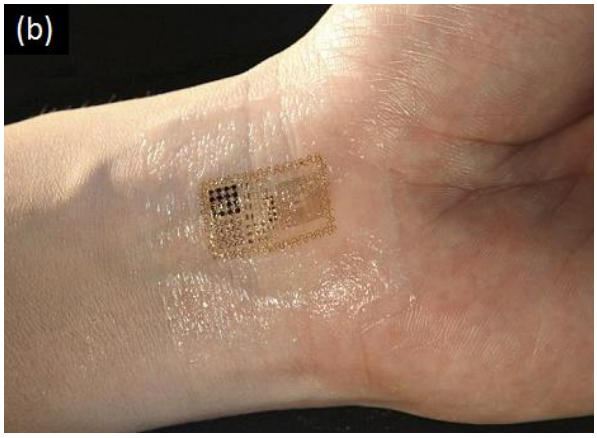

Figure 1.1 Flexible electronics applications.
(a) Philips fluid smartphone. Credit: https://wordlesstech.com/philips-fluid-smartphone/,
(b) Sensor skins to monitor a patient's vital signs such as temperature and heart rate. Credit: http://www.dailymail.co.uk/sciencetech/article-2025102/Electronic-skin-How-hi-tech-tattoo-monitor-patients-vital-signs.html,
(c) Electronic textiles. Credit: http://www.ife.ee.ethz.ch/research/groups/PlasticElectronics/,
(d) Flexible solar cells. Credit: https://www.cnet.com/news/solopower-rolls-out-flexible-rooftop-solar-panels/. All the figures are in public domain.

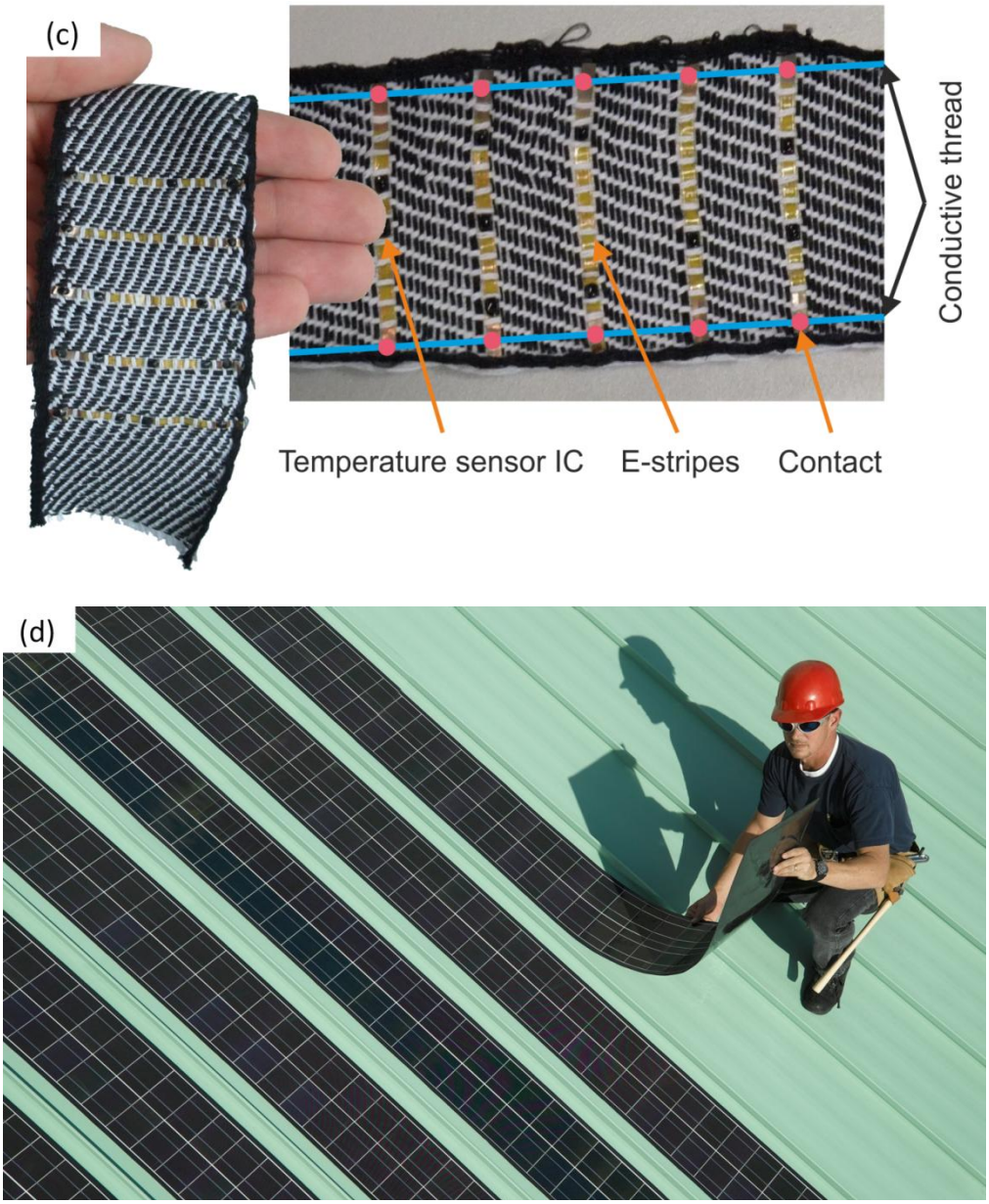

Figure 1.1 (continued).

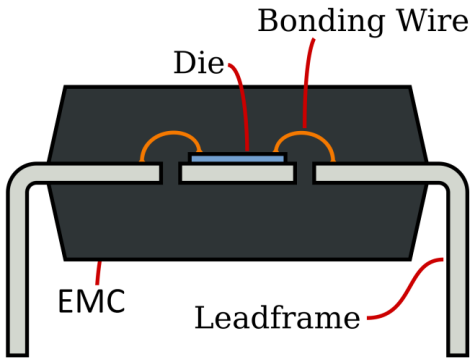

Figure 1.2 Cu leadframe/EMC in an integrated circuit package. Adapted from https://en.wikipedia.org/wiki/Dual_in-line_package, which is in public domain.

CHAPTER 2: FUNDAMENTALS OF FRACTURE MECHANICS AND COMPUTATIONAL METHODS IN FRACTURE MECHANICS

2.1 Introduction

Most of engineering components and structures contain geometry discontinuities, such as teeth roots of gear wheels, keyways in shafts and interfaces between dissimilar materials. The size and shape of the discontinuities are critical because they determine the fracture strength of the parts. Conventional treatment of structure failure often considers the interplay of two factors: applied stress and either yield strength or tensile strength of the material. However, this conventional approach gives erroneous results if the geometry discontinuity features have sharp radii. To explain this point, let's consider the following cases in the Fig. 2.1 (Wang 1996). Assuming equal thickness of all samples, their fracture forces are arranged in the following order: F4 < F3 < F1 < F2. Clearly, the sizes of the defects in samples C and D are crucial to the fracture strength of the structures.

Fracture mechanics is the study of the initiation and propagation of cracks in materials. In comparison with the s*trength of material approach*, fracture mechanics approach considers three factors, including applied stress, flow size and fracture toughness of the material. In this approach, the fracture toughness replaces yield strength (or tensile strength) as the relevant material property. Fracture mechanics quantifies the critical combinations of these three parameters (Anderson 2005). Fig. 2.2 shows the difference between fracture mechanics approach and strength of materials approach.

Fracture mechanics can be divided into *linear elastic fracture mechanics* (LEFM) and e*lasto-plastic fracture mechanics* (EPFM). LEFM gives excellent results for brittle elastic materials, such as amorphous metallic alloys, high-strength steel, glass and concrete. However, for ductile materials, such as low-carbon steel, some certain aluminium alloys, polymers, plastic deformation always precedes fracture and then EPFM is needed. Nonetheless, when the load is low enough, LEFM is still a good choice since it continues to provide an acceptable approximation to the physical problems. The family tree of fracture mechanics can be seen in Fig. 2.3 (Anderson 2005). Within fracture mechanics, there are two alternative (sub-) approaches: *energy criterion approach* and *stress intensity approach*, which will be considered in the next section.

This chapter does not intend to cover all aspects of fracture mechanics but focuses on some key parameters (i.e. fracture toughness and the equivalent terms), which are feasible to be obtained computationally and corresponding fracture criteria in the field, which are used to predict the crack initiation and propagation. These parameters are SIF K (critical value of K is fracture toughness of elastic materials), ERR G (critical value of G is an equivalent term for fracture toughness of elastic materials) and J-integral (critical value of J-integral is fracture toughness of elastic-plastic materials). Other key parameters used in fracture mechanics such as crack tip opening displacement (CTOD, used for elastic-plastic materials) and the crack tip opening angle (CTOA, used for elastic-plastic materials, but mostly applied in thin-walled structures in pipeline and aircraft engineering), can be found elsewhere (Anderson 2005; Cotterell 2002; Erdogan 2000; Horsley 2003; Newman Jr et al. 2003; Wells 1963; Zerbst et al. 2009; Zhu et al. 2012).

2.2 Fracture Criteria

2.2.1 Stress Intensity Approach

a. Stress intensity factor

In fracture mechanics, stress intensity factor (SIF) K is used to accurately determine the stress state (i.e. stress intensity) near the crack tip caused by external loads or residual stresses. For a linear elastic material, the stress field near a crack tip can be expressed as a product of $\frac{1}{\sqrt{r}}$ and a function of θ (where r is radial coordinate and θ is angular coordinate) with a scaling factor K (Anderson 2005):

$$\lim_{\gamma \to 0} \sigma_{ij}^{(I)} = \frac{K_I}{\sqrt{2\pi r}} f_{ij}^{(I)}(\theta), \tag{2.1}$$

$$\lim_{\gamma \to 0} \sigma_{ij}^{(II)} = \frac{K_{II}}{\sqrt{2\pi r}} f_{ij}^{(II)}(\theta), \tag{2.2}$$

$$\lim_{\gamma \to 0} \sigma_{ij}^{(III)} = \frac{K_{III}}{\sqrt{2\pi r}} f_{ij}^{(III)}(\theta), \tag{2.3}$$

where the superscripts and subscripts *I*, *II*, and *III* denote three different fracture modes (Mode I is opening or tensile mode, where the crack surfaces move directly apart. Mode II is sliding or in-plane shear mode in which the crack surfaces slide to each other perpendicular to the crack edge. Mode III is out-of-plane shear mode, or tearing mode, where the crack surfaces move relative to one another and parallel to the leading edge of the crack). For linear elastic materials, the principle of superposition applies. A mixed-mode problem can be obtained by summarizing each mode (Anderson 2005):

$$\sigma_{ij}^{(total)} = \sigma_{ij}^{(I)} + \sigma_{ij}^{(II)} + \sigma_{ij}^{(III)}. \tag{2.4}$$

Therefore, the stress distribution at the crack tip will be obtained if the constants K_i are known. The SIFs K_i (K_I, K_{II}, K_{III}) include the external loads (σ_{ij}) and the geometries, i.e. the crack's size and the shape ($f_{ij}(\theta)$).

In practice, maximum stress at the crack tip will be calculated and engineers' duty is to ensure that it does not exceed the fracture toughness of the materials. For that purpose, SIF *K* is expressed in terms of stresses σ at $r \to 0$ and $\theta = 0$. For example, for a through crack appearing in an infinite plate under uniform tensile stress σ, the SIF *K* is presented and shown in the Fig. 2.4, where *a* is one half of the width of the through crack. The unit of K is:

$$Dim[K] = \frac{F}{L^2}\sqrt{L} = Stress.\sqrt{Length}\,. \tag{2.5}$$

For some simple configurations, closed-form analytical formulas of the SIF K were derived and can be found in fracture mechanics textbooks.

b. K_C as fracture toughness of materials and the first fracture criterion

In theory, the stress at the crack tip is singular (i.e. infinity) but in practice there is always a plastic zone around the crack tip that impedes the stress to reach the infinite value. It is very difficult to determine the actual stress state in the plastic zone around the crack tip and compare it to the allowable strength of the material to determine whether a crack initiates (and propagates) or not. Having done a series of experiments, one can determine the critical SIF K_C for each material. K_C is a material property, i.e. the material's resistance to fracture, and is called *fracture toughness of the material* which is used to determine the crack stability. Fracture occurs when $K_i \geq K_{Ci}$ (i = I, II, III) and at the moment of fracture: $K_i = K_{Ci}$ (Anderson 2005).

2.2.2 Energy Criterion Approach

a. Energy balance during a crack growth

The difference between a cracked body and an un-cracked body is obviously the additional surface associated with the crack. It is well known that creating new surfaces (crack) consumes energies since surfaces carry higher energy than the body. It then follows that whether or not a cracked body remains stable or becomes unstable depends on whether it contains sufficient energy to create additional surfaces while still maintaining its equilibrium (Anderson 2005). According to the law of conservation of energy the work performed per unit time by the applied loads ($\dot{W}$) must be equal to the rates of change of the internal elastic energy ($\dot{U}_E$), plastic energy ($\dot{U}_P$), kinetic energy ($\dot{K}$) of the body, and the energy required to increase the crack length per unit time ($\dot{\Gamma}$). In other words (Wang 1996):

$$\dot{W} = \dot{U}_E + \dot{U}_P + \dot{K} + \dot{\Gamma}. \tag{2.6}$$

If the crack grows slowly, the kinetic energy K is negligible ($\dot{K} = 0$). Moreover, because all changes with respect to time are caused by changes in crack size:

$$\frac{\partial}{\partial t} = \frac{\partial}{\partial A}\frac{\partial A}{\partial t} = \dot{A}\frac{\partial}{\partial A}, \tag{2.7}$$

where A presents the crack area. Therefore equation (2.6) can be rewritten as:

$$-\frac{\partial \Pi}{\partial A} = \frac{\partial U_P}{\partial A} + \frac{\partial \Gamma}{\partial A}, \tag{2.8}$$

where $\Pi = U_E - W$ is the potential energy of the system. The equation (2.8) means that the reduction in potential energy equals to the energy dissipated in plastic energy and surfaces creation (Wang 1996).

b. Griffith's theory

For an ideally brittle material (linear elastic material), the energy dissipated in plastic deformation is negligible and it can be ignored ($\dot{U}_P = 0$). Therefore, for linear elastic materials, a crack extension force per unit of crack area G can be defined from equation (2.8) (Anderson 2005):

$$G = -\frac{\partial \Pi}{\partial A} = \frac{\partial \Gamma}{\partial A}. \tag{2.9}$$

The equilibrium equation (2.9) means that potential energy must be sufficient in the body to overcome the surface energy of the material (energy required to increase the crack). G is also called *elastic energy release rate* or *energy release rate* (ERR) or *strain energy release rate*.

According to linear elasticity theory, a body under constant applied loads obeys Clapeyron's theorem (Fosdick et al. 2003):

$$W = 2U_E \tag{2.10}$$

and associated with (2.6) (and $\dot{K} = 0$), hence, the equation (2.9) can be rewritten as:

$$G = \frac{\partial U_E}{\partial A}. \tag{2.11}$$

The physical meaning of the ERR G is that it characterizes the amount of energy per unit area that would be released if the crack advances. It should be pointed out that the equation is correct only when the cracked body behaves *linearly*. If the body behaves *nonlinear elastic* or *considerable plasticity*, the equation is no longer valid and hence the original equation (2.8) should be used instead.

c. G_C - critical energy release rate of materials and the second fracture criterion

The energy approach states that crack extension (fracture) occurs when the energy available for crack growth is greater than the resistance of the material. In other words, a fracture

occurs when $G \geq G_C$ - the *critical ERR* which is a measure of fracture toughness of the material. Therefore, G_C is also a material property - the material's resistance to fracture. At the moment of fracture: $G = G_C$.

2.2.3 J-integral - a Nonlinear Approach

a. J-integral

The above two methods of finding the ERR are for elastic materials only. For nonlinear elastic and elasto-plastic materials, another approach is needed to analyse the facture. J-integral was first introduced by (Rice 1988), due to the difficulties involved in computing the stresses close to the crack in nonlinear elastic or elastic-plastic materials. It was shown by (Anderson 2005) that if a monotonic loading is assumed (without any plastic unloading), the J-integral is a path-independent line integral and it represents the strain ERR of nonlinear elastic and elasto-plastic materials:

$$J = -\frac{d\Pi}{dA}, \tag{2.12}$$

where $\Pi = U_E - W$ is the potential energy, the elastic strain energy U_E stored in the body minus the work W done by external forces and A is the crack area. In practice, J-integral is defined as (Anderson 2005):

$$J = \int_\Gamma w dy - T_i \frac{\partial u_i}{\partial x} ds, \tag{2.13}$$

where $w = \int_0^{\varepsilon_{ij}} \sigma_{ij} d\varepsilon_{ij}$ is the strain energy density, $T_i = \sigma_{ij} n_j$ is the traction vector, Γ is an arbitrary contour around the tip of the crack as shown in the Fig. 2.6, n is the unit vector normal to Γ, and σ, ε, u are the stress, strain and displacement field, respectively. The dimension of J is:

$$Dim[J] = \frac{F}{L^2} L = \frac{Energy}{Area}. \tag{2.14}$$

b. J_C as fracture toughness of materials and the third fracture criterion

The same as the above mentioned two criteria, the crack propagates when $J \geq J_C$ - critical J-integral or elasto-plastic failure parameter. Critical J-integral is called elasto-plastic fracture toughness. At the moment of fracture: $J = J_C$.

2.2.4 Relationship Between *K*, *G* and J-integral

For linear elastic materials, J-integral is, in fact, the strain ERR G, and both are related to the SIF K in the following fashion (Anderson 2005):

$$J = G = \begin{cases} \dfrac{K^2}{E} & (1) \\ \dfrac{K^2}{E}(1-\nu^2) & (2) \end{cases} \tag{2.15}$$

(1) is for the case of Plane stress and (2) is for Plane strain. The same relationship obviously holds for K_C and G_C. Therefore, the three approaches are equivalent for isotropic linear elastic materials.

2.2.5 Mode-Mixity of an Interface Delamination

Interfacial delamination is of an important concern for multilayered electronics devices, as it is one of the most common failures observed after reliability tests. Fracture mechanics has, quite reasonably, been developed for simple fractures in homogeneous, isotropic materials. For inhomogeneous, anisotropic materials such as bilayered materials an extra characterisation is required.

It is believed that Williams (1959) first conducted the theoretical investigation of interfacial crack problems by using the asymptotic analysis for an interfacial crack between two isotropic elastic materials. Opposite to homogeneous, isotropic materials where cracks tend to

propagate in pure mode I locally at the crack tip, *mode-mixity* ψ (Fig. 2.7) is a critical parameter for interfacial fracture. The mode-mixity (also called the *phase angle of fracture* or *loading phase angle*) is the relative proportion of tractions ahead of the crack tip in mode II and mode I in the facture (ψ = 0 leads to mode I loading, ψ = $\pi/2$ leads to mode II loading). A crack constrained in an interface is subjected to mixed mode conditions and propagates when the preferred fracture path is in the interface. It is shown that interfacial fracture toughness depends strongly on the mode-mixity (Evans et al. 1990; Wang et al. 1990). In general, the total fracture toughness increases as the mode II contribution increases. The delamination propagates when, for a given mode-mixity, the calculated ERR G exceeds the interlaminar fracture toughness G_C (critical strain ERR).

Mode-mixity can be determined using a SIF-based approach or can be based on the components of the ERRs, which is used in this work. The mode-mixity based on ERRs, ψ_G for a crack in homogeneous isotropic materials is calculated by the components of the ERR with respect to mode I and mode II as in the formula (Agrawal et al. 2006):

$$\tan^2 \psi_G = \frac{G_{II}}{G_I}. \tag{2.16}$$

For an interface crack, the decomposed components of the ERR, hence the mode-mixity, ψ_G, depend on the crack extension size, Δ. However, when ε, which is a bimaterial constant defined in (Agrawal et al. 2006), is small, the oscillatory character can be ignored.

2.3 Computational Methods in Fracture Mechanics

Although analytical expressions for the total ERR are available for some simple interfacial crack problems (Cherepanov 1979; Hutchinson et al. 1991), they involve considerable mathematical complexity. For complicated geometries or loading conditions, the analytical

expressions may not be available; hence the problem needs to be solved numerically. Moreover, computational solutions can save time and money spent on experiments. Thus, in practice, computational methods are preferred in many cases.

The total ERR can be obtained through numerical computation using FE based techniques, such as VCCT, VCE, J-integral, etc. However, only VCCT provides information about the mode-mixity (i.e. it can give the components of the ERR).

2.3.1 Virtual Crack Closure Technique

VCCT for ERR calculation was originally proposed in 1977 by Rybicki and Kanninen, based on Irwin's crack closure integral (Irwin 1957). Although the VCCT has significant advantages over other methods, it has not been developed in most of the large general-purpose FE codes (e.g. Ansys APDL). Let's examine a two-dimensional sample.

a. Crack closure method - two analysis steps

Before going to the investigation of the VCCT, it is appropriated to investigate a method called crack closure method or two-step virtual crack closure technique. According to Krueger (2004), the method is based on the assumption that the energy $-\Delta\Pi$ released when the crack is extended (or the work $\Delta\Gamma$ required to increase the crack as shown in the formula (2.9)) by Δa from a (Fig. 2.8) to $a + \Delta a$ (Fig. 2.9) is identical to the energy required to close the crack between location l and i. Index "1" denotes the first step depicted in Fig. 2.8 and index "2" the second step as shown in Fig. 2.9. For a crack modelled with two-dimensional four noded elements, the work $-\Delta\Gamma$ required to close the crack along one element side can be calculated as (Krueger 2004):

$$-\Delta\Gamma = \frac{1}{2}\left[X_{1l}.\Delta u_{2l} + Z_{1l}.\Delta w_{2l}\right], \tag{2.17}$$

noted that $-\Delta\Pi = \Delta\Gamma$. Here, X_1 and Z_1 are the shear and opening forces, respectively, measured at the nodal point l to close the crack (Fig. 2.8) and u_{2l} and w_{2l} are the shear and opening displacements at node l (Fig. 2.9). The crack closure method creates the original state before the crack extension. Hence, the forces needed to close the crack surfaces are identical to the ones acting on the surfaces of the closed crack. The forces X_{1l} and Z_{1l} are determined from the first FEA in which the crack is closed. The relative displacements u_2 and w_2 are determined from the second FEA in which the crack reaches the length of $a + \Delta a$.

b. Virtual crack closure technique - a one step modified crack closure method

VCCT is a modification of the crack closure method. In VCCT, the crack extension of Δa from a $+\Delta a$ (node i) to $a + 2\Delta a$ (node k) is assumed not make any remarkable change to the state of the crack tip (Fig. 2.10). Therefore, the displacements behind the crack tip at node i are approximately equal to the displacements behind the original crack tip at node l. Moreover, during the crack extension from $a + \Delta a$ to $a + 2\Delta a$, the energy $-\Delta\Pi$ released is exactly the same to the energy required to close the crack. That is between the nodes i and k. If the crack was simulated by two-dimensional, four-noded elements (Fig. 2.10), the work $-\Delta\Gamma$ needed to close the crack (along one element side), will be determined (Krueger 2004):

$$-\Delta\Gamma = \frac{1}{2}\left[X_i.\Delta u_l + Z_i.\Delta w_l\right], \tag{2.18}$$

noted that $-\Delta\Pi = \Delta\Gamma$. Here X_i and Z_i are the shear and opening forces, respectively, measured at node i, and Δu_l and Δw_l are the shear and opening displacements measured at node l. Hence, forces and displacements needed to determine the $-\Delta\Pi$ released during the crack extension will be obtained from a single FEA. From equation (2.9): $G = -\frac{\partial\Pi}{\partial A} = \frac{\partial\Gamma}{\partial A}$, the mode I and mode II

components of the ERR G_I and G_{II} are determined for four-noded elements as shown in Fig. 2.11 (Krueger 2004):

$$G_I = -\frac{1}{2\Delta a}.Z_i.\left(w_l - w_{l^*}\right), \tag{2.19a}$$

$$G_{II} = -\frac{1}{2\Delta a}.X_i.\left(u_l - u_{l^*}\right), \tag{2.19b}$$

where a is the element length at the crack front and X_i and Z_i are the measured forces at node i. The displacements behind the crack front are determined at the upper crack face u_l and w_l (node l) and the displacements u_{l*} and w_{l*} are determined at the lower crack face (node l*). The crack surface ΔA is determined as $\Delta A = \Delta a.1$, in which the two-dimensional model is assumed to have the unit thickness. The mode I and mode II components of the strain ERR, G_I and G_{II} are calculated for eight-noded elements as shown in Fig. 2.12 (Krueger 2004):

$$G_I = -\frac{1}{2\Delta a}.Z_i.\left(w_l - w_{l^*}\right) + Z_j.\left(w_m - w_{m^*}\right), \tag{2.20a}$$

$$G_{II} = -\frac{1}{2\Delta a}.X_i.\left(u_l - u_{l^*}\right) + X_j.\left(u_m - u_{m^*}\right), \tag{2.20b}$$

where a is the element length at the crack front. Moreover, the forces X_i and Z_i at the crack tip (node i) and the forces X_j and Z_j at the mid-side node of the crack (node j) are needed. The sliding and opening displacements behind the crack tip are determined at nodes l and l* from the upper crack face u_l and w_l and the lower crack face u_{l*} and w_{l*}. Additionally, the displacements at nodes l and l* and at nodes m and m* are needed. They are determined from displacements at the upper crack face u_m and w_m and at the lower crack face u_{m*} and w_{m*}. The total ERR G_T is then obtained from its mode I, II, III components as:

$$G_T = G_I + G_{II} + G_{III}\,, \tag{2.21}$$

where G_{III} = 0 for the two-dimensional case.

In comparison with other FEM-based methods, VCCT has many advantages. First, *G* can be easily computed by VCCT in conjunction with the FE analysis, since VCCT did not make any assumptions for the form of the stresses and displacements. Therefore, singularity elements are not required at the crack tip. Second, the physical meaning of VCCT is clear: energy to create new surfaces. It combines both force and displacement opening. Third, in contrast to VCE, in VCCT, the second analysis is not required. This leads to a faster calculation. Fourth, the mode-mixity of the fracture can be obtained by VCCT, since it gives individual mode components of ERR. Last, VCCT does not require a special mesh arrangement around the crack front. It is not mesh sensitive, and even a coarse mesh can work. However, the major limitation of the VCCT is that it can only be applied to linear elastic fracture.

2.3.2 Virtual Crack Extension Method

In the VCE method, which was implemented in Ansys, two analyses are performed, one with the crack length *a*, and the other with the crack length $a + \Delta a$. If the potential (strain) energy Π for both cases is stored, the ERR can be calculated from (Ansys 2016):

$$G = -\frac{\Delta \Pi}{\Delta A} = -\frac{\Pi_{a+\Delta a} - \Pi_a}{B\Delta a}\,, \tag{2.22}$$

where *B* is the thickness of the fracture model.

2.3.3 Stress Intensity Factor Approach

The calculation procedure of K in commercial FE codes, such as Ansys, is depicted in (Ansys 2016). For a crack loaded in mode I, the displacement of the investigated point in the y-direction (perpendicular to the crack plane) is given by (Ansys 2016):

$$u_y = \frac{K_I}{2\mu}\sqrt{\frac{r}{2\pi}}\sin\left(\frac{\theta}{2}\right)\left[\kappa + 1 - 2\sin^2\left(\frac{\theta}{2}\right)\right], \tag{2.23}$$

with $\kappa = 3 - 4\nu$ for plain strain and $\kappa = \frac{3-\nu}{1+\nu}$ for plain stress and $\mu = \frac{E}{2(1+\nu)}$ is the shear modulus, r and θ are the point's polar coordinates. This expression also follows from Westergaard's solution to the differential equation based on the Airy's stress function. The higher order terms are neglected in this solution. This means that it is only valid near the crack tip. Evaluating the equation for the displacement u_y at θ = ±180° gives the displacement at the crack faces (Ansys 2016):

$$u_y = \frac{K_I}{2\mu}\sqrt{\frac{r}{2\pi}}(\kappa + 1). \tag{2.24}$$

Therefore:

$$K_I = \sqrt{2\pi}\,\frac{\mu}{1+\kappa}\,\frac{|\Delta u_y|}{\sqrt{r}}, \tag{2.25}$$

where Δu_y is the motion of one crack face with respect to the other one. The crack intensity factors in the other modes can be determined in the same way using the displacements u_x and u_z.

Using this method, the intensity factors are determined in Ansys APDL by the KCALC command. Having K, G is then calculated by the formula (Krueger 2004):

$$G = \begin{cases} \dfrac{K^2}{E} \\ \dfrac{K^2}{E}(1-\nu^2) \end{cases} \tag{2.26}$$

which expresses the relationship between G and K to calculate G.

In Ansys, the POST1-command KCALC is used to determine stress-intensity factors at different fracture modes K_I, K_{II}, and K_{III}. Note that KCALC is limited for linear elastic problems with homogeneous, isotropic materials. To use KCALC, follow these steps within the POST1 postprocessor (Ansys 2016):

+ Define a crack-front coordinate system: x-axis has to be set to be parallel to the crack face (i.e. perpendicular to the crack front if the model is three dimensional) and y-axis perpendicular to the crack face. This coordinate system has to be the active coordinate system (CSYS) or result coordinate system (RSYS) when KCALC executes.

+ Define a path along the crack face starting from crack-tip node: for a half-crack configuration (Fig. 2.13(a)), two more nodes are needed along the crack face; for a full-crack configuration (Fig. 2.13(b)) in which both adjacent crack faces are involved, four more nodes are needed.

+ Calculate K_I, K_{II}, and K_{III}: KCALC command is used to calculate the SIFs.

2.3.4 J-integral Method

As mentioned in section 2.2.3, for a nonlinear elastic body containing a crack, the J-integral is defined as (Anderson 2005):

$$J = \int_\Gamma w dy - T_i \frac{\partial u_i}{\partial x} ds \,,$$

where $w = \int_0^{\varepsilon_{ij}} \sigma_{ij} d\varepsilon_{ij}$ is the strain energy density, $T_i = \sigma_{ij} n_j$ is the traction vector, Γ is an arbitrary contour around the tip of the crack, n is the unit vector normal to Γ, and σ, ε, u are the stress,

strain and displacement field, respectively. The strain energy density *w* can preferably be defined per element. That means that it is possible to divide the strain energy for each element. Creating a path around the crack tip, mapping the strain energy density to this path and integrate over the path length with respect to *y*, gives the first term $\int_{\Gamma} w dy$. Defining a normal vector to the path Γ and using the stresses σ_x , σ_y and σ_{xy} makes it possible to get the traction vector $T_i = \sigma_{ij} n_j$ working on the path. The derivatives $\frac{\partial u_i}{\partial x}$ are defined by mapping the displacements to the path, then moving the path by a distance in the x-direction in the local crack tip coordinate system. Knowing the distance ∂x the path is moved and makes it possible to approximate the derivates. With the traction vector and the derivates of the known displacements the second term in the equation $\int_{\Gamma} T_i \frac{\partial u_i}{\partial x} ds$ can be calculated.

Using this principle, J-integral has been implemented in Ansys in which the J-integral is calculated at the solution phase of the analysis after a sub-step has converged. Ansys then stores the value in the result file. J-integral is performed in four steps (Ansys 2016):

+ Initiate a new J-integral calculation: to start a J-integral calculation, use the CINT command's NEW option and provide a number to identify the input information for the J-integral calculation.

+ Define crack information: the crack tip node component and the crack extension direction are both necessary for a J-integral calculation. Two methods using the CINT command are available for specifying the values. First, one defines the crack tip node component and the crack plane normal. This approach applies for both 2-D crack geometry and 3-D flat crack surfaces. It offers a simple way to define a 3-D J-integral calculation in which only the definition of the crack tip (front) node component and the normal of the crack plane are needed. Use this

method when the crack plane is flat. In the second method, one defines the crack extension node component and crack extension direction. This approach applies for 3-D curve crack planes, where a unique normal may not exist. However, the crack extension node component and the crack extension direction at each crack tip node location must be defined. This method is used when the crack plane is not flat, or when a set of nodes form the crack tip, as in the case of a collapsed crack tip mesh.

+ Specify the number of contours to calculate: this step specifies the number of contours for the J-integral evaluation. This step helps users get the convergence value of the J-integral.

+ Define a crack symmetry condition: if the crack is located along a symmetry plane, and only a half model is created, define a symmetric condition so that Ansys can account for it.

In comparison with other fracture mechanics computational methods, the biggest advantage of J-integral is that it can be used for linear elastic as well as nonlinear elastic and elastic-plastic materials. The major limitation of the J-integral method is that it is impossible to get the mode-mixity of the fracture.

2.3.5 Cohesive Zone Model

The cohesion zone model (CZM) which was critically reviewed in reference (Park et al. 2013) is one of the most modern evolutions in fracture mechanics. It is well known that the traditional mentioned fracture mechanics approaches cannot predict the crack nucleation. When the nonlinear plastic zone size around the crack tip becomes comparable to or larger than the characteristic size, the assumption of small plastic zone size is no longer valid. Therefore, another approach is required. CZM, on the other hand, can investigate both nucleation and growth of interfacial delamination without the assumption of small plastic zone size. Moreover, while in all other methods, even for brittle materials the presence of a pre-crack is needed, it is

not necessary to introduce a pre-crack in CZM (Camanho et al. 2004; Tvergaard et al. 1992; van Hal et al. 2007). So far, CZM has been successfully applied to investigate the fracture at dissimilar material interfaces (Tvergaard et al. 1993; Xu et al. 1994) or to study the composite delamination (Alfano et al. 2001).

CZM is a phenomenological rather than physical model of fracture process inside materials or along interfaces. CZM was originally proposed by (Dugdale 1960) where the plastic deformation area is assumed to be a narrow strip ahead of the crack tip involving the extent of plastic yielding and applied loading. Based on the atomic nature of the fracture nucleation and propagation, this narrow plastic strip was then modeled to be a cohesive zone where the stress ahead of the crack tip (in the strip) is a function of surfaces separation rather than a constant yielding strength (Barenblatt 1962). Instead of taking into account the crack tip singularity (in LEFM), CZM regards the fracture process as a gradual phenomenon where the surfaces separation occurs at the cohesive zone (i.e. crack tip and the involved surfaces) being impeded by cohesive forces (Fig. 2.14).

In CZM, the fracture process is modeled as progressive decay of interface strength. The stress state between the potent crack surfaces governed by a cohesive law or also called a traction-separation law. In other words, a cohesive law describes the debonding of two surfaces mathematically. The cohesive traction works as the resistance to crack nucleation and propagation. It is usually presented as a τ-δ curve, in which τ is the stress to separate the adjacent surfaces or can be understood as the stress on the surfaces and δ is the relative separation between them (Trias 2012). Under external loading, the traction increases with separation and then decreases after it reaches a critical separation δ_c. At this point, the traction is at maximum value τ_m, the crack initiates or, in other words, the material starts the damage process. The actual

crack tip is defined or, in other words, the material is totally damaged where the cohesive traction reaches zero (Fig. 2.15) (Haodan 2010; Trias 2012). If the material/structure is loaded at $\tau < \tau_m$ then the unloading goes back to zero in the same path because the material/structure is not damaged. In another situation, if the material/structure is loaded at $\tau > \tau_m$ then it begins to damage then the unloading goes back to zero as a secant (Fig. 2.15) (Trias 2012). The area under the curve is defined as fracture toughness of the material or interfacial fracture toughness of the interface (Fors 2010). Therefore, besides the material properties of the constitution bulk materials, the cohesive traction-separation law governs the behavior of crack extension without any additional conditions. Several traction-separation laws have been proposed to represent non-linear fracture behavior. There are generally required characteristics for the laws summarized as follows (Park et al. 2013):

+ The traction separation relationship is independent of any rigid body motion.

+ The work to create a new surface is finite, and its value corresponds to the fracture energy, i.e., area under the traction-separation curve.

+ A finite characteristic length scale exists, which leads to a complete failure condition, i.e., no load-bearing capacity.

+ The cohesive traction across the fracture surface generally decreases to zero while the separation increases under the softening condition, which results in the negative stiffness.

+ A potential for the cohesive constitutive relationship may exist, and thus the energy dissipation associated with unloading/reloading is independent of a potential.

Based on the required characteristics, the effective traction (normalized by the cohesive strength (rmax)) and displacement representing the cohesive relations were proposed in terms of cubic polynomial (Tvergaard 1990), trapezoidal (Tvergaard et al. 1993), smoothed trapezoidal

(Scheider et al. 2003), exponential (Ortiz et al. 1999), linear softening (Camacho et al. 1996; Espinosa et al. 2003) and bilinear softening (Wittmann et al. 1988) relationships. However, it is worthy to note that the influence of the curve shape is of lesser importance than the critical traction and separation (Fors 2010).

In practice, to determine the cohesive law of a material or an interface, based on experiments and simulations there are two main approaches: iterative and direct. For iterative approach, various traction-separation relations are imposed in FEA simulations and the one that fits the experimental data the best is selected (Cox et al. 1991; Li et al. 2005a; Mello et al. 2004). Some works done by this approach can be found elsewhere (Cox et al. 1991; Li et al. 2005a; Mello et al. 2004). With the direct approach, the cohesive law is obtained from experiments, such as tensile tests or double cantilever beam tests (Pandya et al. 2000a; Pandya et al. 2000b). Another direct approach involves J-integral calculations from which the traction-separation relation is determined. In this method, J-integral values and the separation of the surfaces adjacent to the crack tip are recorded simultaneously, based on which the traction-separation relation is obtained. Some studies conducted by this approach can be found in references (Sørensen 2002; Sørensen et al. 2003; Zhu et al. 2009).

There are only two cohesive laws available in Ansys APDL: bi-linear and exponential. Bi-linear law is used for contact elements and exponential law is for interface elements (Ansys 2016). In bi-linear approach, two cohesive parameters are needed, including maximum traction and maximum separation (CBDD option) or maximum traction and critical ERR (CBDE option). In exponential approach, three cohesive parameters are needed, including maximum stress, normal displacement at maximum stress and tangential displacement at maximum stress.

2.4 Tables and Figures

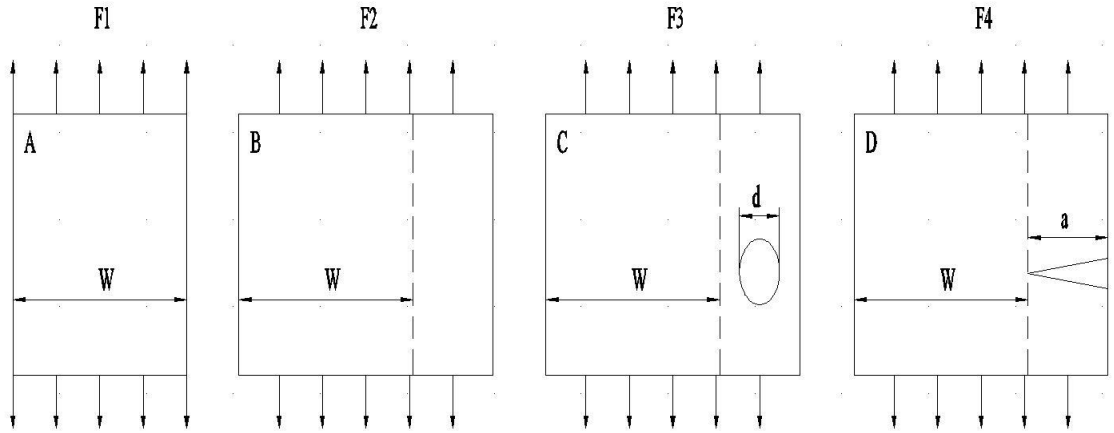

Figure 2.1 (A) (B) un-cracked and (C) (D) cracked plates with different sample and crack geometry.

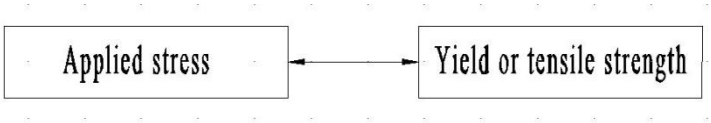

a. Strength of materials approach

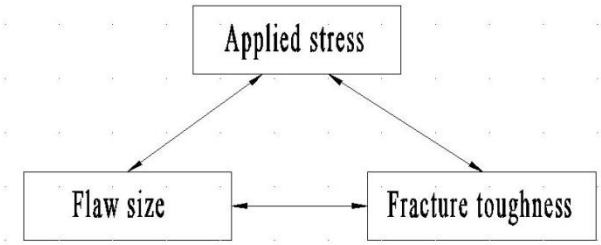

b. Fracture mechanics approach

Figure 2.2 Comparison of the fracture mechanics approach to the strength of materials approach. (a) strength of materials approach and (b) fracture mechanics approach.

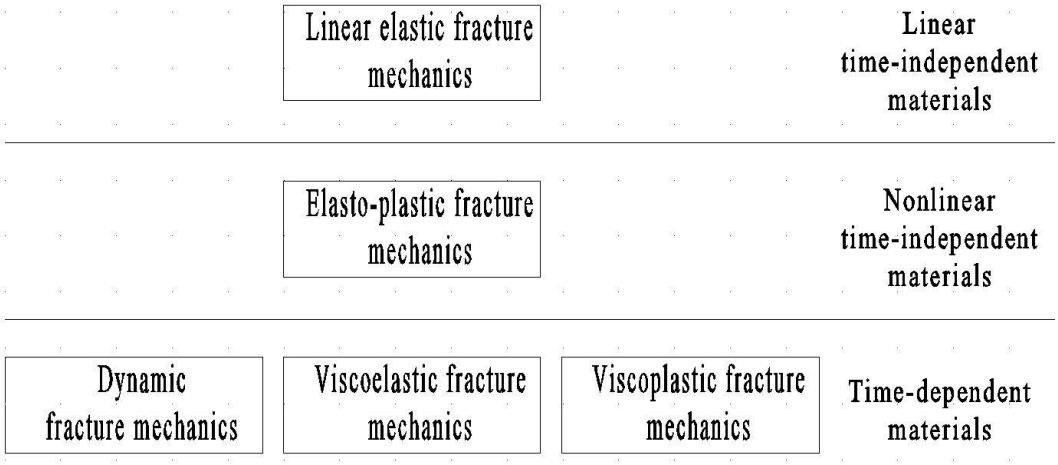

Figure 2.3 Simplified family tree of fracture mechanics.

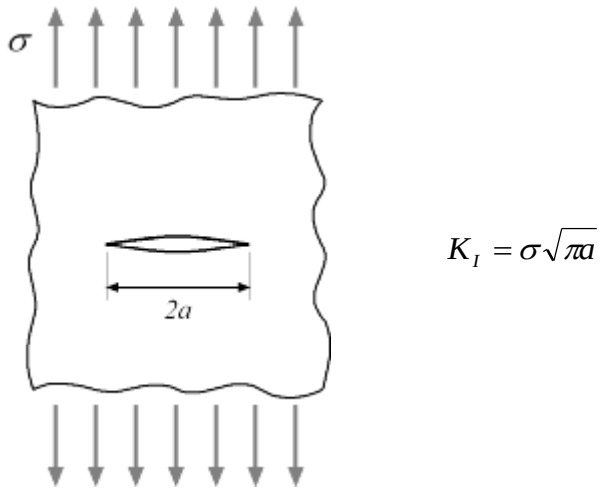

Figure 2.4 Crack in an infinite plate under uniform tension. Credit wikipedia.com, which is in public domain.

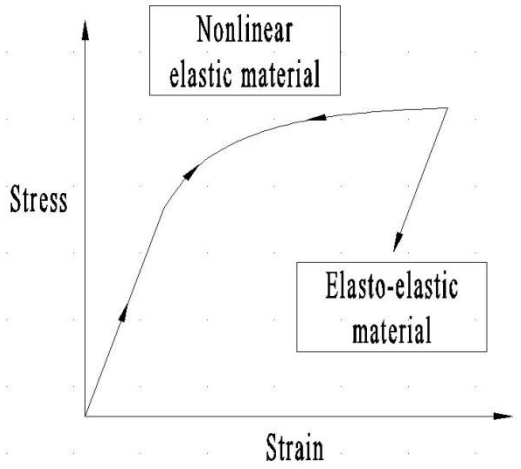

Figure 2.5 Difference between nonlinear elastic material and elastic plastic material.

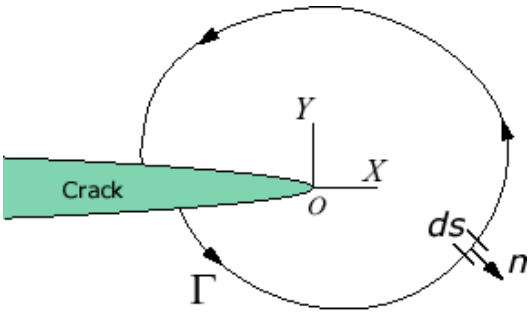

Figure 2.6 J-integral. Credit (Ansys 2016), which is in public domain.

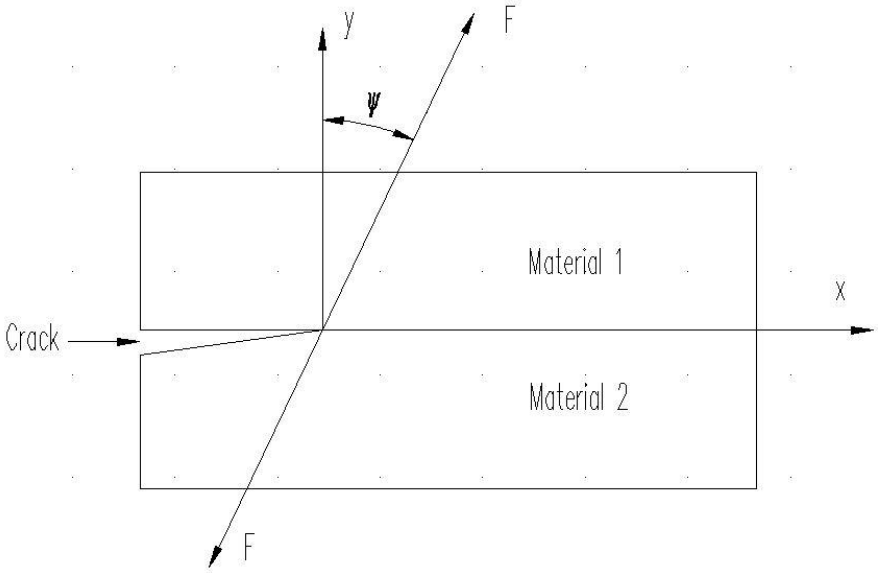

Figure 2.7 Geometry of a bi-material specimen with an interface crack.

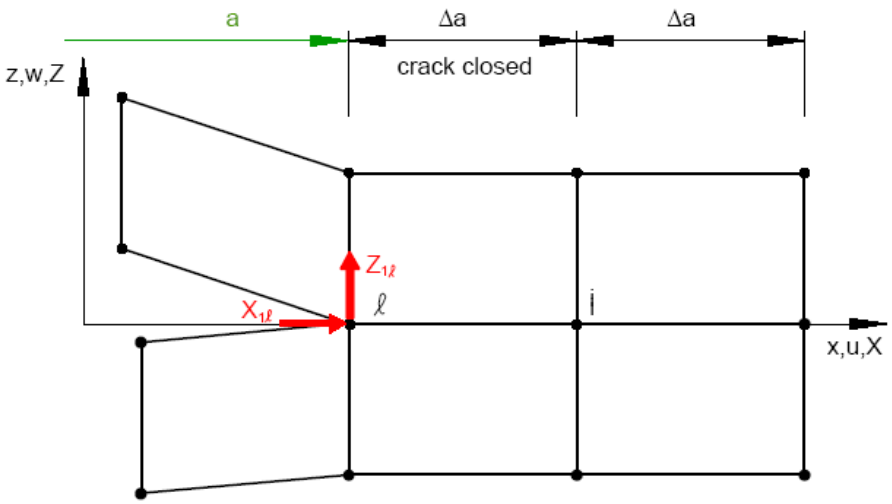

Figure 2.8 First step - Crack closed. Credit (Krueger 2004).

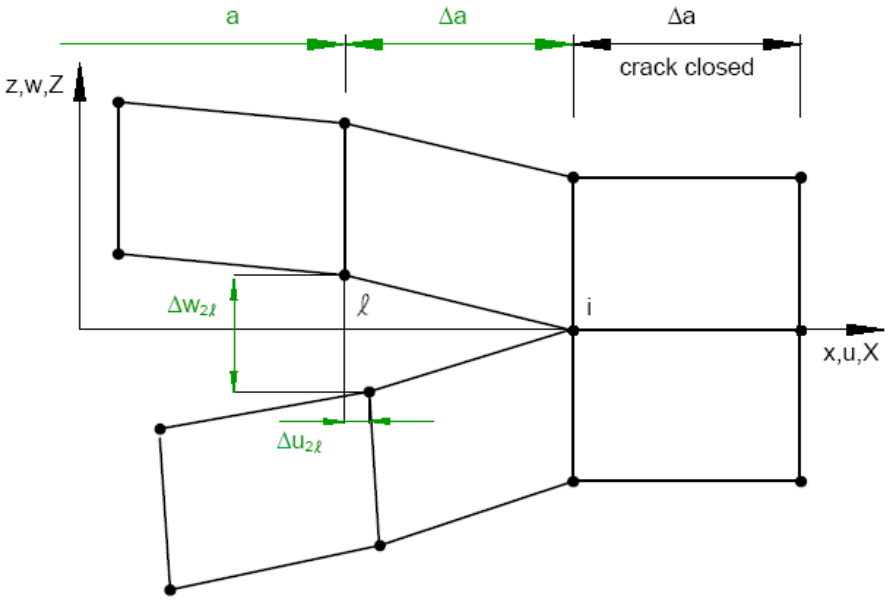

Figure 2.9 Second step - Crack extended. Credit (Krueger 2004).

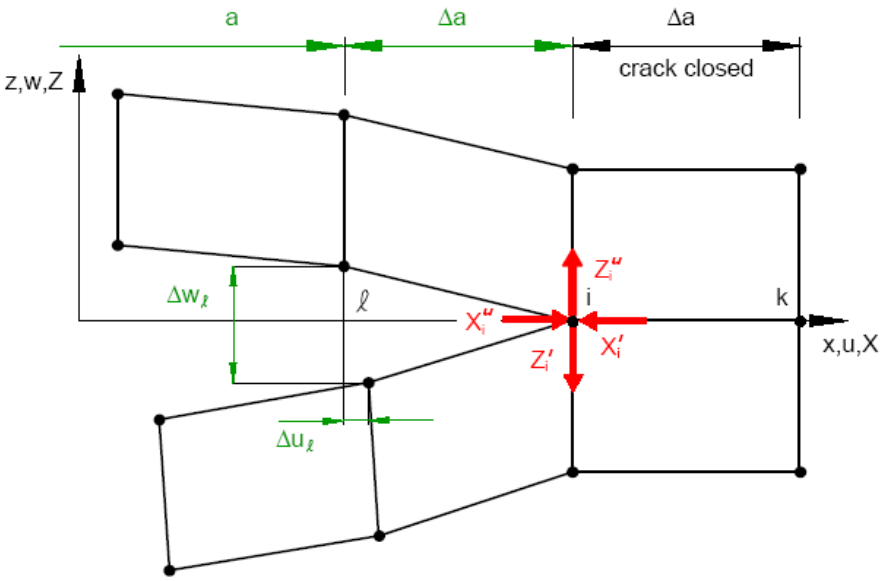

Figure 2.10 VCCT (or 1 step – VCCT). Credit (Krueger 2004).

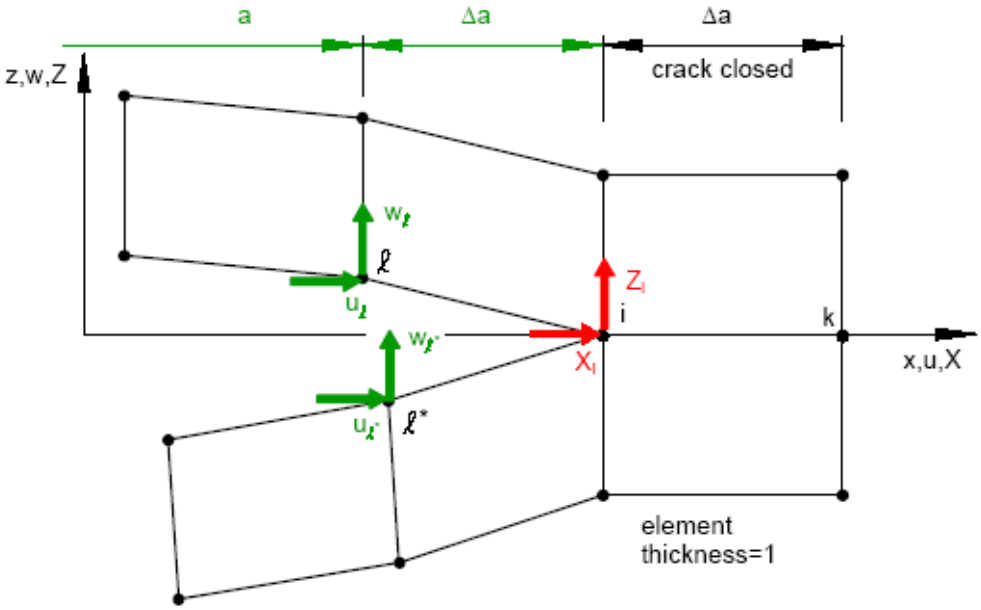

Figure 2.11 VCCT for four-noded elements. Credit (Krueger 2004).

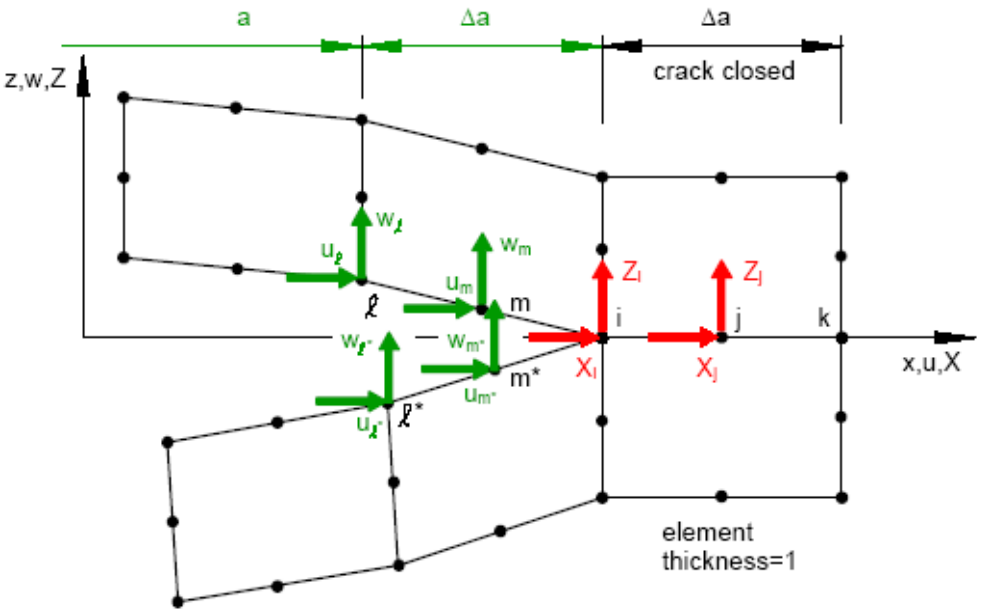

Figure 2.12 VCCT for eight-noded elements. Credit (Krueger 2004).

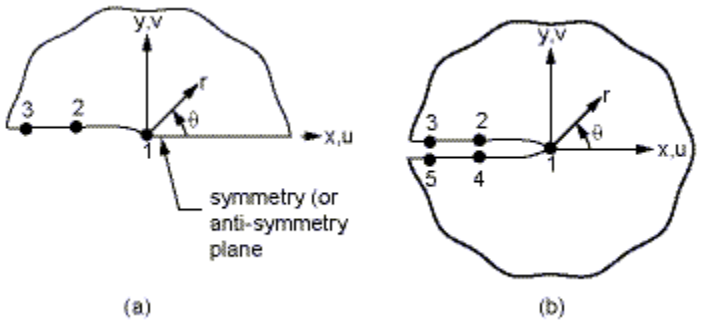

Figure 2.13 Half-crack and full-crack models. Credit (Ansys 2016), which is in public domain.

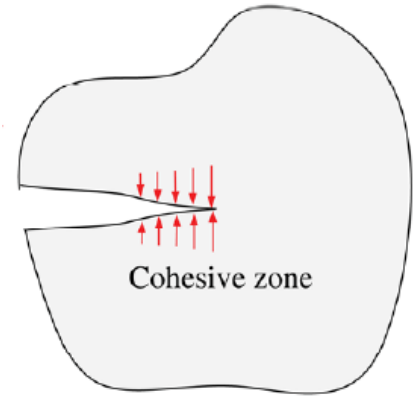

Figure 2.14 Cohesive zone model. Credit (Park et al. 2013).

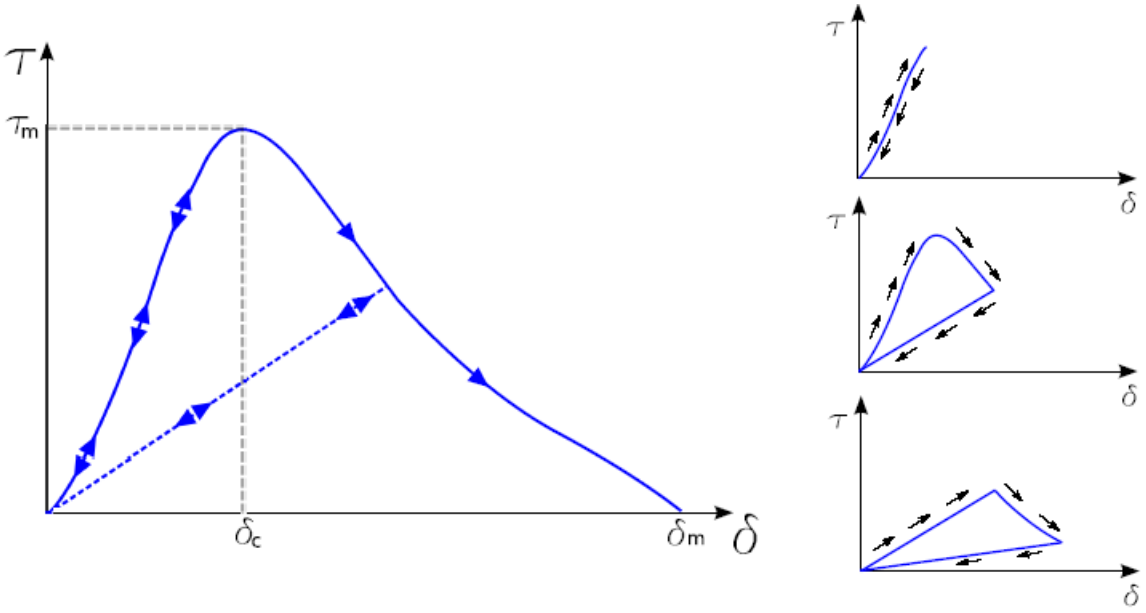

Figure 2.15 Cohesive law. Credit (Trias 2012), which is in public domain.

CHAPTER 3: OPTIMIZING DUCTILITY AND FRACTURE PROPERTIES OF BRITTLE METALLIC THIN FILMS ON POLYIMIDE SUBSTRATES USING MULTILAYER SCHEMES

3.1 Introduction

Ductility mismatch between the metallic interconnect thin films and the flexible polymer substrate has often led to limited stretchability and thus hindering reliable performance of the whole flexible electronics system. Various strategies have been adopted to improve the stretchability of the metal film coated on polymer, mostly focusing on crystalline thin films, such as Cu and Cr (Kim et al. 2005a; Kim et al. 2005b; Lin et al. 2008; Park et al. 2000; Xu et al. 2011). Metallic film's rupture strain has been found to be highly sensitive to film adhesion to the substrate. Improved film/substrate adhesion delays interfacial debonding and retards strain localization, such as necking or shear band formation in the film (George et al. 2005; Xiang et al. 2005). Annealing at relatively low temperatures also improves the strechability and fracture toughness of crystalline thin films by grain growth and other related phenomena (Lu et al. 2009).

As mentioned in chapter 1, compared to crystalline counterparts, various amorphous alloys stand out to be good candidates as functional materials due to their good metallic bonding ability (Chu et al. 2009; Inoue 2001; Wang 2009), excellent mechanical, corrosion (Chu et al. 2010; Moffat et al. 1993), and magnetic properties (McHenry et al. 1999; Phan et al. 2008). Nevertheless, most amorphous alloys are quasi-brittle due to the lack of strain hardening mechanisms or any intrinsic crack propagation barriers, such as grain boundaries or secondary

phase boundaries. Therefore, their limited ductility and low fracture toughness often lead to high sensitivity to structural variables, such as surface roughness, making them unreliable for the widespread use (Schuh et al. 2007). One solution for this issue is adding crystalline metal layer(s) to create a hierarchical multilayered structure (Misra et al. 2005; Wang et al. 2005; Zhang et al. 2014). The ductile crystalline layer will mitigate the catastrophic shear bands propagation of the amorphous layers and localize crack propagation. Despite current progress, there have been very limited attempts to characterize the fracture behavior of amorphous alloys, especially under tensile loading conditions.

In this chapter, Cu was chosen as the crystalline buffer layer to the amorphous film due to its relatively high elongation and tensile strength. It was proposed that if the strength of the well-adhered crystalline layer is similar or higher than that of the amorphous counterpart, the amorphous layer will be constrained by the crystalline one, making the whole multilayered film fail at a larger strain (Chen et al. 2011b; Li et al. 2007b; Nieh et al. 1999). In this chapter, crystallinity of the Al thin films was tuned by varying Mn concentration in the alloy (Ruan et al. 2009). Increasing Mn% from 5.2 at.% to 20.5 at.% leads to a phase transformation from supersaturated fcc phase with moderate ductility to brittle amorphous phase. Thin film microstructure and composition were characterized using SEM, EDS, TEM and SAD. Tensile tests of metal coated PI were performed and the strains were measured using DIC method. It was found that the amorphous Al-20.5 at.% Mn exhibits the highest fracture stress and fracture toughness, but lowest ductility. Further improvement of fracture toughness, interfacial fracture toughness and elongation of the amorphous alloy/PI system was achieved by adopting bilayered and trilayered structures using ultrathin Cu buffer layers. Finally, the failure mechanisms of the layered films were modeled using finite element analysis (FEA).

3.2 Experimental Procedure

3.2.1 Sample Preparation

Al-Mn thin films were magnetron sputtered on 7.6 μm thick PI foils (Kapton HN by DuPont). Prior to film deposition, the PI substrates were ultrasonically cleaned with acetone and ethanol. All depositions were performed using the CRC-100 sputtering system with 70 W RF power at a base pressure of $1x10^{-6}$ Torr. The nominal target-substrate distance was 60 mm and the deposition rate was about 0.11 nm/s. Six sets of samples were prepared, as listed in Table 3.1. The total thickness of metallic films on all samples was kept at about 1.2 μm to minimize the film thickness effect on fracture strain (Cordill et al. 2010). Samples M5 (Al-5.2 at.% Mn), M11 (Al-11.5 at.% Mn) and M20 (Al-20.5 at.% Mn) are 1.2 μm thick monolithic films on PI substrate (Fig. 3.1). Samples B1 and B2 are bilayered films with 50 nm and 100 nm Cu buffer layer between the PI substrate and the Al-Mn film, respectively, with the total film thickness (i.e. thickness of both the Cu and Al-Mn layer) of 1.2 μm (Fig. 3.2). Sample S is a trilayered structure on the PI substrate, with two Cu layers (100 nm) sandwiching the Al-20.5 at.% Mn layer (1 μm) (Fig. 3.3). After film deposition, coated PI exhibits negligible curvature change, thus the residual stress in the film is neglected in this study. This is consistent with extensive previous reports showing that the highly compressive residual stress in thin films increases (or the absolute value decreases) rapidly with increasing film thickness and becomes close to zero at layer thicknesses greater than 500 nm (Frank et al. 2011).

Surface morphology and chemical composition of as-deposited samples were characterized using TEM (Hitachi SU-70) and EDS (EDAX-Phoenix). TEM samples were prepared by directly sputtering Al-Mn alloys on continuous carbon film grids for 15 min to reach

a sample thickness of ~150 nm. Bright-field, dark-field imaging, and SAD analysis were performed using Tecani F20 TEM operated at 200 kV with a field emission gun.

3.2.2 Tensile Testing

Uniaxial tensile tests (DTS, National Instruments) were carried out at a constant strain rate of $4x10^{-4}$ s^{-1} at room temperature. Rectangular samples with 4×20 mm^2 gauge area were used. All results reported were obtained by averaging from at least four separate tests. Electrical resistance of the samples was recorded using Tektronix 4050 multimeter during the test. The critical strain ε_c, i.e. the macroscopic strain, which characterizes the micro-crack formation (as opposed to rupture), was obtained by using electrical resistance change method (Lu et al. 2007; Niu et al. 2007). Fig. 3.4 shows a typical evolution of electrical resistance change during a tensile test, where ε_c is defined at the point where the electrical resistance deviated from the ideal curve (Niu et al. 2007). The force of the film (F_{film}) at a certain displacement was estimated as $F_{film} = F_{total} - F_{substrate}$ (Macionczyk et al. 1999; Pei et al. 2011) (neglecting the force required to break the native oxide layer on the metallic film), where F_{total} and $F_{substrate}$ are the tensile loads of the thin film-coated and uncoated PI specimen at the same displacement, respectively. The tensile stress of the film was then calculated as $\sigma = F_{film}/wt$, where w and t are the width and the thickness of the film, respectively. Strain was measured during tensile tests using DIC method by tracking the makers (all samples were sprayed with fine ink speckles on the surface prior to the tensile testing). The movements of these markers were then tracked with the high definition camera (1920 × 1080 pixels, 30 fps) (Bing et al. 2009). The strain was then calculated from the recorded images using a Matlab routine developed by Christoph Eberl et al. (Eberl 2010). Based on the stress and the strain data of the film, the true stress - strain curve of the film was obtained. This "non-touching" methodology (i.e. using DIC) to get stress - strain

curves was going to give extremely accurate results in comparison with traditional methods, such as using strain gauge, especially for such thin samples.

3.3 Results and Discussion

3.3.1 Microstructure of As-Deposited Al-Mn

Microstructure of as-deposited monolithic Al-Mn was studied by TEM and SAD, as shown in Fig. 3.5. Increasing Mn% in the alloy leads to a phase transition from a supersaturated fcc structure to a completely amorphous phase, similar to electrodeposited Al-Mn (Ruan et al. 2009). At 5.2 at.% Mn, Fig. 3.5(a) shows that sample M5 contains a single fcc phase (lattice constant a = 4.036 Å) with an average grain size <d> of ~15 nm. At the intermediate Mn concentration of 11.5 at.%, M11 contains a complex dual phase structure, where nanocrystalline fcc (a = 4.035 Å and <d> = 12 nm) and amorphous phases coexist. Further increasing Mn concentration to 20.5 at.% leads to the formation of a completely amorphous microstructure of M20, as confirmed by the diffuse halo in the SAD pattern (Fig. 3.5(f)).

3.3.2 Tensile Behavior of Monolithic and Multilayered Samples

Typical true stress-strain curves of the monolithic and multilayer samples are shown in Fig. 3.6. The arrows indicate the critical strains (ε_c). Table 3.1 lists the mechanical properties obtained from the stress-strain curves, including elastic modulus (E), fracture stress (σ_f, i.e. the film stress at its critical strain), critical strain (ε_c), and fracture toughness (K_{Ic}). The mode I critical SIF K_{Ic} (fracture toughness) was calculated from the critical ERR G_c as (Freund et al. 2003):

$$K_{Ic} = \sqrt{\frac{EG_c}{1-\nu^2}}, \tag{3.1}$$

where E and ν are the elastic modulus and the Poisson's ratio of the film, respectively. G_c was calculated as (Beuth Jr 1992):

$$G_c = \frac{\pi {\sigma_f}^2 h_T}{2E}(1-\nu^2)g(\alpha,\beta), \tag{3.2}$$

where h_T is the total thickness of the film (~1.2 μm), $g\ (\alpha, \beta)$ is a dimensionless quantity determined by the elastic mismatch between the film and the substrate, and α and β are the two Dundurs' parameters defined as:

$$\alpha = \frac{\bar{E}_1 - \bar{E}_2}{\bar{E}_1 + \bar{E}_2}, \quad \text{and} \quad \beta = \frac{\mu_1(1-2\nu_2) - \mu_2(1-2\nu_1)}{2\mu_1(1-\nu_2) + 2\mu_2(1-\nu_1)}, \tag{3.3}$$

where $\bar{E} = E/(1-\nu^2)$ is the plane strain tensile modulus and μ is the shear modulus. The subscripts 1 and 2 refer to the film and the PI, respectively. In this work, α ranges from 0.87 to 0.95, $\beta \approx \alpha/4$ and $g\ (\alpha, \beta)$ are linear interpolation values obtained from reference (Beuth Jr 1992). It should be noted that the ERR calculated from eqn. (3.2) considers a single channeling crack in a thin film on a semi-infinite substrate, while the effect of crack spacing on G is neglected. For deformed ductile thin films such as Cu on compliant substrate, parallel channel cracks are often observed perpendicular to the loading direction. It was shown that the ERR of such thin films increases with crack spacing for a given film (and substrate) thickness and eventually reaches a maximum (saturated) value that corresponds to the case with a single isolated crack (Huang et al. 2003). However, as will be shown later in section 4.2, the deformed amorphous Al-Mn (M20) thin films studied here do not exhibit the typical parallel channel cracks, but rather extensive shear bands inclined or perpendicular to the loading direction. For samples with Cu buffer layers, such as B1, B2 and S, parallel cracks were indeed observed (Fig. 3.8(b-d)), with crack spacing between ~ 50 nm to 100 μm and crack spacing to film thickness ratio around ~ 42-83. In such cases, the ERR is approaching the saturated value as calculated here. Hence, considering the behavior of both monolithic (M20) and layered samples (B1, B2, and S), we neglect the effect of crack spacing and adopt eqn. (3.2) to calculate G for simplicity, while it should be noted that such calculations correspond to an upper limit of the steady state ERR for some samples.

Representative true stress-strain curves of all samples are shown in Fig. 3.3. For all monolithic samples, the stress reaches a maximum at the critical strain, followed by a stress relaxation due to crack and/or shear band formation. In addition, all mechanical properties, including σ_f, E, and K_{Ic} were found to increase with Mn %, with M20 exhibiting the highest values of all, as shown in Fig. 3.7 and Table 3.1. However, at the highest Mn concentration (20.5 at.%), the amorphous nature of M20 renders a very low tensile ductility (~0.46%). This is not surprising given that amorphous alloys lack sufficient intrinsic mechanisms to hinder crack propagation or strain hardening (Schuh et al. 2007). Fig. 3.8(a) shows a typical SEM image of the surface of M20 at the critical strain. Extensive shear bands, either inclined at an angle of ~45^o or perpendicular to the loading direction can be seen (indicated by white arrows), which contribute to the failure of an amorphous material (Schuh et al. 2007).

The critical strains remain very low (less than 0.65%) for all monolithic samples regardless of their crystallinity, similar to the behavior of brittle thin films, such as Cr (< 1%) (Cordill et al. 2010) and Ta (0.6%) (Frank et al. 2009) on PI. To improve the film/substrate adhesion and stretchability of the system, bilayered (B1 and B2) and trilayered(S) samples were designed via extrinsic toughening mechanisms (Hofmann et al. 2008; Ritchie 2011). Fig. 3.6(b) shows the true stress-strain curves of all layered samples (B1, B2, and S). It can be seen that while ε_c occurred in the elastic domain in all monolithic samples (Fig. 3.6a)), it always occurred after extensive "plastic" deformation in the multilayered samples. Fig. 3.7(a) shows that the bilayer scheme (B1) can enhance the elongation of M20 by more than 13 times (from 0.46% to 6.24%). However, at the same time, the fracture toughness decreased from 1.38 to 0.79 MPa·m$^{1/2}$. In contrast to B1, B2 samples maintained high fracture toughness of M20 and moderate improvement of critical strain (from 0.46% to 2.32%). Finally, the trilayered sample S

turned out to be the optimized solution, which exhibits a combination of high ductility (5.67%), fracture stress (~284 MPa) and fracture toughness (1.13 $MPa \cdot m^{1/2}$). The following discussions justify these experimental observations.

3.3.3 Fracture Mechanisms at the Brittle/Ductile Interface in the Multilayered Samples

In a ductile/brittle layered structure, crack often initiates in the brittle layer and then travels to the ductile/brittle interface (Wu et al. 2014). As long as the thickness (h) of the ductile layer (e.g. Cu in this work) is much larger than its Burgers vector, emitted dislocations will move away from the crack tip under tensile loading (Hsia et al. 1994). In the ductile layer, emitted dislocations will blunt the crack tip and therefore reduce the tensile stress at the crack tip. Hence, the crack propagation process is suppressed, since the crack tip stress is unable to reach the cohesive tensile strength of the interface (Hsia et al. 1994). Moreover, if the strength of the ductile material is increased, its fracture toughness will be increased because of the plastic deformation during crack propagation (Was et al. 1996). Therefore, adding a ductile Cu layer has the potential to improve the ductility as well as the fracture toughness of the amorphous Al-Mn/PI structure. However, the dislocations emitted in the ductile layer are also confined by the brittle layer. These dislocations pile up at the interface, generating additional stress at the crack tip, which hinders further dislocation emission and blunting process at the crack tip (Anderson et al. 1993). Gradually, the tensile stress at the blunted crack tip reaches a critical strength resulting in fracture. Therefore, the fracture toughness of the film depends on the number of dislocations emitted, which in turn depends on the thickness of the ductile layer (Hsia et al. 1994).

What is the appropriate ductile layer thickness that should be added to the amorphous M20 sample to optimize its ductility and fracture toughness? We approach this problem by evaluating the constraining effect of the ductile layer on the fracture behavior of a composite

material consisting of alternating ductile and brittle layer(s). In a ductile metallic layer with a crack, the plastic zone size at the crack tip can be estimated as (Hsia et al. 1994):

$$r_p = \frac{1}{2\pi}\left(\frac{K_{I_c}}{\sigma_Y}\right)^2, \tag{3.4}$$

where K_{I_c} is the fracture toughness and σ_Y is the yield strength of the material. When the layer thickness (h) of the ductile phase is large, the plastic zone size is on the order of millimeters or even centimeters, similar to its bulk counterpart. However, in thin films with h ranging from a few micrometers to ~10 nm, the plastic zone is confined ($h < r_p$), resulting in a reduced fracture toughness (Hsia et al. 1994; Varias et al. 1991). In this case, dislocation activities in ductile thin film (Cu layer) no longer obey the continuum plasticity theory. The discrete dislocations interact with the crack tip and the interfaces, which serve as barriers preventing dislocations from crossing over into the brittle layer. Because of this dislocation confinement, fracture toughness increases with the ductile layer thickness (Hsia et al. 1994). For example, Wu et al. (Wu et al. 2014) showed that in Cu/Mo multilayers coated on PI, the adhesion energy remains low when the thickness of the ductile Cu layer (h_{Cu}) is below ~25 nm, but increases rapidly with h_{Cu} afterwards. Zhang et al. (2011) studied the effect of layer thickness on the fracture behavior of Cu/Nb and Cu/Zr multilayers coated on PI. They found that the fracture mode of the mutlilayers is controlled by the constraining effect of the Cu layer and the fracture toughness increases with h_{Cu} and reaches a steady-state at h_{Cu} > 20-30 nm. On the other hand, when h_{Cu} is reduced to less than ~15 nm, dislocation activities are greatly suppressed and their shielding effect is minimized, resulting in a significant reduction of deformability of the Cu layers (i.e. Cu layers become more brittle). Based on the above discussion, we chose h_{Cu} of 50 nm and 100 nm to be added to the monolithic Al-Mn/PI structure (samples B1, B2, and S) in order to optimize the ductility and the fracture properties of amorphous thin film on PI substrate.

Next, a fracture model proposed by Hsia et al. (1994) was employed to justify the effect of Cu layer thickness on the fracture behavior of B1 and B2 samples. In this model, crack propagation in a composite structure composed of submicron thick ductile and brittle layers is considered. This model considers the constraint effect of the ductile layer on the propagation of a crack initiated at the brittle layer and blocked by the interface. As discussed above, the dislocations emitted from the crack tip blunt the crack tip and consequently reduce the tensile stress at the crack tip. At the same time, these emitted dislocations also pile up at the interface sending back a stress to the crack tip, impeding further dislocation emission. Based on the crack tip shielding and blunting effects by the emitted dislocations, the equilibrium number of dislocations (n) is determined as (Hsia et al. 1994):

$$n = \frac{4\pi(1-\nu)}{\ln\left(\frac{\tilde{h}}{\tilde{r}}\right)}\left(\frac{\tilde{K}_{app}\sqrt{\tilde{h}}}{A\sqrt{2\pi}} sin\varphi cos\frac{\varphi}{2} - \tilde{\gamma}\right), \tag{3.5}$$

where ν = 0.328 is the Poisson's ratio of Cu (Yu et al. 2004) and A is a factor that is slightly greater than unity (Hsia et al. 1994). $\tilde{K}_{app}$, $\tilde{h}$, $\tilde{\gamma}$ and $\tilde{r}$ are the normalized values defined as:

$$\tilde{K}_{app} = \frac{K_{app}}{\mu\sqrt{\beta}}, \tilde{h} = \frac{h_\varphi}{b}, \ \tilde{\gamma} = \frac{\gamma}{\mu b}, \tilde{r} \approx 2.7\frac{r_0}{b}, \tag{3.6}$$

where K_{app} is the far field SIF of the Cu thin film. The values of K_{app} are 0.97 and 1.17 MPa·m$^{1/2}$ for the Cu layers in B1 and B2, respectively, calculated from equations (3.1)-(3.3) (σ_{Cu} is thickness-dependent, taking the values of 1180 MPa and 1000 MPa for the Cu layers in B1 and B2, respectively (Zhang et al. 2008a); E_{Cu} is 90 GPa (Yu et al. 2004); g_{Cu} (α, β) is 8.65 for both the Cu layers in B1 and B2 (Beuth Jr 1992)). μ is the shear modulus of Cu, taking the value of 33.89 GPa (Yu et al. 2004), $\beta = 2\sqrt{(2/\pi)}$ assuming that the crack has a semi-circular front, and $h_\varphi = h_{Cu}/(2sin\varphi)$ being the maximum distance the leading dislocation can travel before it is blocked by the interface. φ is the angle that the slip plane inclines from the interface (φ is chosen

as 45° without a loss of generality). b is the Burgers vector of Cu (2.56 Å). $\tilde{\gamma}$ is the normalized surface energy ($\tilde{\gamma} \approx 0.1684$ estimated from Rice et al. (1974)). r_0 is the effective core radius of dislocations ($r_0 = 1.725$ nm (Hsia et al. 1994)). The equilibrium number of dislocations estimated from equation (3.5) is 22 and 28 for the Cu films in B1 and B2, respectively.

With the presence of the shielding effect of the dislocations, the SIF at the crack tip is defined as (Hsia et al. 1994):

$$K_{tip} = K_{app} - K_D, \tag{3.7}$$

where K_D is the contribution of the dislocations to the stress intensity at the crack tip (Hsia et al. 1994):

$$K_D = \frac{\mu b}{(1-\nu)\sqrt{2\pi h_\varphi}} \frac{3}{2} sin\varphi cos\frac{\varphi}{2}. \tag{3.8}$$

The maximum tensile stress at the crack tip is determined as (Hsia et al. 1994):

$$\sigma_{tip} = \beta \frac{K_{tip}}{\sqrt{nb}}. \tag{3.9}$$

Using the input values described above, K_{tip} were estimated to be 0.92 MPa·m$^{1/2}$ and 1.13 MPa·m$^{1/2}$, and σ_{tip} were estimated to be 1.94 GPa and 2.12 GPa for the samples B1 and B2, respectively. The higher value of the crack tip stress intensity (K_{tip}) in B2 shows that a thicker Cu layer can accommodate more damage and emit larger number of dislocations before fracture. These results are in agreement with our experimental observations that the fracture toughness of the whole B2 sample is higher than B1 (Fig. 3.7(c)). Moreover, the fact that maximum tensile stress at the crack tip (σ_{tip}) in B2 is larger than that in B1 (along with the substrate effect as discussed later in section 4.2) suggests that the Cu layer in sample B2 has a higher stress concentration than in B1, making the elongation of B2 smaller than B1, which agrees well with our experimental observations (Fig. 3.7(a)).

Finally, let us consider the behavior of the sandwiched trilayer sample S, which is the optimized solution that exhibits a combination of high ductility (5.67%) and high fracture toughness (1.13 MPa·$m^{1/2}$). Since cracking of nano-scaled multilayer films is initiated in the brittle layers and hindered by the ductile layers (Wu et al. 2014), in the cases of B1 and B2, the micro-cracks initiated at the top surface of the Al-Mn film and propagated to the Cu/Al-Mn interface. For sample S, having another Cu layer on the top will delay the crack initiation at the brittle Al-Mn layer, which eventually leads to the ductility enhancement.

3.3.4 Failure Mechanisms at the Film/Polymer Interface in Multilayered Samples

Together with the fracture mechanisms at the brittle/ductile interface, those at the film/polymer interface also contribute significantly to the fracture behavior of the multilayered samples. SEM image in Fig. 3.8(b) shows the surface of the sample B1 at the critical strain. The presence of channeling cracks through the width without any shear bands confirmed the ductile fracture via the bilayer scheme (Was et al. 1996; Zhang et al. 2014). It is likely that the presence of a thin (50 nm) Cu layer dissipated the energy from the amorphous alloy layer to the PI substrate and thereby delayed the final failure (Chen et al. 2011a; Kou et al. 2014).

In sample S, the Cu layers limit the propagation of some shear bands distributing the plastic strain to many other bands, delaying fracture, which is why large strain was observed. The failure mechanism can be explained as follows. First, even with a thick (100 nm) Cu layer between the alloy and PI, which slows down the energy dissipation from the Cu layer to PI, sample S still possesses high ductility because of its hierarchical structure of the three layers. The three layers deform differently, i.e. the top surface Cu layer maintains/stabilizes ductility (of the Al-Mn layer) and together with the inner Cu layer they dissipate energy via their plasticity, preserving ductility and delaying the final failure of the whole structure (Chen et al. 2011a; Kou

et al. 2014). Second, it was observed in the DIC program that there were nearly no strain localizations on the sample S' surface. The idea of strain non-localization was first introduced to improve the ductility of nano-materials by designing three-layered stainless steel sheets with surface mechanical attrition treatments and co-rolling processes (Chen et al. 2008; Lu et al. 2004). Strain non-localization mitigates the initiation of one critical major crack and delays the crack propagation by transferring the originally localized cracks to other positions (Kou et al. 2014). According to Lu et al. (2009), the critical condition for strain localization to take place is debonding between the film and the substrate, since debonding makes the film locally free-standing and thus necking of the film will be accommodated by local elongation. Fig. 3.9 shows FIB images of the cross-section view of the tested S specimen and confirms that there was no debonding at the film/PI interface, and thereby no strain localization in the S samples. Since a strong bonding between the film and the PI substrate is very critical in maintaining high ductility for such systems, the work in chapter 4 will be an attempt to increase the adhesion of the film/polymer interface.

3.4 Finite Element Simulations

To provide further insight into the failure mechanism and to evaluate the interfacial fracture toughness of the film/PI systems under tensile loading, finite element simulations were performed using Ansys (version 17). A two dimensional plane-strain model of the multilayered film on PI substrate under uniaxial tension was constructed, similar to that in (Zhang et al. 2008b). The total metallic film thickness h_T is 1.2 μm and the PI substrate thickness is 7.6 μm. The length l of the film/substrate system was set at 3.12 μm. The material properties used in the FEM model are listed in Table 3.2. The stress-strain curve of PI is obtained from the manufacturer specifications (Dupont 2004) and that of Cu thin film is from Ref. (Yu et al. 2004).

The properties of the Al-Mn alloy layer were obtained from experiments, as listed in Table 3.1. With the implementation of the CZM (Park et al. 2013) in Ansys APDL, the strain energy density distribution, von Mises equivalent stress distribution and J-integral (which represents interfacial adhesion) were obtained.

Cohesive zones were defined at both the film itself and the interface between the film and the PI substrate. Exponential law was selected as the cohesive law, which describes mathematically the separation or debonding of two parts of the film and of two material surfaces (Park et al. 2013). The stress for which the crack opening starts was assumed to be equal to the yield stress or the fracture stress of the material considered (Dugdale 1960), i.e. Cu and Al-Mn alloy. The maximum normal traction for which the film/substrate interface starts to debond was assumed to be equal to the yield stress or fracture stress of the material that adheres to the PI substrate (Xu et al. 2010). Normal separation across the interface and the shear separation, where the maximum normal traction is attained, were assumed to be identical and obey the law of the fracture energy represented in (Xu et al. 2010). To introduce an imperfection where the crack can nucleate, a V-shaped notch $0.2h_T$ wide and $0.02h_T$ deep was placed at the top of the film (Li et al. 2007a; Lu et al. 2010; Zhang et al. 2008b). Both the film and the substrate were meshed by the two-dimensional 8-node structural solid elements Plane183 with the plane strain option. The interfaces were meshed by the 6-node cohesive elements Inter203. The vertical displacement along the bottom of the substrate as well as the horizontal displacement along the centerline of the system were set to zero, whereas a uniform horizontal displacement of *u/2* was applied to both sides of the film/substrate system. The nominal strain of the system is then *u/l*, where *l* denotes the length of the film/substrate system. Finally, convergence analysis was performed to

get the optimal mesh. Fig. 3.10 shows the sketch of a bilayered sample with the above defined cohesive zones.

To investigate the adhesion of the interface between two dissimilar, non-linear elastic materials (i.e. the film/PI system), path-independent J-integral has been proven to be the only feasible computational method (Anderson 2005; Rice et al. 1965; Tran et al. 2013). A strain of 0.46% (i.e. critical strain of the sample M20) was applied to all multilayer samples. Twelve contours were defined around the crack tip, which rested at the film/substrate interface, to calculate the converged J-integral values. Fig. 3.11 shows the elastic strain energy density distribution of the M20 and S samples at 0.46% strain. It can be seen that the presence of a Cu layer sustained a high amount of strain energy. This confirms that the two Cu layers dissipate energy via their plasticity, together with the ductility of the polymer substrate, preserving the ductility and then delaying the final failure of the whole metallic system (Chen et al. 2011a; Kou et al. 2014). Fig. 3.12 shows the von Mises equivalent stress distributions of M20 and S. The two Cu layers sustain much of the stress distributed to the whole film, which obviously reduces the stress that the alloy layer has to endure. This makes the elongation of the sample S larger and the alloy layer can possess higher critical stress at its critical strain. The J-integrals of the film/substrate interface at the same strain of 0.46% (Fig. 3.13) show that the adhesion of the interface increases significantly with the added Cu layers (from 0.34 J/m^2 for M20 to 0.45 J/m^2 for B2 and S). This result confirms that the bonding between the film and the substrate was improved, making it a critical condition for strain non-localization, delaying the crack propagation by transferring the originally localized cracks to other positions (Kou et al. 2014; Lu et al. 2009).

Finally, to evaluate the ability of the multilayered film/PI systems to resist delamination at the film/polymer interface, interfacial fracture toughness (i.e. critical J-integrals) of all samples were calculated (Tran et al. 2013). Samples M20, B1, B2 and S were applied with their experimental critical strains of 0.46%, 6.24%, 2.32% and 5.67%, respectively (Fig. 3.7(a)). The results in Fig. 3.14 show that with the sandwiching scheme, the interfacial fracture toughness can be enhanced twenty four times from 0.34 J/m^2 (sample M20) to 8.13 J/m^2 (sample S). This result again confirms the significant improvement of the adhesion between the film and the substrate via the sandwich structure.

3.5 Conclusions

Mechanical properties of monolithic and multilayered Al-Mn thin films coated on PI substrates were studied by tensile testing and finite element methods. Among the monolithic films, the amorphous Al-Mn possesses the highest fracture toughness, but limited ductility and poor resistance to interfacial delamination. To improve the stretchability of the system without compromising the fracture toughness, bilayered and trilayered films were designed by adding Cu buffer layers to the system. It was found that the bilayered structure with 50 nm Cu buffer layer improves the ductility of amorphous Al-Mn by more than ten times while the trilayered structure optimizes both ductility and fracture toughness. Analytical modeling and finite element analysis show that in the trilayered structure, the topmost Cu layer retards crack initiation, while the inner Cu layer dissipates strain energy and improves film/PI adhesion. In this case, the elongation was enhanced more than ten times and the interfacial fracture toughness twenty four times with a limited sacrifice of fracture toughness (less than 18%).

The results of this chapter thus provide important guidelines for optimizing mechanical properties of future flexible electronics, whose performance requires reasonable ductility of crystalline and amorphous metallic films on polymer substrates.

3.6 Tables and Figures

Table 3.1 Composition and mechanical properties of monolithic (M5, M11, and M20), bilayered (B1 and B2), and trilayered (S) Al-Mn thin films deposited on PI substrates. h_{Cu} is the thickness of the Cu layer(s) in the samples. The critical strain (ε_c), fracture stress (σ_f) and elastic modulus (E) were measured from the stress-strain curves of uniaxial tensile tests. The Poisson's ratio (ν) was estimated using the rule of mixtures from pure Al and Mn (Cardarelli 2008). Critical J-integrals of the film/substrate interface (interfacial fracture toughness) of samples M20, B1, B2, and S were calculated by FEA at their corresponding critical strains.

Sample ID	Composition	h_{Cu} (nm)	ε_c (%)	σ_f (MPa)	ν	E (GPa)	K_{Ic} (MPa·m$^{1/2}$)	Crit. J-int. (J/m^2)
M5	Al-5.2 at.% Mn	-	0.63 ± 0.06	199.1 ± 8.6	0.34	39.4 ± 7.3	0.58	-
M11	Al-11.5 at.% Mn	-	0.57 ± 0.08	221.1 ± 13.4	0.33	62.3 ± 5.9	0.78	-
M20	Al-20.5 at.% Mn	-	0.46 ± 0.01	321.7 ± 22.7	0.32	103.6 ± 2.9	1.38	0.34
B1	Cu|Al-20.5 at.% Mn	50	6.24 ± 1.14	220.8 ± 11.9	0.32	67.8 ± 2.6	0.79	8.55
B2	Cu|Al-20.5 at.% Mn	100	2.32 ± 0.24	324.3 ± 15.9	0.32	90.7 ± 11.6	1.21	2.19
S	Cu|Al-20.5 at.% Mn|Cu	100	5.67 ± 0.69	284.1 ± 5.6	0.32	94.9 ± 10.8	1.13	8.13

Table 3.2 Material properties used in the FEM model. Properties of PI are from the manufacturer (Dupont 2004) and those of Cu thin film are from reference (Yu et al. 2004), while the properties of the Al-Mn alloy layer are from experiments as listed in Table 3.1.

Material	E (GPa)	ν	σ_Y (MPa)	σ_f (MPa)
PI	2.5	0.34	69	-
M20	103.6	0.32	-	321.7
Cu	127	0.34	881.98	-

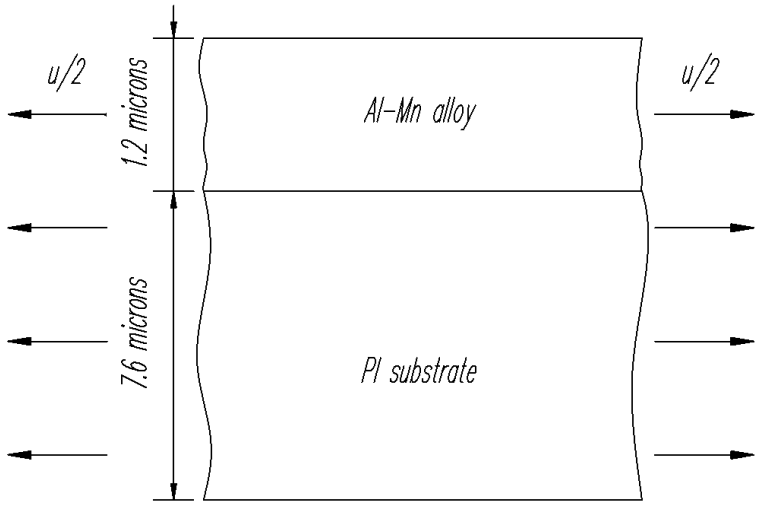

Figure 3.1 Sketch of monolithic sample geometry (M5, M11 and M20).

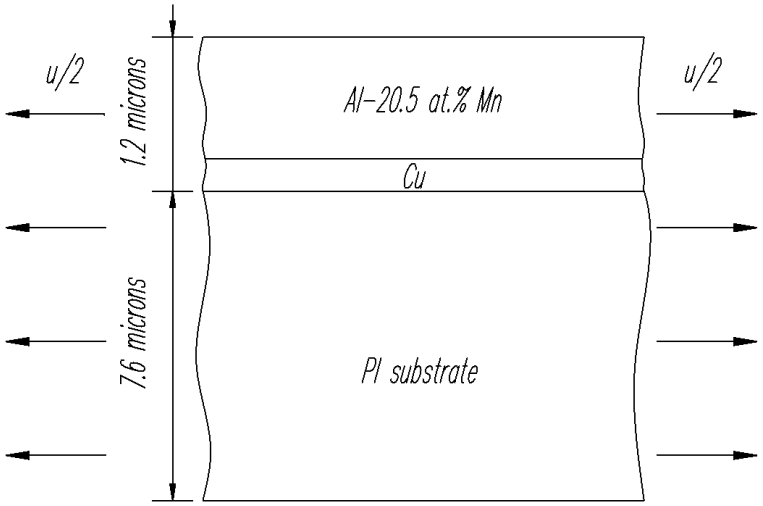

Figure 3.2 Sketch of bilayered sample geometry (B1 and B2).

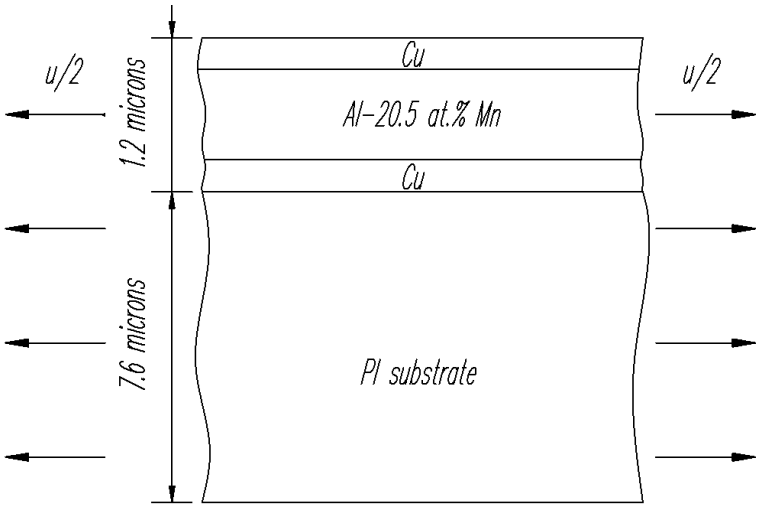

Figure 3.3 Sketch of trilayered sample geometry (S).

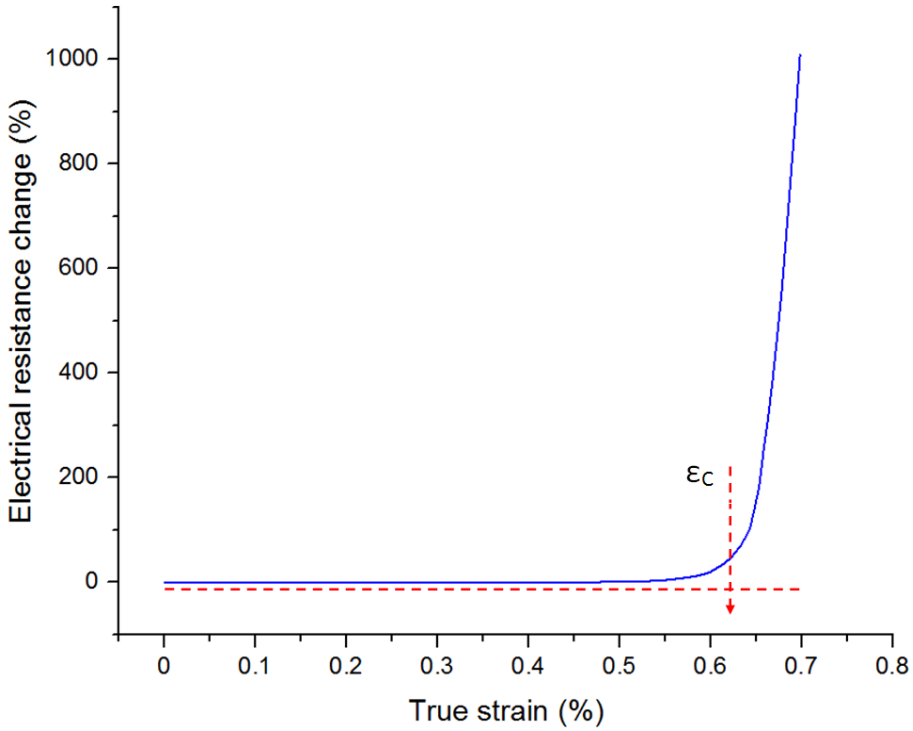

Figure 3.4 Evolution of electrical resistance change (defined as $(R-R_0)/R_0$, where R_0 is the initial electrical resistance of the film) of a monolithic Al-5.2at.%Mn (sample M5) as a function of strain.

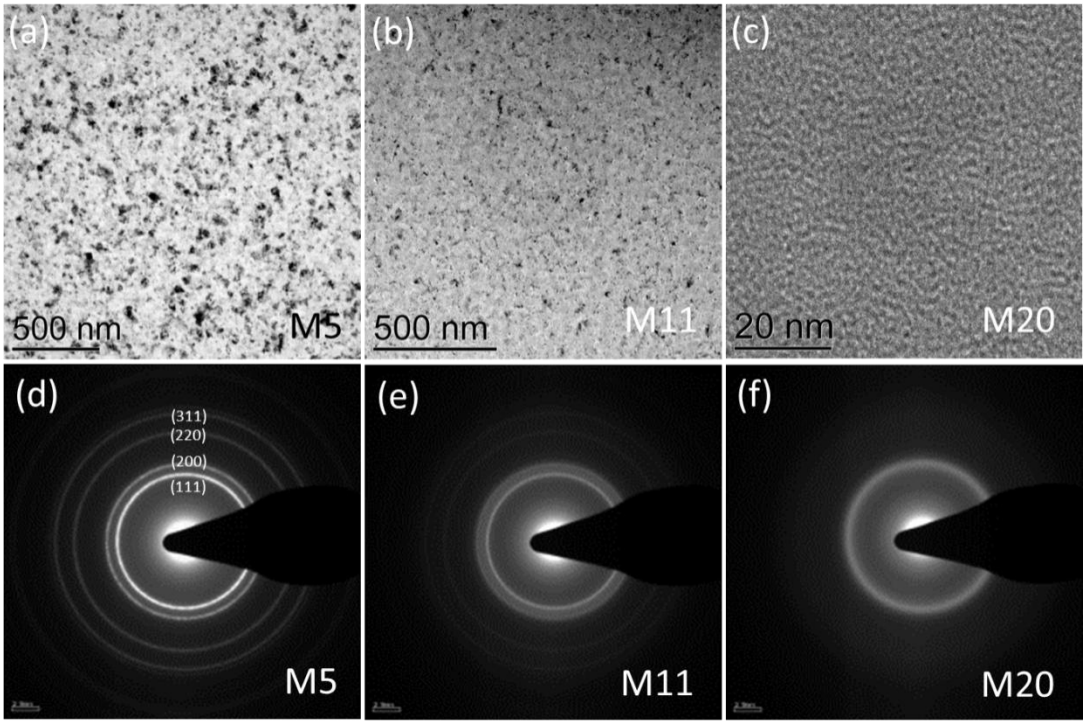

Figure 3.5 (a-c) TEM images and (d-f) corresponding SAD patterns of as-deposited monolithic Al-Mn films with various Mn % as defined in Table 3.1.

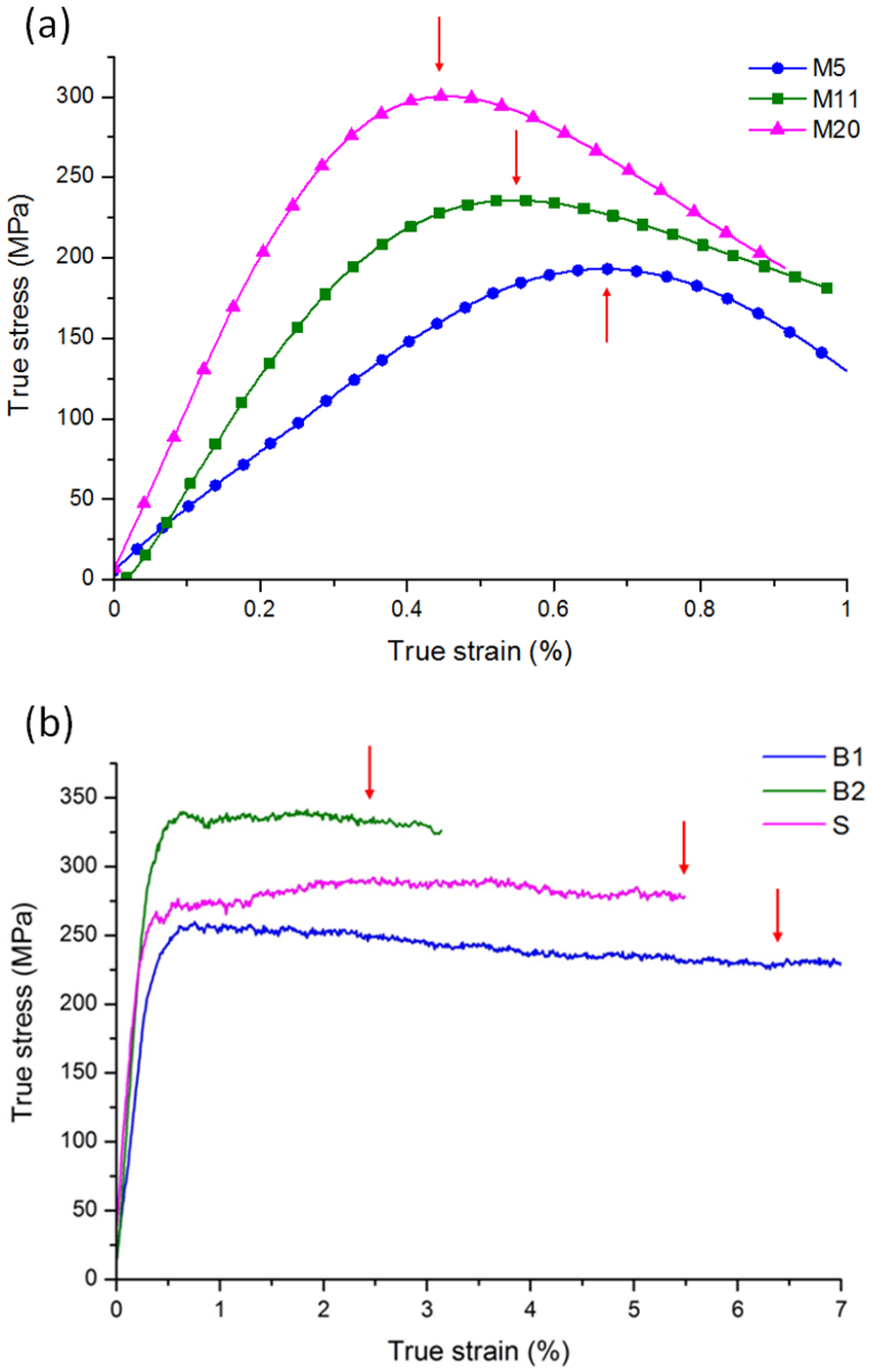

Figure 3.6 (a) Representative true stress-strain curves of M5, M11 and M20 and (b) B1, B2 and S samples. The arrows indicate the critical strains ε_c.

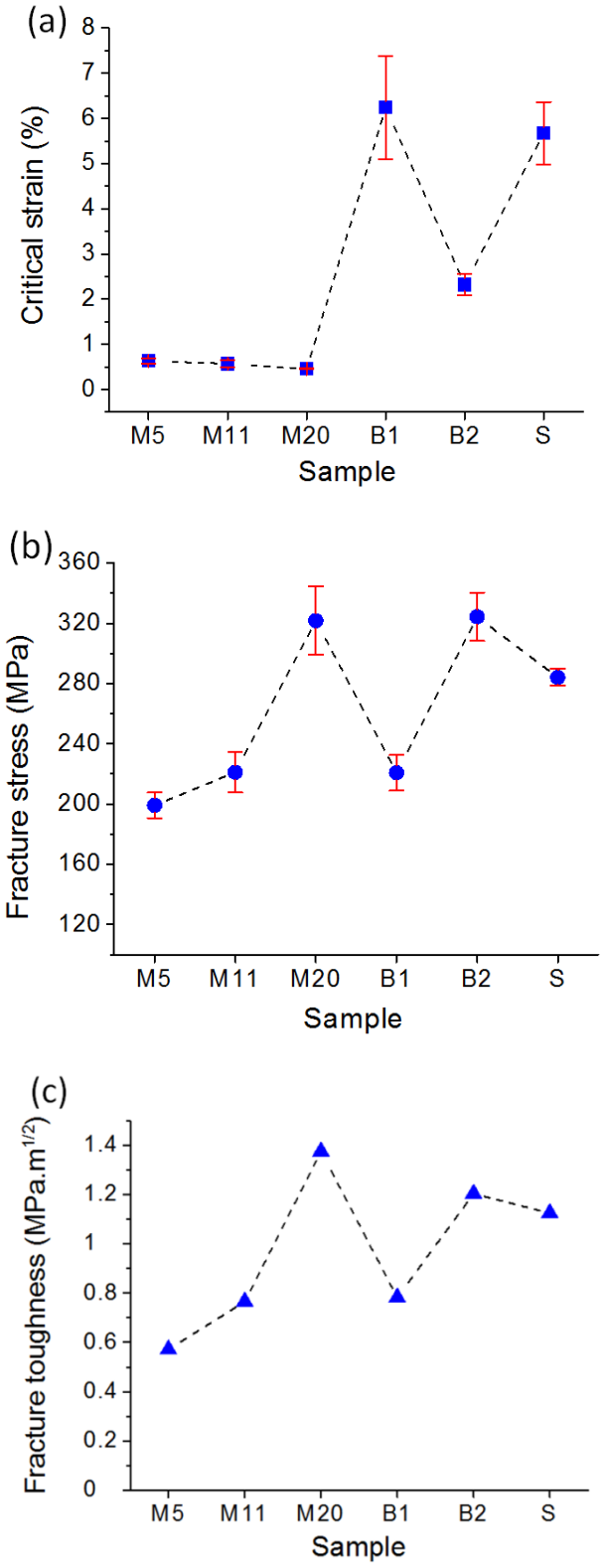

Figure 3.7 (a) Critical strain, (b) fracture stress, and (c) fracture toughness of all monolithic, bilayered, and trilayered samples. Error bars represent standard deviation obtained from at least four separate tests.

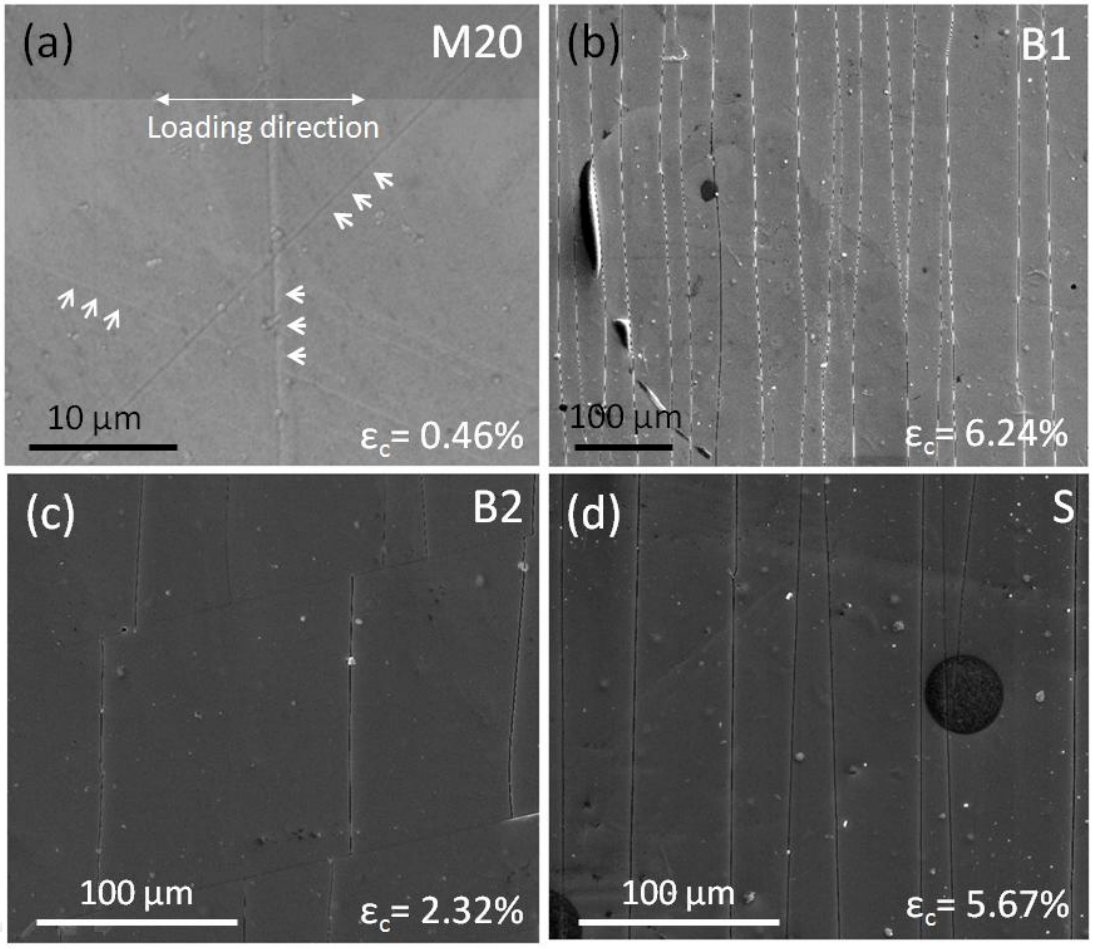

Figure 3.8 SEM images of sample (a) M20, (b) B1, (c) B2 and (d) S at its respective critical strains. Uniaxial loading is applied in the horizontal direction in all samples as shown in (a). White arrows in (a) show the extensive shear bands formed either inclined at an angle of ~ 45^o or perpendicular to the loading direction.

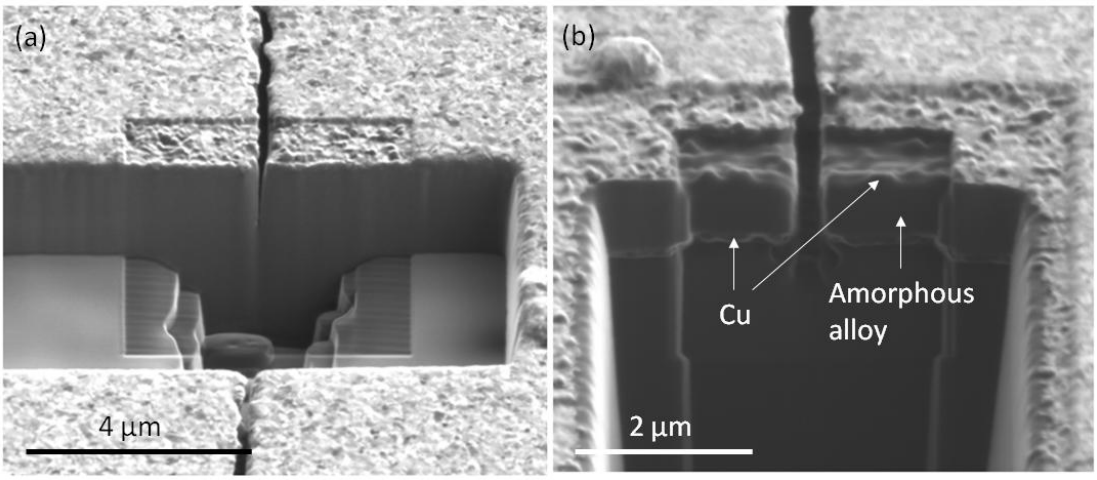

Figure 3.9 (a) and (b) Cross-sectional ion beam images of the S sample at its critical strain. Image (b) was obtained after extensive ion etching of the crack in (a) to reveal the sandwich structure.

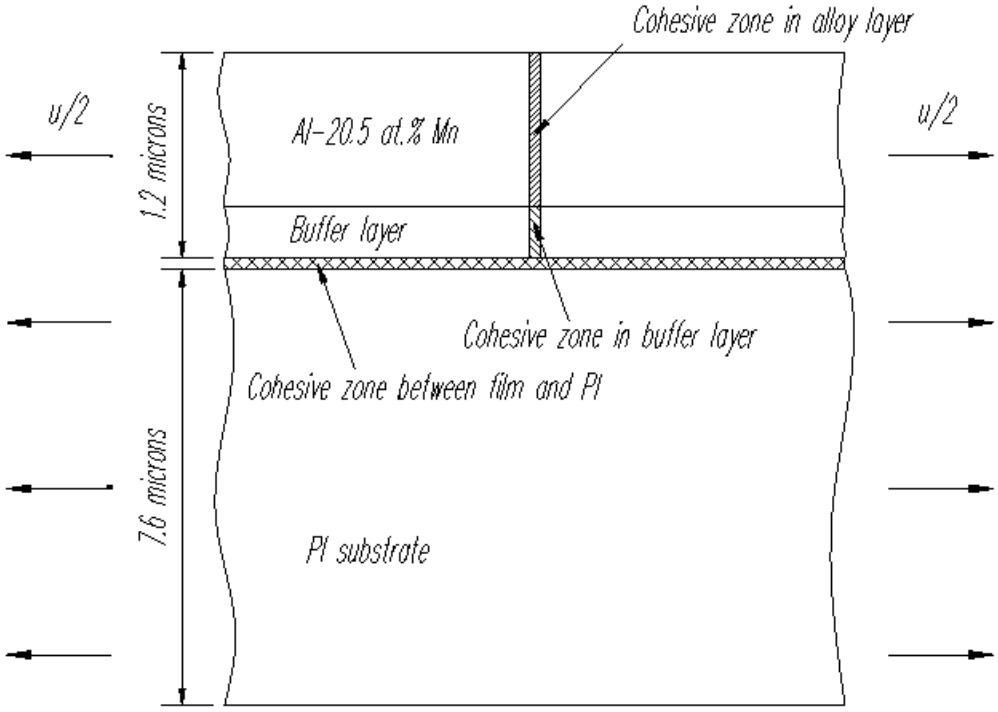

Figure 3.10 Sketch of a bilayered sample with cohesive zones.

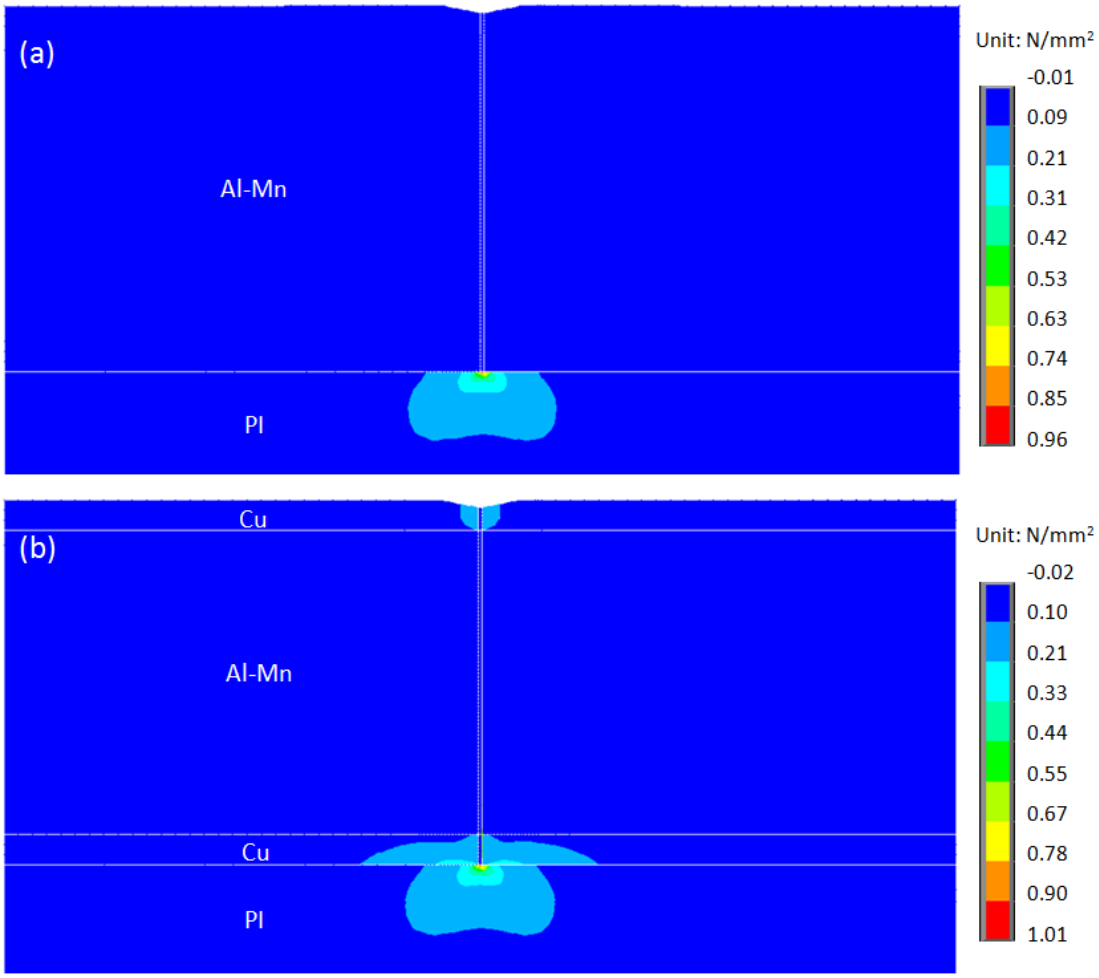

Figure 3.11 Elastic strain energy density distributions of sample (a) M20 and (b) S at a strain of 0.46%.

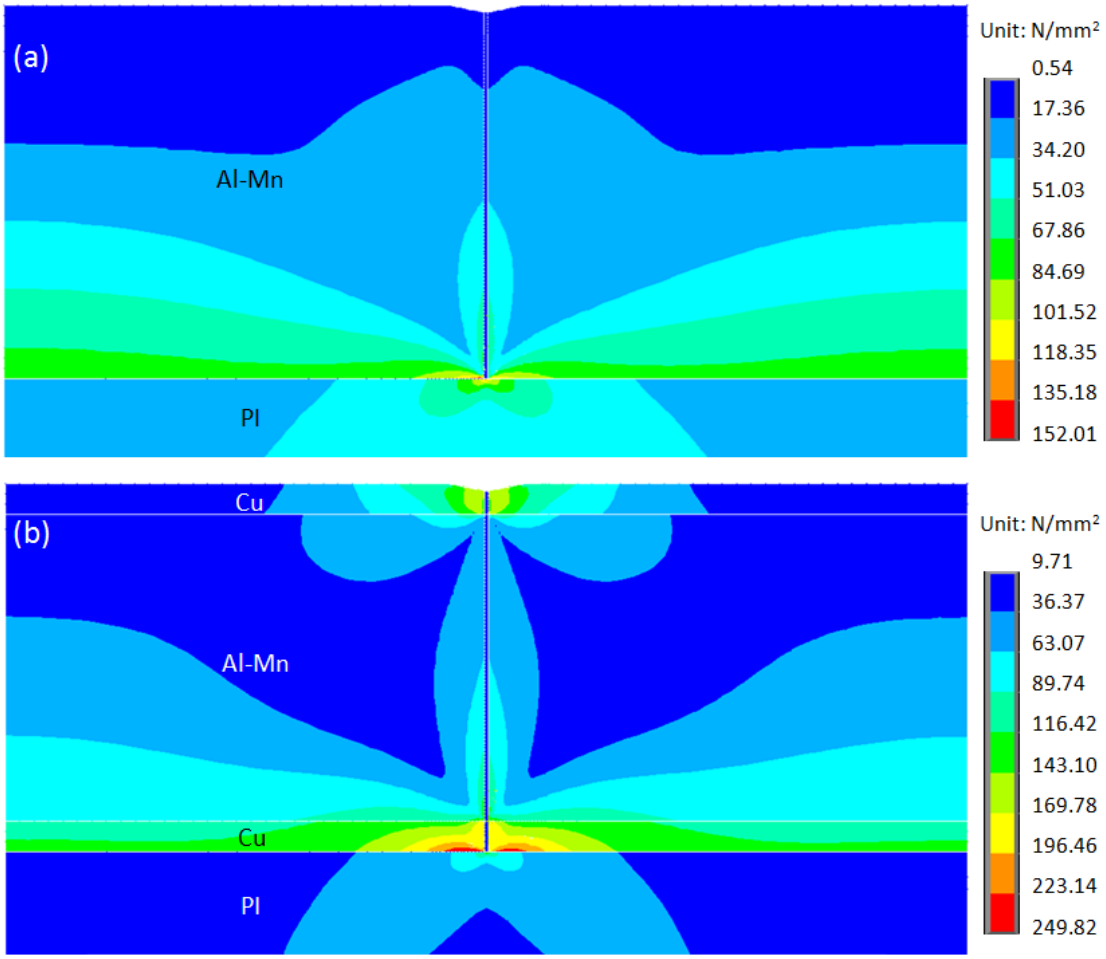

Figure 3.12 Equivalent stress distributions of sample (a) M20 and (b) S at a strain of 0.46%.

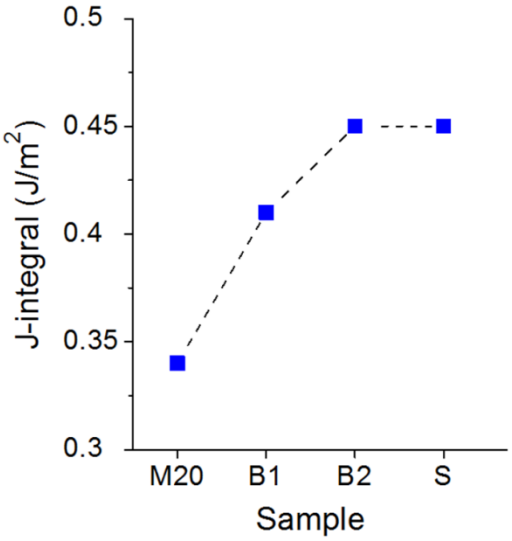

Figure 3.13 J-integrals of the film/substrate interface at the applied strain of 0.46%.

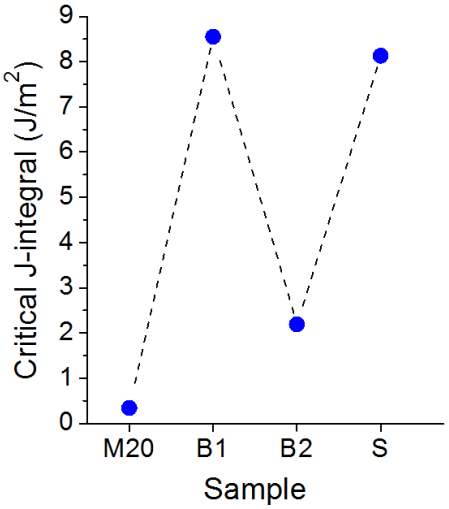

Figure 3.14 Critical J-integrals of the film/substrate interface of the sample M20, B1. B2 and S at their critical strains of 0.46%, 6.24%, 2.32% and 5.67%, respectively.

CHAPTER 4: EFFECTS OF SUBSTRATE ROUGHNESS AND BUFFER LAYER PROPERTIES ON THE INTERFACE ADHESION OF BRITTLE THIN FILMS ON POLYIMIDE SUBSTRATES

4.1 Introduction

Ductility and fracture resistance of metallic interconnect thin films coated on polymer substrates are strongly influenced by the film/substrate interface adhesion. It was shown that the improved metallic film/polymer substrate adhesion delays the interface debonding (George et al. 2005; Xiang et al. 2005). Therefore, the film is constrained by the substrate, retarding the strain localizations, such as neckings or the shear band formations in the film, which leads to a larger failure strain (George et al. 2005; Li et al. 2005b; Li et al. 2007a; Xiang et al. 2005; Zhang et al. 2008b). On the other hand, if the metallic film delaminates from the substrate because of weak adhesion, the support from the substrate is lost, and the film becomes freestanding and is free to form a neck, resulting in the failure at a smaller strain (Li et al. 2005b; Lu et al. 2009; Xiang et al. 2005; Zhang et al. 2008b). To increase the toughness of the interface, the interface has to play an important role in releasing the stresses to the adjacent layer, resulting in a smaller probability of delamination (He et al. 1993; Odette et al. 1992; Was et al. 1996). This observation results from two mechanisms: either the debonding of the interface (if the interface adhesion is weak) or the plastic slip normal to the crack plane (if one of the adjacent materials is ductile) (Was et al. 1996).

Various strategies have been applied to enhance the metallic film/polymer substrate interface adhesion. The strategies involve mechanical and design parameters including interface roughness, material and thickness of the adjacent buffer layer (Dauskardt et al. 1998; Frank et al. 2009; Lin et al. 2008; Misra et al. 2005; Schuh et al. 2007; Xu et al. 2011). Despite the recent progress, there have been very limited attempts to work on the ductility and fracture behavior of amorphous brittle film coated on polymer substrates, especially under tensile loading conditions.

Such considerations have motivated us to improve the situation. Since a strong bonding between the film and the polymer substrate is critical to maintain high ductility and fracture resistance for such systems, this chapter will evaluate strategies to improve the adhesion of the film/polymer interface including roughening the surface of the polymer substrate, adding a buffer layer and then tuning its thickness. The investigated system is 7.6 μm PI substrate magnetron sputtering coated with 1.2 μm Al-Mn alloy thin film in which the crystallinity of the film was tuned by varying Mn concentration in the alloy. A homogenous brittle amorphous phase was obtained with 20.5 at.% Mn addition, confirmed by energy dispersive spectra (Ruan et al. 2009). Using the same procedure described in chapter 3, tensile tests of monolithic Al-Mn alloy coated on PI were performed to obtain its mechanical properties. FE simulation is the main focus of this chapter.

4.2 Experimental Procedure

First, tensile experiments were conducted to obtain the critical strain (ε_c), i.e. the macroscopic strain, which characterizes the microcrack formation (as opposed to rupture), by electrical resistance change method; and the stress-strain curve of Al-20.5 at.% Mn alloy (hereafter referred as Al-Mn for simplicity) thin film coated on PI substrate (named as sample

M), from which mechanical properties including fracture stress (σ_f) and elastic modulus (E) were extracted.

The experiments were performed with the same procedure as mentioned in section 3.2. The samples of 1.2 μm Al-Mn alloy thin films were sputtered on 7.6 μm thick PI foils. Microstructure of as-deposited monolithic Al-Mn samples was characterized using TEM and SAD and it shows a completely amorphous phase. Uniaxial tensile tests (DTS, National Instruments) were carried out and the critical strain ε_c was also obtained by electrical resistance change method. Fig. 4.1 shows a typical evolution of electrical resistance change during a tensile test, where ε_c is defined at the point where the electrical resistance deviated from the ideal curve (Lu et al. 2007; Niu et al. 2007). With the use of DIC method, the true stress-strain curve of a monolithic Al-Mn alloy sample was obtained and shown in Fig. 4.2. The mechanical properties of the Al-Mn alloy were extracted and listed in Table 4.1.

Second, to see the potential effects of the rough PI substrate and the buffer layer on the thin film/substrate adhesion, tensile tests were conducted on the monolithic Al-Mn and bilayer 20 nm Cr|Al-Mn films coated on both flat and rough PI substrates. Table 4.2 shows the four samples used in our experiments and their experimental critical strains and simulation J-integral values (will be mentioned latter).

To get rough PI substrates of 100 nm Ra (i.e. arithmetic average of absolute values of surface profile), oxygen plasma etching (Plasma-Therm PECVD/RIE) was operated at oxygen flow of 50 cc/s, 20 Torr process pressure and 35 W of RF power for 120 seconds in RIE mode. The roughness was measured by Dektak D150 profiler. All four samples were tensile tested with the same procedure and devices. Their experimental critical strains and simulation J-integral values are shown in Table 4.2, except the critical strain of samples MCr20. The film/substrate

adhesion of those samples was too weak, so the films delaminated whenever they were in contact with hands.

The above four samples were chosen to show the correlation between the experimental critical strains and the simulated J-integrals, which represent the film/substrate adhesion (Anderson 2005; Rice et al. 1965; Tran et al. 2013). The ductility of a metallic thin film/substrate system in tensile tests is governed by three main factors including dislocations emitted from the crack tip (Hsia et al. 1994; Zbib et al. 2011), the adhesion at the film/substrate interface (Dauskardt et al. 1998; Xiang et al. 2005; Zbib et al. 2011), and the dislocation-interface interaction (Zbib et al. 2011). If there exists a ductile buffer layer or if the film is a ductile material, dislocations emitted from the crack tip will blunt the crack tip and therefore reduce the tensile stress at the crack tip resulting in the suppression of the crack propagation process, since the crack tip stress is unable to reach the cohesive tensile strength of the interface (Hsia et al. 1994). In all chosen samples which are either brittle monolithic amorphous film (i.e. M and M-R) or buffered by a brittle layer (i.e. MCr20 and MCr20-R), the effects of dislocations can be neglected. Therefore, their experimental critical strains correlate to the film/substrate adhesion (hence, J-integrals) mainly.

Looking at the critical strains and J-integral values of M and M-R in Table 4.2, it can be seen that the J-integral values are directly proportional to the critical strains. The same tendency can be observed in the MCr20 and MCr20-R samples assuming that the critical strain of MCr20 is very low. The observation has motivated us to further investigate the effect of rough PI substrates and buffer layers on the Al-Mn amorphous metal thin film/substrate adhesion. Moreover, this correlation once again verified the simulation models.

4.3 Finite Element Simulations

In order to investigate systematically the effect of rough PI substrates on the amorphous metallic film/substrate interface adhesion, a series of simulations was performed categorized in two groups of samples: without and with 100 nm Ra roughness on the PI substrate surfaces. Among the two groups, to study the effects of buffer layers (material and layer thickness) on the adhesion, Al and Cr were used with layer thicknesses of 20, 50, 75 and 100 nm. This range of thicknesses was chosen based on some previous results. For example, the authors in reference (Wu et al. 2014) proved that the adhesion energy in Cu/Mo multilayers coated on PI remains low when the thickness of the ductile layer (i.e. Cu) is below ~25 nm and increases with the thickness. Zhang et al. (2011) studied the effect of layer thickness on the fracture behavior of Cu/Nb and Cu/Zr multilayers coated on PI. They found that the fracture mode of the mutlilayers is controlled by the constraining effect of the ductile layer (i.e. Cu) and the fracture toughness increases with its thickness and reaches a steady-state when the thickness is lager than 20 nm. Reducing the ductile layer thickness to less than ~15 nm, dislocation activities are greatly suppressed and their shielding effect is minimized, resulting in a significant reduction of deformability of the Cu layer or, in other words, the Cu layer becomes more brittle. This conclusion was confirmed by others (Misra et al. 2005; Was et al. 1996). Moreover, the authors in references (Frank et al. 2009; Park et al. 1998) showed that a 20 nm buffer layer can improve the adhesion between Cu/PI or alumina/PI. Lastly, Al and Cr were chosen to represent a more ductile (and softer), and more brittle (and stronger) material, respectively, compared to Al-Mn alloy. Table 4.3 shows all the samples used in simulations.

The properties of the Al-Mn alloy were obtained from our experiments (Table 4.1). The stress-strain curve of PI is obtained from the manufacturer specifications (Dupont 2004) and

materials properties of Al, Cr layers are from references (Cardarelli 2008; Cordill et al. 2010; Yu et al. 2004). All the metallic materials were assumed to have elastic-perfectly plastic behavior. The material properties used in the FEM models are summarized in Table 4.4.

The computational models based on FEM were performed using ANSYS (version 17). A two dimensional plane-strain model of the multilayered film on PI substrate under uniaxial tension was constructed, similar to those in references (Li et al. 2004; Li et al. 2005b; Li et al. 2007a; Lu et al. 2010; Zhang et al. 2008b) and verified by the results in reference (Zhang et al. 2008b). The total metallic film thickness h_T is 1.2 μm, in which the buffer layer thickness in the bi-layer samples ranges from 20, 50, 75 to 100 nm, and the PI substrate thickness is 7.6 μm. The length *l* of the film/substrate system was set at 3.12 μm. Similar to section 3.4 and Fig. 3.7, CZM was implemented to get the J-integral values of flat samples (samples without roughness on PI surface). A strain of 4.66% (i.e. critical strain of the sample MCr20-R, Table 4.2) was applied to all samples. Twelve contours were defined around the crack tip, which rested at the film/substrate interface, to get the converged J-integral values. Table 4.3 shows all the J-integral results.

To get the simulation of the rough PI samples, a FEM model of the bilayered system with rough PI substrate was constructed. For simplicity, the film/PI interface was assumed to be wavy with the idealized sinusoidal shape of the formula:

$$y = a\sin\frac{2\pi}{\lambda}x, \tag{4.1}$$

where a is the amplitude, λ is the wavelength and x is the horizontal coordinate. For the roughness of 100 nm Ra, λ and a take the values of 2 μm and 100 nm, respectively. The length *l* of model was equal to 2λ, i.e. two sinusoidal periods. The nominal strain of the system was then $u/l = u/(2\lambda)$.

Superior to the model in reference (Xu et al. 2011) where the film was simulated to be bonded to the wavy PI substrate, in this chapter the cohesive zones were introduced both inside the layers (at the crack) as well as at the film/substrate interface, similar to the above mentioned flat surface model. All the other geometry, material parameters and boundary conditions are the same as the flat surface model. The convergence analysis was performed again with the mesh to get the mesh-independent results. Fig. 4.3 shows the sketch of a bilayered rough sample with the cohesive zones and Table 4.3 shows all the J-integral results.

4.4 Results and Discussion

4.4.1 Effects of the Buffer Layer Material Properties on the Interface Adhesion

Fig. 4.4 shows J-integrals of M, M-R, MAl20, MAl20-R, MCr20 and MCr20-R samples. It can be seen that among the flat substrate samples, the one with Al buffer layer (MAl20) has the highest interface adhesion. This can be explained by the following mechanisms involving the stress, strain and plastic deformation. First, in the MAl20 and MCr20 samples, the higher equivalent stress of MAl20 (Fig. 4.5(a)) is distributed broadly in the Al-Mn alloy layer (1.2 μm) with the maximum value of about 200 MPa. Meanwhile, the higher equivalent stress concentrates in the buffer layer of Cr (20 nm) with the higher maximum value of 901 MPa (Fig. 4.5(b)), which obviously creates a higher traction at the interface, increasing the possibility of delamination. That is likely the reason why the interfacial adhesion of MAl20 is about three times higher than that of MCr20. Second, it can be seen that there is no yielding in the Al layer (since the equivalent stress in the Al layer is much lower than its yield strength, shown in Fig. 4.5(a)), while all the PI substrates yielded. The plastic strain distribution in sample MAl20 (Fig. 4.6(a)) shows a high plastic strain concentration (about 31%) near crack tip in the PI substrate while in MCr20 (Fig. 4.6(b)) there is only about 5% of plastic strain near crack tip within the

substrate PI layer. According to Was et al. (Was et al. 1996), the plastic deformation has a significant impact on the toughness of the interface in a multilayer system. A tough interface is attributed to extensive plastic work done at the crack tip during crack propagation. The substrate PI in MAl20 sample clearly shows the highest plastic deformation among the flat substrate samples. Based on the two discussions above, it can be postulated that in order to improve the interface adhesion of a brittle film (e.g. Al-20.5 at.% Mn) on a flat flexible PI substrate, a thin (e.g. 20 nm) ductile buffer layer (e.g. Al) of smaller yield strength than the fracture strength of the brittle film should be added in between the film and the substrate.

4.4.2 Effects of the Substrate Roughness on the Interface Adhesion

It has been shown that interface adhesion can be improved by roughening the substrate (Dauskardt et al. 1998; Ma et al. 1995). Results in Fig. 4.4 demonstrate that rough PI substrate can improve the interface adhesion within the three samples (M, MAl20 and MCr20). J-integral values of the monolithic M-R and MAl20-R have nearly doubled with the presence of substrate roughness. In MCr20-R, the interfacial adhesion increases 9 times compared with the flat substrate sample MCr20. Moreover, in comparison with its counterparts, i.e. M-R and MAl20-R, the interfacial adhesion of MCr20-R is about 5 and 1.5 times, respectively. Note that similar to MAl20, there is no yielding in the Al layer of MAl20-R. Hence the fractures in all 6 samples fall into the debonding mechanism as categorized in reference (Was et al. 1996). Dauskardt et al. (1998) showed that energy dissipation during the debonding was affected by the interface morphology due to the increase in frictional sliding of the surface asperities behind the debonding tip. A model in reference (Evans et al. 1989) also shows that the increased adhesion of a rough interface results from the extension of the frictional contact zone behind the debonding tip. Second, rough interface can reduce the tensile stresses along the film surface, thus

restraining the channel cracking of the film as well as the debonding (Xu et al. 2011). Lastly, high energy dissipation of the film by plastic deformation could be considered a toughening mechanism that contributes to the enhanced interface adhesion (Dauskardt et al. 1998). The energy dissipation mechanism involves the plastic deformation of the ductile bonding layer(s) and the interaction between the crack faces behind the debonding tip. Fig. 4.7 shows the plastic strain energy densities of the bi-layer rough samples. It can be seen that the plastic strain energy density of the PI substrate in MCr20-R is two times that of MAl20-R. That means the energy dissipated to the substrate in MCr20-R is more than that of MAl20-R, making the interface adhesion in MCr20-R higher. Therefore, it is postulated that with the condition of the rough PI substrate, higher adhesion of an amorphous brittle film/PI interface can be obtained by having a buffer layer with higher strength and stiffness.

4.4.3 Effects of the Buffer Layer Thickness on the Interface Adhesion

Fig. 4.8 shows the effects of buffer layer (Al and Cr) thickness on the interface adhesion. While the behavior of MAlx and MAlx-R (x = 20, 50, 75 and 100) samples is insenstitive to buffer layer thicknesses, MCrx and MCrx-R samples reach their J-integral maximum at x = 75 nm and the substrate roughness takes its best effect on the adhesion with Cr buffer layer. We will thereafter focus on the MCr75-R, which improves the interface adhesion of the base sample M by almost 20 times and is therefore the most beneficial case. By systematically increasing the thickness of the Cr film, the combined elastic energy stored in the two adjacent layers increases, making it higher than the critical condition sufficient to delaminate the interface (Wei et al. 1997). It can be seen that the Cr layers in MCr75 and MCr75-R possess the highest values of elastic energy density compared to MCrx (not shown) and MCrx-R (x = 20, 50 and 100) (Fig. 4.9), respectively. That means the energy is absorbed more by the thicker Cr layers until the

maximum energy absorption ability is reached at x = 75 in MCr75 and MCr75-R samples. In other words, the Cr layers of 75 nm dissipate the highest amount of strain energy, increasing the ability of preserving ductility and delaying the final failure of the whole system, similar to that reported in reference (Kou et al. 2014).

4.5 Conclusions

Interface adhesion of amorphous Al-Mn alloy thin films coated on PI substrates was improved by adding buffer layer (Al or Cr) and roughening the substrates. The analysis was done by tensile testing and FE simulations. Among the flat substrate samples with a fixed buffer layer thickness (20 nm), the one with Al buffer layer (MAl20) has an interfacial adhesion three times higher than that of Cr (MCr20). It is postulated that to improve the interface adhesion of the system (without roughing the PI), a thin (e.g. 20 nm) ductile buffer layer (e.g. Al) of smaller yield strength than the fracture strength of the amorphous film could enhance interface adhesion via stress concentration and plastic deformation mechanisms. On the other hand, introducing substrate roughness enhances interfacial adhesion of MCr20-R nine times stronger than the flat one (MCr20). Moreover, interface adhesion of MCr20 is about 5 and 1.5 times stronger than M-R and MAl20-R, respectively. Hence, it can be predicted that with the condition of the rough PI substrate, higher adhesion can be obtained by having a buffer layer with higher strength and stiffness (than the brittle film).

When the buffer layer thickness was varied, MAlx and MAlx-R (x = 20, 50, 75 and 100) samples show their independency on buffer layer thicknesses, while the MCrx and MCrx-R samples reach their J-integral maximums at a thickness of 75 nm. Particularly, MCr75-R improves the interface adhesion of the base sample M to almost 20 times and is therefore the most beneficial case. It was found that the Cr buffer layer reaches its highest amount of strain

energy dissipation ability at the thickness of 75 nm, maximizing the ability of preserving ductility and delaying the final failure of the whole system.

The results of the present work may shed light on the interfacial engineering strategies for improving interface adhesion for flexible electronics, whose performance requires reasonable interface adhesion of amorphous metallic films on polymer substrates. The author therefore calls for further experimental studies to verify the predictions.

4.6 Tables and Figures

Table 4.1 Composition and mechanical properties of monolithic amorphous Al-Mn thin films deposited on PI substrates. The critical strain (ε_c) was obtained from electrical resistance change method (Fig. 4.1) while fracture stress (σ_f) and elastic modulus (E) were measured from the stress-strain curves of uniaxial tensile tests. The Poisson's ratio (ν) was estimated using the rule of mixtures from pure Al and Mn (Cardarelli 2008).

Sample ID	Composition	ε_c (%)	σ_f (MPa)	ν	E (GPa)
M	Al-20.5 at.% Mn	0.46 ± 0.01	321.7 ± 22.7	0.32	103.6 ± 2.9

Table 4.2 Samples used in experiments to get their experimental critical strains.

Sample ID	Film composition	PI roughness - Ra (nm)	h_{Cr} (nm)	ε_c (%)	J-integral (J/m^2)
M	Al-20.5 at.% Mn	-	-	0.46 ± 0.01	0.69
M-R	Al-20.5 at.% Mn	100± 6	-	1.39± 0.1	1.82
MCr20	Cr|Al-20.5 at.% Mn	-	20± 5	-	0.96
MCr20-R	Cr|Al-20.5 at.% Mn	100± 6	20± 5	4.66	8.93

Table 4.3 Samples used in simulations to get their J-integral values.

Sample ID	Composition of film	PI roughness - Ra (nm)	Buffer layer thickness (nm)	J-integral (J/m^2)
M	Al-20.5 at.% Mn	-	-	0.69
M-R	Al-20.5 at.% Mn	100	-	1.82
MAl20	Al|Al-20.5 at.% Mn	-	20	3
MAl50	Al|Al-20.5 at.% Mn	-	50	2.97
MAl75	Al|Al-20.5 at.% Mn	-	75	2.98
MAl100	Al|Al-20.5 at.% Mn	-	100	3.02
MAl20-R	Al|Al-20.5 at.% Mn	100	20	5.97
MAl50-R	Al|Al-20.5 at.% Mn	100	50	5.15
MAl75-R	Al|Al-20.5 at.% Mn	100	75	4.9
MAl100-R	Al|Al-20.5 at.% Mn	100	100	4.75
MCr20	Cr|Al-20.5 at.% Mn	-	20	0.96
MCr50	Cr|Al-20.5 at.% Mn	-	50	2.65
MCr75	Cr|Al-20.5 at.% Mn	-	75	3.54
MCr100	Cr|Al-20.5 at.% Mn	-	100	2.92
MCr20-R	Cr|Al-20.5 at.% Mn	100	20	8.93
MCr50-R	Cr|Al-20.5 at.% Mn	100	50	12.26
MCr75-R	Cr|Al-20.5 at.% Mn	100	75	13.62
MCr100-R	Cr|Al-20.5 at.% Mn	100	100	12.18

Table 4.4 Material properties used in the FEM model.

Material	E (GPa)	ν	σ_Y (MPa)	σ_f (MPa)
PI	2.5	0.34	69	-
Al-20.5 at.% Mn	103.6	0.32	-	321.7
Al	70.2	0.345	225.4	-
Cr	279	0.21	-	1618.2

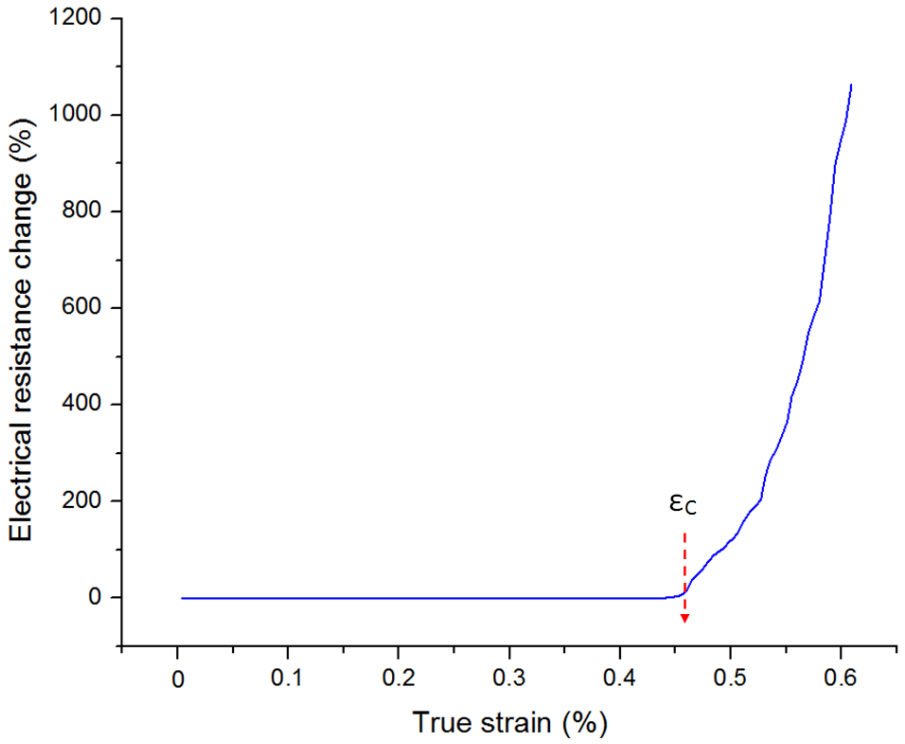

Figure 4.1 Evolution of electrical resistance change (defined as $(R-R_0)/R_0$, where R_0 is the initial electrical resistance of the film) of a monolithic Al-Mn (sample M) as a function of strain. The arrow indicates critical strain ε_c.

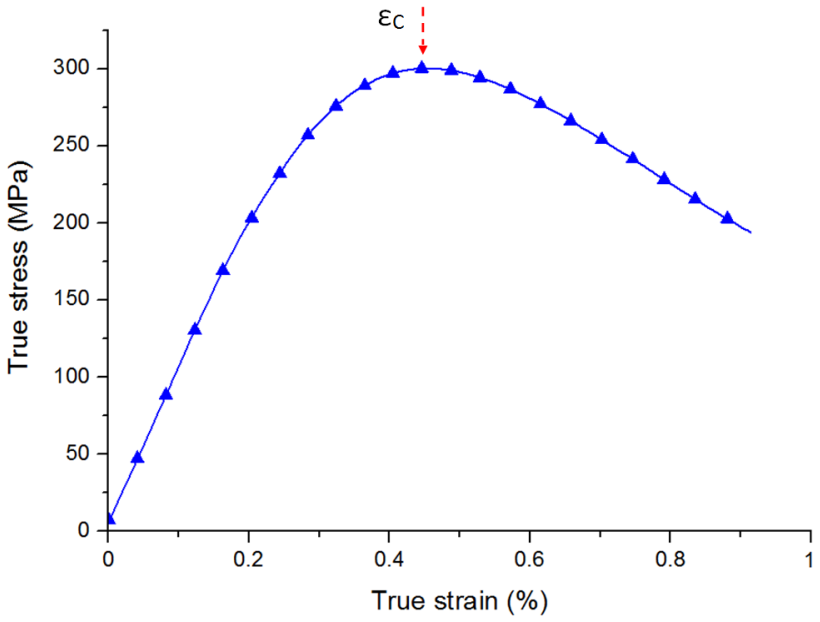

Figure 4.2 Representative true stress-strain curve of sample M. The arrow indicates critical strain ε_c.

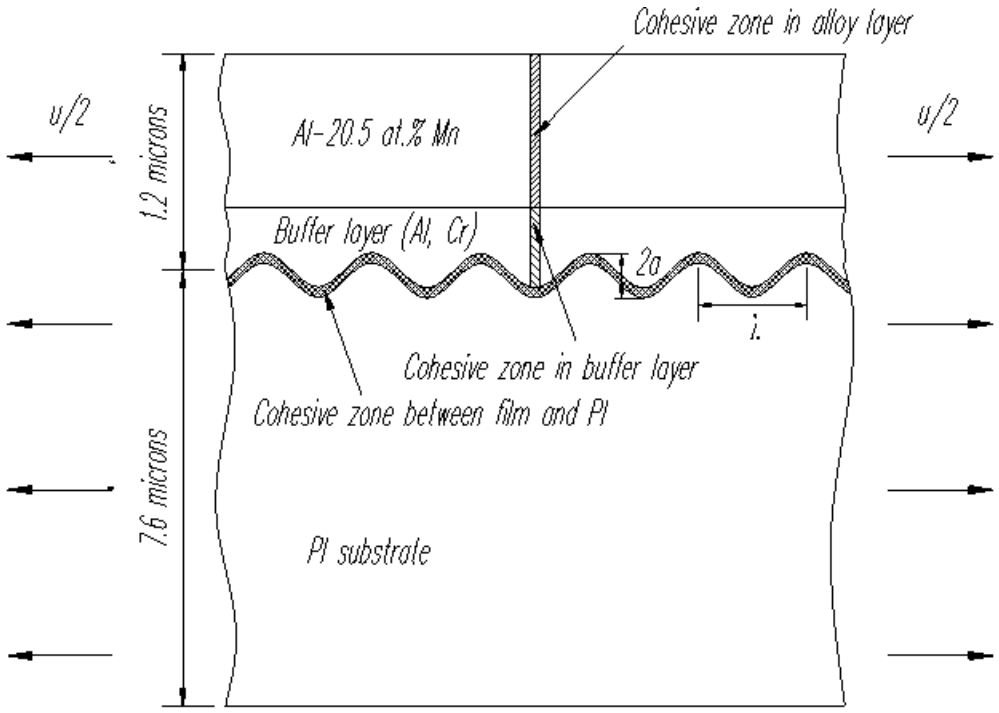

Figure 4.3 Schematic illustration of a bilayered rough sample with cohesive zones.

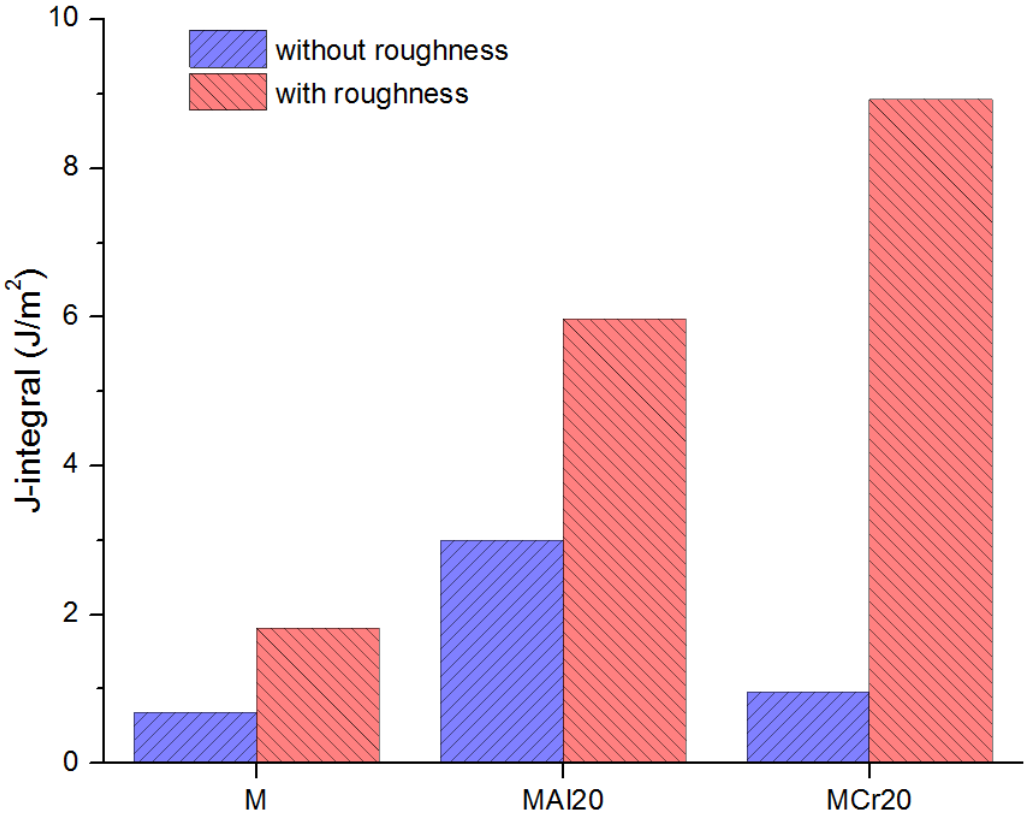

Figure 4.4 J-integrals of flat samples (M, M-R, MAl20) and rough samples (MAl20-R, MCr20 and MCr20-R).

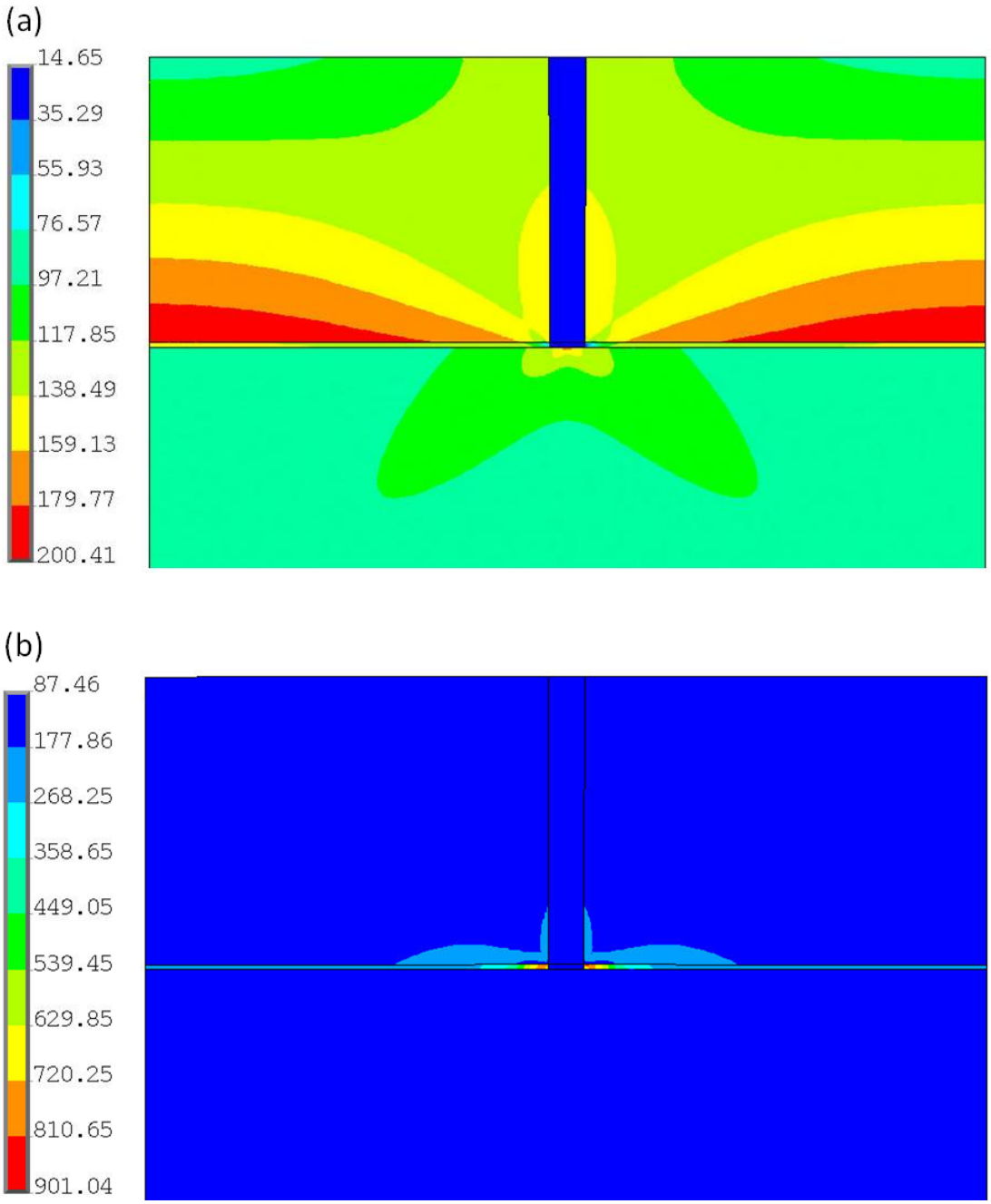

Figure 4.5 Equivalent stress (MPa) distributions of the (a) MAl20 and (b) MCr20 samples.

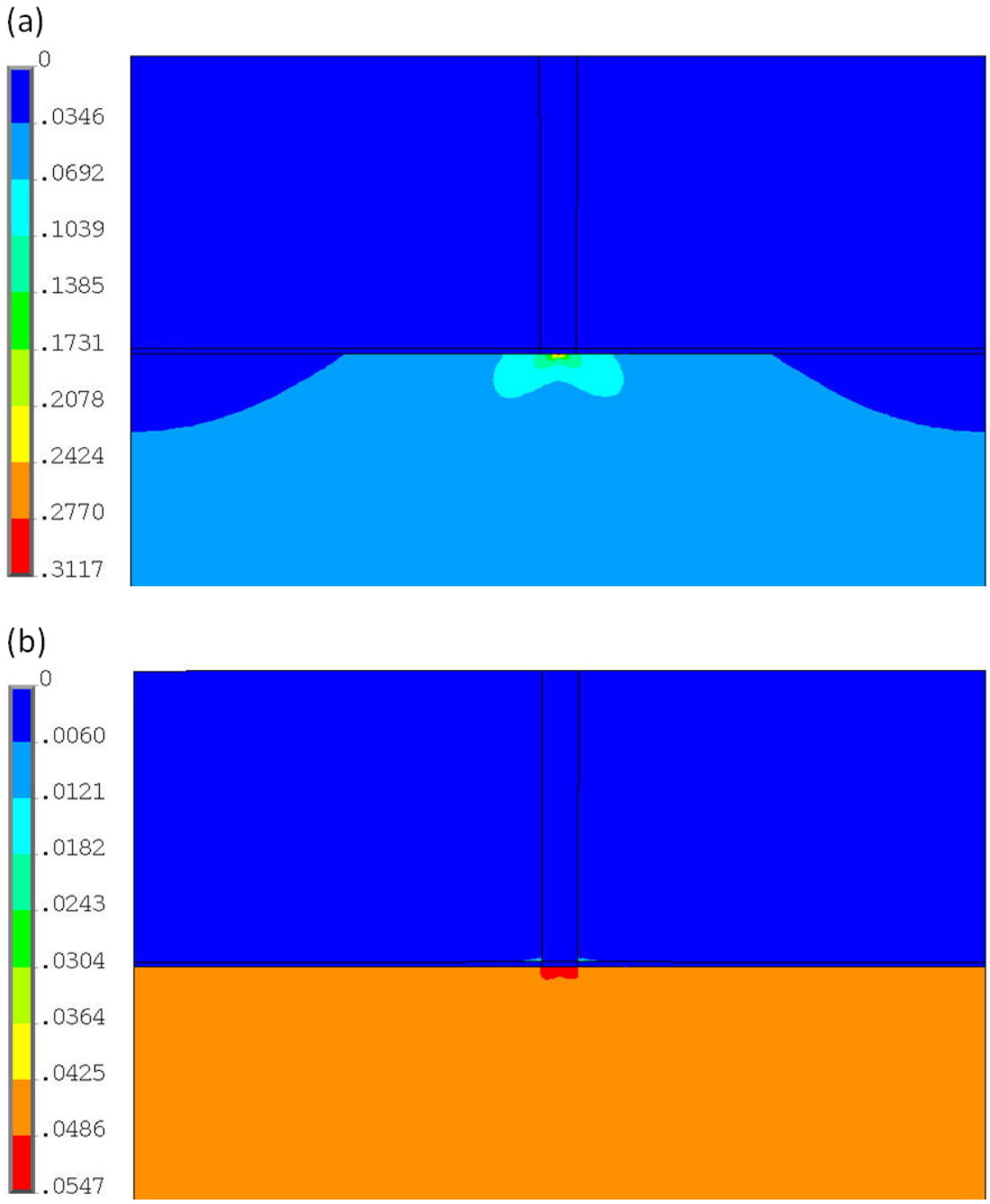

Figure 4.6 Plastic equivalent strain distributions of the (a) MAl20 and (b) MCr20 samples.

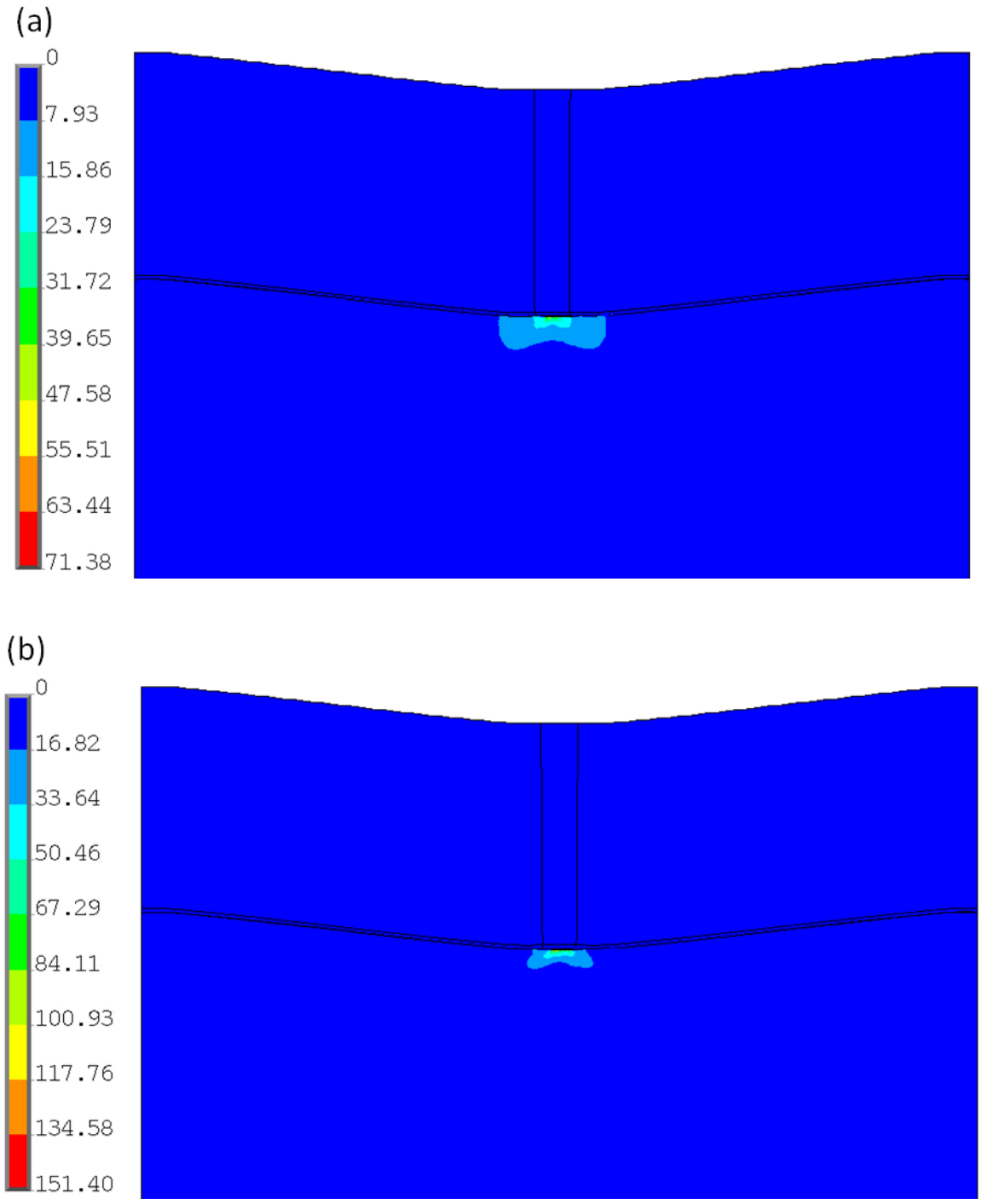

Figure 4.7 Plastic strain energy densities (N/mm^2) of the three rough samples (a) MAl20-R and (b) MCr20-R.

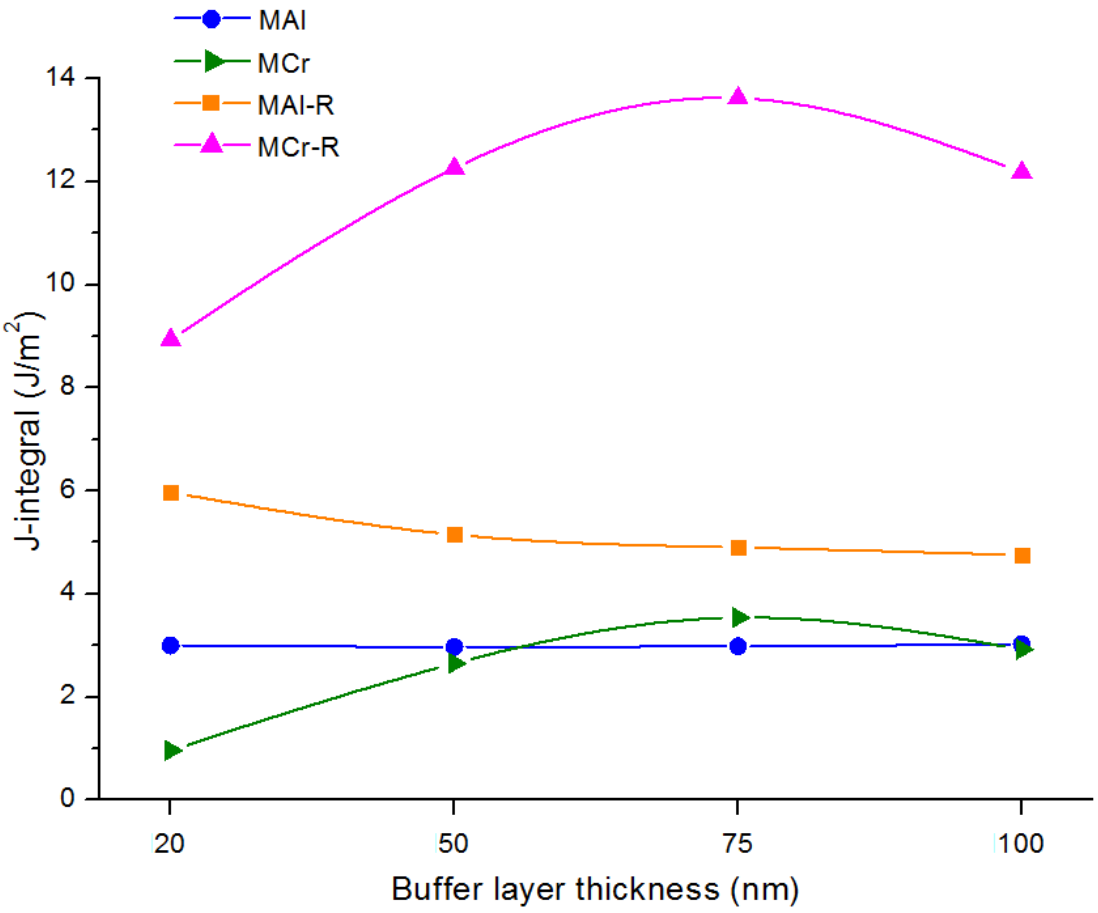

Figure 4.8 Dependence of the J-integrals on the buffer layer thicknesses.

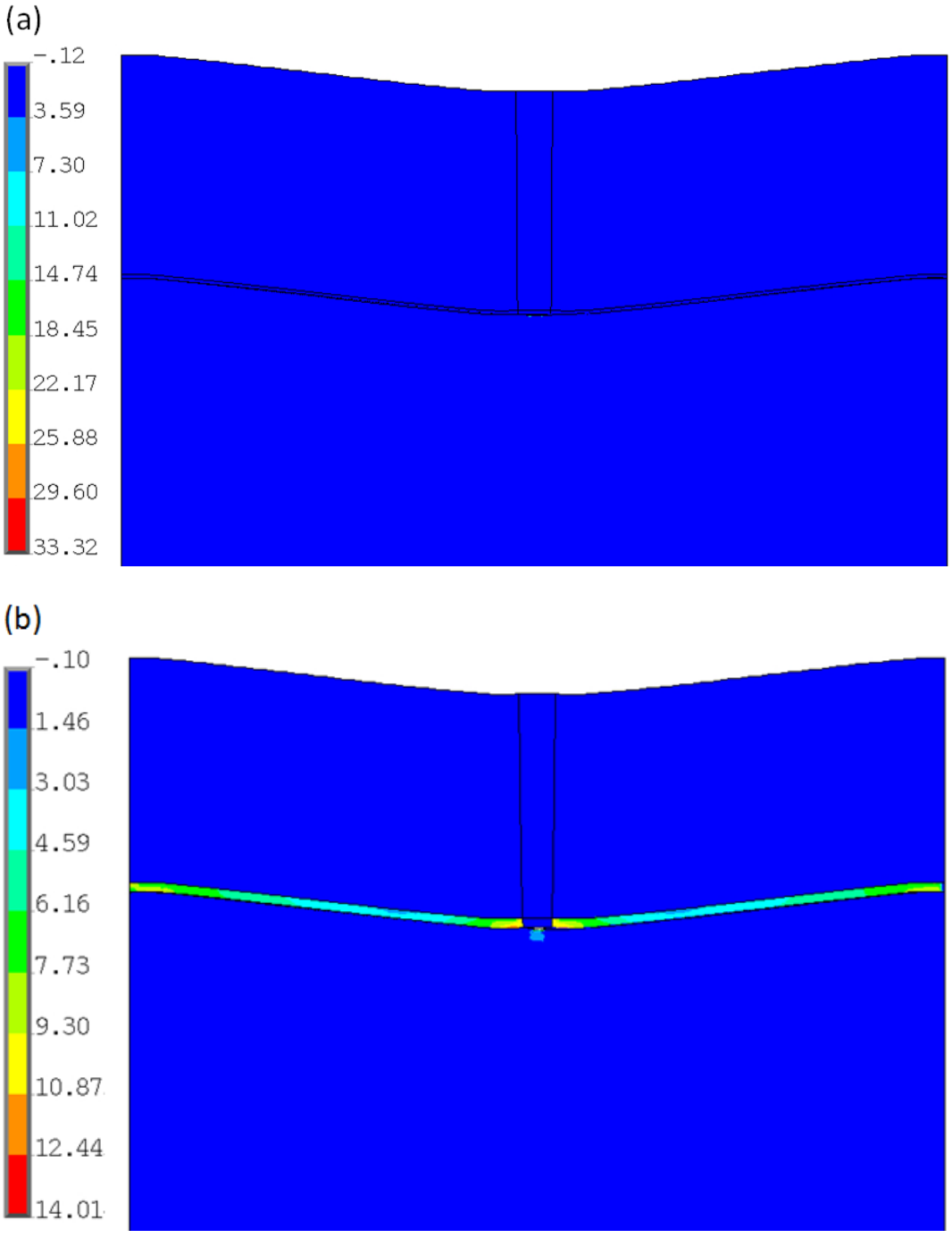

Figure 4.9 Elastic strain energy densities (N/mm^2) of the rough samples with Cr buffer layers (a) MCr20-R, (b) MCr50-R, (c) MCr75-R and (d) MCr100-R.

(c)

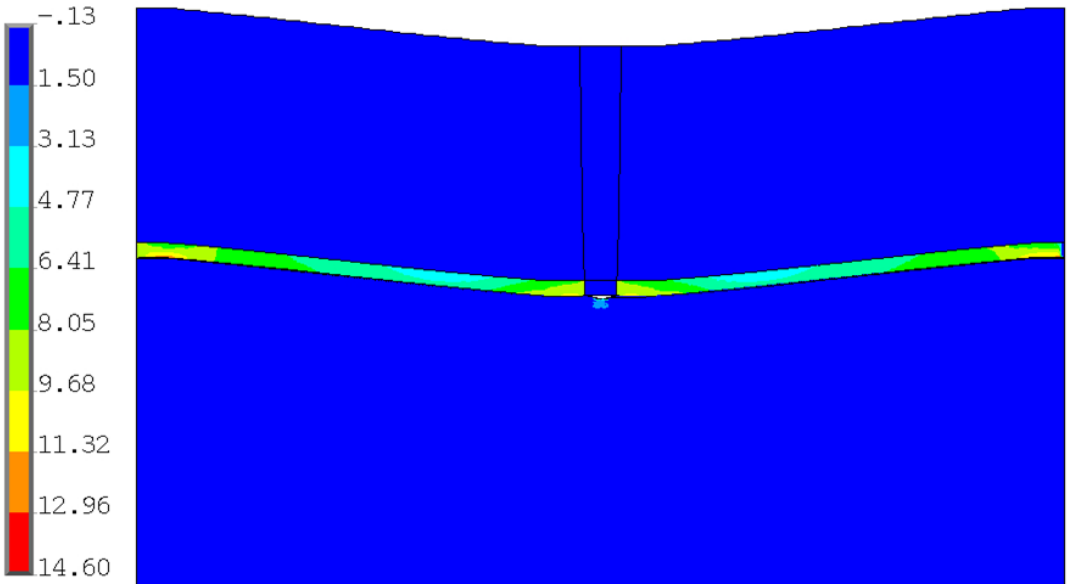

(d)

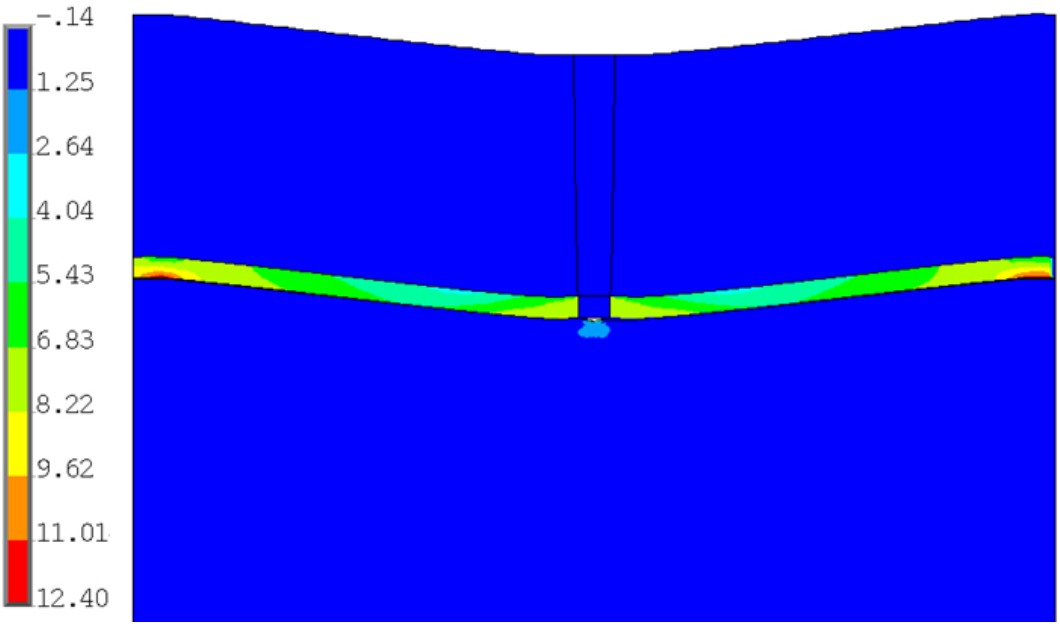

Figure 4.9 (continued).

CHAPTER 5: EFFECTS OF TEMPERATURE, MOISTURE AND MODE-MIXITY ON COPPER LEADFRAME/EPOXY MOLDING COMPOUND INTERFACIAL FRACTURE TOUGHNESS

5.1 Introduction

There have been several studies addressing the adhesion between Cu and EMC. Wong et al. (2006) used an atomic force microscope to characterize nano-scale adhesion forces in the Cu/SAM/EMC system. Fan et al. (2005) used a series of button shear tests along with the FEM to evaluate the interfacial adhesion between the EMC and Cu. Weidong et al. (2003) performed standard tensile tests for determining the interfacial fracture toughness of Cu/epoxy, while monitoring the crack length. They also performed fatigue tests to study interfacial delamination, followed by fatigue crack propagation. Chan et al. (2009) used Fourier transform infrared multiple internal reflection technique to detect moisture at the epoxy/Cu interface.

In this chapter, based on experiments and numerical simulations, a fast, simple and comprehensive methodology is proposed to investigate the interfacial delamination propagation and characterize the fracture toughness of the interface between Cu leadframe and EMC. In fracture mechanics' energy criterion approach, the crack propagates when the strain ERR G, which is the driving force for the crack propagation, is equal to its critical value G_c, known as interfacial fracture toughness. The values of G_c were calculated by the FE simulations. Temperature, moisture and mode-mixity effects on the leadframe/EMC adhesion (i.e. interfacial fracture toughness) were then investigated.

Although analytical expressions for the total ERR are available for some simple interfacial crack problems (Hutchinson et al. 1991), they involve considerable mathematical complexity. For complicated geometries, or loading conditions, analytical expressions may be unavailable and need to be solved numerically. Fortunately, the total ERR can be obtained using FE-based techniques, such as VCCT, VCE, J-integral, CZM, etc. Among these methods, only VCCT and CZM provide information about the mode-mixity, giving components of the ERR. Since VCCT has been successfully used to obtain both the total ERR and the mode-mixity for an interface crack, within the context of LEFM (to be discussed later), this work focuses on the VCCT and uses other methods as references.

5.2 Experimental Procedure

5.2.1 Sample Preparation

The samples were made from Cu leadframe and EMC. Various raw material ingredients were added to an EMC in order to meet the requirements of reliability, physical properties and moldability. The typical ingredients were phenolic resins, epoxy resins, fused silica as filler, coupling agents, curing promoter, and a release agent, all of which influence the adhesion strength and moldability of the resulting product. These raw materials were mixed and kneaded under heat into a homogeneous mixture in a kneader or a roll mixer. Generally, the materials were cooled, while kneaded into a sheet, and then pulverized. The powder material was pelletized into pellets, which were used in the transfer molding step. Commercial EMC pellets were provided by the vendors and kept in the refrigerator at freezing temperature (below -10 °C) to avoid undesired chemical changes, or contamination. The composition of the EMC investigated in this chapter is shown in Table 5.1. A leadframe is a thin layer of metal that connects the wiring from tiny electrical terminals on the semiconductor surface to the large-scale

circuitry in electrical devices and circuit boards. The leadframe used in this study is a Cu-based alloy with the chemical composition listed in Table 5.2.

Transfer molding is normally the preferred method for encapsulating or packaging a semiconductor chip with an EMC. It is generally a fast, consistent manufacturing technique that results in high-quality parts. This relatively simple process can be simply automated, which makes it a suitable choice for a lean manufacturing line (Komori et al. 2009). The transfer molding process used for the bi-material samples was similar to that for the plastic encapsulated microcircuits including the following steps:

+ Set the leadframe (substrate) connected to the semiconductor chip into the cavities of a heated mold;

+ Set the molding compound tablet into the pot of the molding machine;

+ Close the mold die tightly and, melt the molding compound under mold temperature conditions of 170-180 °C, and pour it into the mold under pressure;

+ After applying pressure for 45-90 seconds, when the molding compound has been fully cured, open the mold and release the molded parts. This completes the encapsulation process.

To fabricate the bi-material samples, leadframe plates were machined into 48×10×0.4 mm^3 strips and molded. After the transfer molding, the samples were placed in an environmental chamber for the post-mold curing at 175 °C for 6 hours to complete the polymerization process of the EMC.

In order to get the interfacial fracture toughness of the bi-material samples, a highly precise testing device is required. A computer-controlled Instron 5848 micro-tester was used for this purpose.

5.2.2 Four-Point Bending Delamination Tests

The critical forces, which were obtained from the 4PB experiments, were used to obtain the critical ERRs G_c (i.e. interfacial fracture toughness) of the interface between Cu leadframe and EMC. They were determined by the FEM simulations using the three mentioned methods: VCCT, VCE and J-integral. The verification of simulations was performed using an analytical solution (eq. (5.6)). Based on the critical ERRs obtained from different specimens tested at different temperatures, the temperature dependence of the interfacial fracture toughness was investigated.

The upper EMC layer of the sample was notched with a diamond blade to get the depth of the notch, approximately 80% of the EMC thickness. Fig. 5.1 shows the 4PB test setup, and Fig. 5.2 shows the sample before and after the test. The distance between the two loading pins was fixed at c = 20 mm, and the distance between the two supports was fixed at 2c = 40 mm. Noted that the 4PB delamination test can be performed in one, or two steps, including pre-cracking. Here, the single step approach was used, in which the whole fracture test is performed in a single step, without pre-cracking. In (Shirangi et al. 2008), it was shown that the critical forces are almost the same either with, or without pre-cracking.

Samples were loaded monotonically under displacement-controlled rate of 1 mm/min at room temperature. Fig. 5.3 shows a typical load-displacement curve of the 4PB fracture test. The slope of the linear part of the curve corresponds to the stiffness of the whole structure. The peak force represents the required force for fracture of the upper layer (EMC) through the notch, and does not provide any information about the interface fracture toughness. The vertical part of the curve shows that the notch has been broken down, and the interface has been reached. Afterwards, the crack advanced along the interface. This constant force during crack propagation

represents the critical force required to propagate the crack. Its constant value suggests that the critical ERR using 4PB fracture test does not depend on the crack length.

5.2.3 Four-Point Bending End-Notched Flexure Tests

In order to propose a comprehensive methodology for interfacial fracture toughness characterization, this section focuses on the mode II fracture. Since the interfacial fracture toughness is strongly mode-dependent, the 4ENF test was used instead of the 4PB. Another reason of choosing 4ENF test is that in comparison with the conventional three-point bending end-notched flexure test, the 4ENF test has a more stable crack growth, making it, in this work, a better tool to analyze the effects of moisture on the interfacial fracture toughness of bi-materials.

Fig. 5.4 shows the test set-up of the 4ENF for the determination of the resistance to delamination (critical ERR, or interfacial fracture toughness). Similar to the 4PB, LEFM was assumed to hold true for the 4ENF with the loading rate of 1 mm/min. The same samples were used, but after molding, they were kept for 6 hours in the heat chamber at 175 °C to complete the EMC polymerization process. Moreover, instead of notching the upper layer (EMC), in the 4ENF samples, the pre-crack at the interface was made by a sharp steel blade. The testing machine was Instron 5848 micro-tester. The distance between the two loading pins was fixed at 40 mm, and the distance between the two supports was fixed at 20 mm. Samples were loaded monotonically under displacement-controlled rate of 1 mm/min at room temperature.

Fig. 5.5 shows the force – displacement curve of the 4ENF test. The slope of the linear part of the curve (A-B) corresponds to the stiffness of the whole structure. The force at point B represents the required force (critical force) for the interfacial delamination. This force was used to determine the interfacial fracture toughness, G_c, in the simulation. From point B to C the crack

propagates, until it stops at point C. Afterwards, the load increases linearly again, and the slope represents the stiffness of the EMC only.

5.3 Finite Element Simulations

In this study, three FEM-based methods were implemented with the commercial general purpose FE software package, Ansys, to calculate ERRs of fractures. The three methods include VCCT (the main focus), VCE, and the J-integral. A major issue in fracture mechanics simulations is the large degree of freedom of the FE model. It is well known that a three dimensional FE model becomes very computationally expensive to implement, even with the minimal number of elements across the thicknesses, which in turn causes a very large aspect ratio in the simulation model. This chapter presents an effort to develop a simpler, low-cost two dimensional model to evaluate the system. With the test conformation, the problem can be assumed to be plane strain. The very good agreement between FE analysis results and the analytical solution confirmed this assumption (discussed in section 5.4, Fig. 5.9).

In order to get the most accurate result of the ERRs, the convergence analysis was used to find the optimal mesh. Fig. 5.6 shows the mesh-convergence analysis on three meshing parameters including the radius of first row elements at the crack tip, the number of elements in circumferential direction and the defined maximum element size.

5.3.1 Four-Point Bending Delamination Simulations

The critical forces, which were achieved from the 4PB experiments, were used to obtain the critical ERRs G_c (i.e. interfacial fracture toughness) of the interface between Cu leadframe and EMC. They were determined by the FEM simulations using the three mentioned methods: VCCT, VCE and J-integral. The verification of simulations was performed using an analytical solution (eq. (5.1)). In order to find the most accurate result for G_c, the convergence analysis was

used to find the optimal mesh. Based on the critical ERRs obtained from different specimens tested at different temperatures, the temperature dependence of the interfacial fracture toughness was investigated.

The simulation model of the test is shown in Fig. 5.7 (equivalent stress distribution in deformed shape of the 4PB model with optimal mesh, using singularity elements at the crack tip). Taking advantage of the symmetry, only half of the 4PB specimen is modelled. To prevent rigid body translation, the x-displacement of the points, where the two loads *P/2* are applied, is fixed. The analysis was performed in plane strain. The optimal mesh was obtained by performing the convergence analysis. The two types of meshing – using singularity elements at the crack tip and using mesh refinement around the crack tip, were implemented. There was not much difference between the two mesh types with respect to the obtained G_c values. Moreover, the computational time in the latter type is three times longer than the first one. Therefore, the former type was chosen. The mechanical properties of the bi-material, obtained by uniaxial tensile tests, are: E = 135 GPa and v = 0.34 for Cu leadframe, and E = 30 GPa and v = 0.24 for EMC at room temperature.

5.3.2 Four-Point Bending End-Notched Flexure Simulations

In order to find the most accurate result of the ERR, the convergence analysis was also used to find the optimal mesh in the same manner as for the 4PB specimens. The VCCT was applied to obtain the critical ERR for the 4ENF specimens, since it can give the ERR for each individual fracture mode. In this simulation, contact elements and target elements are required at the pre-crack surface to prevent elements penetration. Besides, the geometry non-linearity was also considered to obtain a better result. As mentioned in the 4PB case, two types of meshing, which are using singularity elements at the crack tip and using mesh refinement around the crack

tip, were used, and the former type was proven to be better. The simulation model of the test is shown in Fig. 5.8.

5.4 Results and Discussion

5.4.1 Interfacial Fracture Toughness of the Four-Point Bending Specimen

The ERR of 4PB delamination test exhibits steady-state characteristics when the interfacial crack reaches a minimum length, and does not exceed the distance between the inner supports (in this case, c = 20 mm). This value of G_c, is the difference between the strain energy in the un-cracked and cracked beams. Applying the beam theory and assuming LEFM, G can be calculated as in (Charalambides et al. 1989):

$$G = \frac{M^2(1-\nu_{\mathrm{Cu}}^2)}{2E_{\mathrm{Cu}}}\left(\frac{1}{I_{\mathrm{Cu}}} - \frac{\lambda}{I_c}\right), \tag{5.1}$$

where $\lambda = [E_{\mathrm{Cu}}(1-\nu_{\mathrm{EMC}}^2)]/[E_{\mathrm{EMC}}(1-\nu_{\mathrm{Cu}}^2)]$, $M = PL/2b$. I_c and I_{Cu} are the moments of inertia of the composite beam and Cu, respectively, which can be calculated as:

$$I_c = \frac{t_{\mathrm{EMC}}^3}{12} + \frac{\lambda t_{\mathrm{Cu}}^3}{12} + \frac{\lambda t_{\mathrm{EMC}} t_{\mathrm{Cu}}(t_{EMC}+t_{\mathrm{Cu}})^2}{4(t_{\mathrm{EMC}}+\lambda t_{\mathrm{Cu}})}, \text{ and } I_{\mathrm{Cu}} = \frac{t_{\mathrm{Cu}}^3}{12}.$$

In equation (5.1), the initial cracks are symmetric, and both cracks propagate simultaneously at the same load. The equation provides the interfacial fracture toughness, G_c, when the load, P, is substituted with the critical fracture load, P_c.

Fig. 5.9 shows the results of G (J/m^2) calculated by the four methods: VCCT, VCE, J-integral, and the analytical solution of equation (5.1), under the average critical load P_c (average of 5 tests) of 5.56 N (25 °C test temperature, 1 mm/min loading rate). These ERRs are at the average mode-mixity (see section 5.4.5) of 15.46°. It can be seen that G_c values calculated with the four methods are nearly the same. With a very good agreement with the other methods, and with the capability of finding the components of G, corresponding to the mode I and mode II

separately (thus the capability of finding the mode-mixity), VCCT was chosen as the main method and the others were used for reference.

Note that in this problem, the LEFM was assumed to hold true. First, the reaction forces and applied displacement, up to the delamination point, were always linear. Second, in Fig. 5.2, plastic deformation could be expected after the crack started to propagate. However, there is no significant plastic deformation at the moment. In other words, the plastic zone was much smaller than the SIF dominated field. (Volinsky et al. 1998) proposed the relationship between the ERR and the plastic zone size as the following:

$$G \approx c\frac{\sigma_{ys}^2}{E}\left(ln\left[\frac{c}{b}\right] - 1\right), \tag{5.2}$$

where c is the plastic zone size, b is Burgers vector, E is the Young's modulus, σ_{ys} is the yield stress of, in this case, the Cu layer. With the value of G = 17.78 J/m^2 (25 °C test temperature, 1 mm/min loading rate, Fig. 5.9), the plastic zone size was estimated as 5.52*10^{-3} mm which is much smaller than the Cu layer thickness of 0.25 mm. Last, the 4PB tests were performed at a relatively high displacement rate of 1 mm/min, and crack propagation happened within a couple of seconds after starting the test, and took normally less than one second until the crack reached the supports. Therefore, the visco-elastic effects due to the stress relaxation within such short crack propagation time were found to be almost negligible. The above reasons mean that the LEFM can be applied for these tests and the visco-elastic deformation of the EMC layer can be neglected.

5.4.2 Temperature Effects on the Interfacial Fracture Toughness

Temperature dependence of the interfacial fracture toughness of the Cu leadframe/EMC interface was investigated. After keeping all the 4PB samples for 6 hours in a heat chamber at 175 °C to complete the polymerization process of the EMC, they were tested at various

temperatures of 25 °C, 85 °C, 130 °C, 175 °C, 210 °C, and 250 °C (5 samples for each test temperature). The samples were loaded monotonically under displacement-controlled rate of 1 mm/min. Since the Young's modulus of EMC is temperature dependent, it was determined using uniaxial tensile tests at various temperatures (Table 5.3), identical to the fracture experiments temperature.

When testing at elevated temperatures and time scales, where visco-elastic deformation may affect the interfacial fracture toughness, LEFM is believed to be still valid, since the load-displacement curves are all linear, up to the point of delamination propagation. In this case, any significant visco-elastic deformation that may occur in a sample is assumed to occur on a very local scale at the crack tip region as a part of the crack growth process. Moreover, the EMC used in this work is cross-linked, which means, according to (Swallowe 1999), that the viscoelasticity effects can be neglected.

Fig. 5.10 shows the fracture toughness of the Cu leadframe/EMC interface, which was calculated by VCCT, as a function of the testing temperature. The results from 5 samples, along with the average value at each temperature, are shown (17.78 J/m^2 at 25 °C, 23.99 J/m^2 at 85 °C, 27.8 J/m^2 at 130 °C, 7.21 J/m^2 at 175 °C, 5.02 J/m^2 at 210 °C, and 4.71 J/m^2 at 250 °C). G_c was also calculated by using other approaches (i.e. VCE, J-integral and analytical formula) for comparison, and all of them give nearly the same values.

It can be seen that after an initial increase at the early stages of the temperature rise, the interfacial fracture toughness significantly decreases with the test temperature. The glass transition temperature of the EMC is about 130 °C. Therefore, the interfacial fracture toughness undergoes a significant change around the glass transition temperature.

5.4.3 Interfacial Fracture Toughness of the Four-Point Bending End-Notched Flexure Specimen

Until now, to the best of my knowledge, there is no acceptable analytical formula for the *G* calculation of 4ENF specimens, made of two different materials. Instead, there is only the formula for calculating the G_{II} (*G* at mode II), which can be found elsewhere (Davies et al. 2005; Shindo et al. 2008); and there is no formula for the mode I portion of the *G*. In the Fig. 5.13, it also can be seen that the 4ENF is close to the mode II facture, but actually it is at the mix-mode fracture. For that reason, the interfacial fracture toughness for the 4ENF delamination tests needs to be obtained through numerical computation using FE-based techniques. Components of the critical ERR, G_{Ic}, G_{IIc}, and the total critical ERR, G_c, were obtained by VCCT, based on the pre-crack lengths and the critical forces from 5 tests. Under the average critical load, P_c, of 229.9 N and the average pre-crack length of 11.72 mm, G_{Ic}, G_{IIc} and G_c of 3.64 J/m^2, 196.31 J/m^2 and 198.16 J/m^2, were obtained, respectively. This ERR value corresponds with the average mode-mixity angle of 82.27° (Fig. 5.13).

5.4.4 Moisture Effects on the Interfacial Fracture Toughness

The effect of moisture on the interfacial fracture toughness of Cu leadframe/EMC was investigated. All the fracture tests were performed at room temperature and the load rate of 1 mm/min. Before the tests, except for the samples tested in dry condition, all the other ones were placed into a moisture chamber for one week, 2 weeks, 3 weeks, 4 weeks and 5 weeks (5 samples for each category) at 85 °C and 85% relative humidity. Only the EMC layer absorbs moisture. An electronic balance scale was used for weighing the samples to calculate the amount of moisture absorbed by the EMC layer. The weight gain of the samples at the time of testing can be determined as:

$$\text{weight gain (\%)} = \frac{M_t - M_0}{M_0} \times 100\%, \tag{5.3}$$

where M_t is the weight of the sample at time t (in weeks) and M_0 is the dry weight before the moisture preconditioning. Fig. 5.11 shows the average mass of the moisture absorbed with respect to time. It can be recognized that the moisture absorption reached saturation at around 4 weeks at the weight gain of 0.22%.

From Fig. 5.12, which shows the critical ERRs of the moisture preconditioned samples, calculated by VCCT, based on experimental critical forces, the effect of moisture diffusion in humid chamber on the interfacial fracture toughness of bi-materials Cu leadframe/EMC can be seen. The initial interfacial fracture toughness of 198.16 J/m^2 in dry condition reduced significantly to 137.1 J/m^2 after one week of moisture absorption, and then continued to decrease slightly with moisture exposure time. Finally, the interfacial fracture toughness hardly changed when the moisture absorption of the specimens was around 20% (108.89 J/m^2 at 3 weeks, 106.59 J/m^2 at 4 weeks, 107.53 J/m^2 at 5 weeks and 100.43 J/m^2 at 6 weeks).

The effect of moisture on the interfacial fracture toughness is strong enough to put it into consideration when the device is exposed to humid environment in service. However, once exposed, the moisture effect is minimal after a certain time of around three weeks at 85 °C and 85% relative humidity. Interfacial fracture toughness decreases by a factor of two in 6 weeks of moisture exposure, compared to the dry conditions.

5.4.5 Mode-Mixity Effects on the Interfacial Fracture Toughness

The effect of mode-mixity ψ (also called mode angle, or phase angle), which is defined as $\tan^2 \psi = \frac{G_{II}}{G_I}$, on the interfacial fracture toughness has been widely investigated. For example, Liechti et al. (1991) proposed a method to find the range of in-plane fracture mode-mixity and

contact zone that can be obtained from bi-material samples. In that work, the crack opening displacement was measured and the values obtained with FE solutions were matched to get the mixed mode fracture parameters. Agrawal et al. (2006) have shown a method to obtain mode-mixity for a bimaterial interface crack using VCCT with the 4PB model. This section extends the work by using 4PB tests together with 4ENF tests to characterize the effect of mode-mixity on the interfacial fracture toughness of Cu leadframe/EMC.

It should be noted that when using the VCCT method to determine the components of the ERR, the virtual extension of the crack is determined by the length of the elements around the crack tip. In order to use the VCCT method correctly, it is required that the length of all elements across the interface at the crack tip are equal. However, a prominent problem of bi-material interface cracks is that: when the length of these elements in the FE meshing is changed, then the values of G components, G_I, G_{II} and G_{III}, also change, although the total G remains constant. This problem has been observed by many researchers (Agrawal et al. 2006; Agrawal et al. 2007; Oh 2004; Sun et al. 1997). This makes the calculation of the mode-mixity difficult, because it seems that the mode-mixity depends on the mesh size. Moreover, for a bimaterial interface crack, the solutions of the crack opening with oscillatory stress and displacement fields are reference length dependent and are given by the equations (5.4) and (5.5) by Rice (1988) and Hutchinson et al. (1991):

$$\sigma_{yy} + i\sigma_{xy} = \frac{K_I + iK_{II}}{\sqrt{2\pi r}} \left(\frac{r}{l}\right)^{i\varepsilon}, \tag{5.4}$$

$$\delta_y + i\delta_x = 8\frac{K_I + iK_{II}}{(1+2\varepsilon)E^* \cosh(\pi\varepsilon)\sqrt{2\pi r}} \sqrt{r} \left(\frac{r}{l}\right)^{i\varepsilon}, \tag{5.5}$$

where $\frac{1}{E^*} = \frac{1}{2}\left(\frac{1}{E_1} + \frac{1}{E_2}\right)$ and l is the reference length. A typical way of solving the above issues is that, for bimaterial interfaces, the mode-mixity is specified at a particular distance ahead of the

crack tip, which is normally referred as reference length or characteristic distance. Agrawal et al. (2006) showed that several, apparently different, methods suggested in literature for obtaining mode-mixity based on the SIFs are indeed identical. As suggested by Beuth (1996), a stable mode-mixity can be defined by introducing the reference length parameter. It should be noted that this reference length is only a mathematical quantity with no physical meaning and is only used to enable a consistent way of reporting the mode-mixity values. It must be also noted that this problem is dependent on many factors, such as geometry of the model, element types, and more importantly, mismatch in the mechanical properties of the two dissimilar materials. Moreover, the variation in the mode-mixity is not a major problem due to the relatively moderate β values (where β is a mechanical properties parameter proposed by Rice (1988)). Therefore, it can be concluded that if the element size is small enough to get a convergence of the total G value, the shift of the mode-mixity due to the element size is almost equal for all problems provided that the same element size is used. In other words, the results from VCCT are consistent, even with an existing shift, whether positive or negative, in the calculated mode-mixity.

Fig. 5.13 shows the critical ERR G_c, calculated for the two test geometries (4PB and 4ENF) of the leadframe/EMC, as a function of the phase angle. From the 4PB delamination test at room temperature and the loading rate of 1 mm/min, a mean fracture toughness of 17.78 J/m^2 was obtained. The average interfacial fracture toughness found in the 4ENF test for the same conditions was much higher, at 198.16 J/m^2. This phenomenon can be explained by the mode-mixity angle. Interfacial fracture toughness strongly depends on the mode-mixity, as it increases with the contribution of the mode II fracture. In the 4PB delamination test, the average phase angle is 15.46° (with G_I = 16.52 J/m^2, G_{II} = 1.26 J/m^2 and G = 17.78 J/m^2), which means that the

fracture is close to the mode I. In the 4ENF test, the average phase angle is 82.27°, which means that the fracture is mostly mode II. In practice, the phase angle involves many delamination phenomena, among which loading is a significant impact factor (Evans et al. 1995; Gan et al. 2005; Högberg et al. 2006; Hutchinson et al. 1991). Let's take a look at the formula (2.16) in chapter 2, the phase angle depends on the components of the loading, which depends on the configuration of the test setup (e.g. the distance between the supports and that between the loading positions); and the chosen crack size, which is in this case the radius of 1st row elements at the crack tip.

Several relationships have been proposed to characterize interfacial fracture toughness as a function of the phase angle (Hutchinson et al. 1991). There are results in the literature, both experimental and theoretical, that exhibit similar behaviour, such as (Liechti et al. 1991) and (Jensen et al. 1993). The most realistic description of the functional dependence of the interfacial toughness on the mode-mixity was proposed by Hutchinson et al. (1991):

$$G_c = G_{c0}[1+\tan^2(\psi(1-\lambda))], \tag{5.6}$$

where G_{c0} is the mode I interfacial toughness with respect to ψ = 0 and λ is an adjustable parameter. By fitting the results of this work, the interfacial fracture toughness and the mode-mixity relationship for the bi-materials Cu lead-frame/EMC was achieved (Fig. 5.13). In this case G_{c0} = 16.78 J/m^2 and λ = 0.111, yielding the following G_c phase angle dependence:

$$G_c = 16.78[1+\tan^2(0.889\psi)]. \tag{5.7}$$

5.5 Conclusions

This chapter was to study the interface delamination propagation and then characterize the fracture toughness of the interface between Cu leadframe and EMC under monotonic loading by experimental data and numerical simulations. Fracture mechanics was used as a theory guide.

Within the framework, the energy approach was applied in which the ERR is the key parameter. Two dimensional simulations with the methods, such as VCCT, VCE and J-integral have been proven accurate and computationally cheap to find the ERRs and, together with critical force obtained by experiments (4PB and 4ENF tests), the interfacial fracture toughness of a bi-material structure was calculated.

This work shows a systematic investigation and characterization of the interfacial fracture toughness of the bi-material Cu leadframe/EMC, including the testing temperature dependence of the interfacial fracture toughness, the moisture diffusion effect on the fracture toughness and the relationship between the fracture toughness and the mode-mixity. First, after an initial increase at the early stages of the temperature rise, the interfacial fracture toughness significantly decreases with the test temperature. Because of the glass transition temperature of the EMC is about 130 °C, the interfacial fracture toughness suffers a significant change around this temperature. Second, the effect of moisture on the interfacial fracture toughness is strong enough to put it into consideration when the device is in service in a humid environment. However, the moisture effect is minimal after a certain time of around three weeks at 85 °C and 85% relative humidity and the interfacial fracture toughness decreases by a factor of two in 6 weeks of moisture exposure compared to the dry conditions. Last, by fitting, the interfacial fracture toughness and the mode-mixity relationship for the bimaterials Cu leadframe/EMC was achieved.

The results of this chapter can be generally applied to predict the delamination, as well as to characterize the interfacial fracture toughness between two layers of dissimilar materials under different environmental conditions.

5.6 Tables and Figures

Table 5.1 Composition of the EMC. Credit (Tran et al. 2014)

EMC components	Composition
Epoxy resin	Multi Aromatic + Biphenyl
Hardener	Low water absorption
Flame retardant system	No FR
Filler content	88 / 80 Weight / volume, %
Filler shape	All spherical (average 50 µm diameter)
Spiral flow	1143 mm
Gelation time (175 °C)	30 sec
Flexural Modulus	2450 kgf/mm^2
Flexural strength	15 kgf/mm^2

Table 5.2 Composition of the Cu leadframe. Credit (Tran et al. 2014)

Cu	Fe	P	Pb	Zn
Balance	2.1-2.6wt.%	0.015wt.%	0.03wt.%	0.05-0.2wt.%

Table 5.3 Young's modulus of EMC at varying temperature. Credit (Tran et al. 2014)

Temperature (°C)	Young's modulus of EMC (GPa)
25	30
85	25
130	2
175	2
210	1
250	1

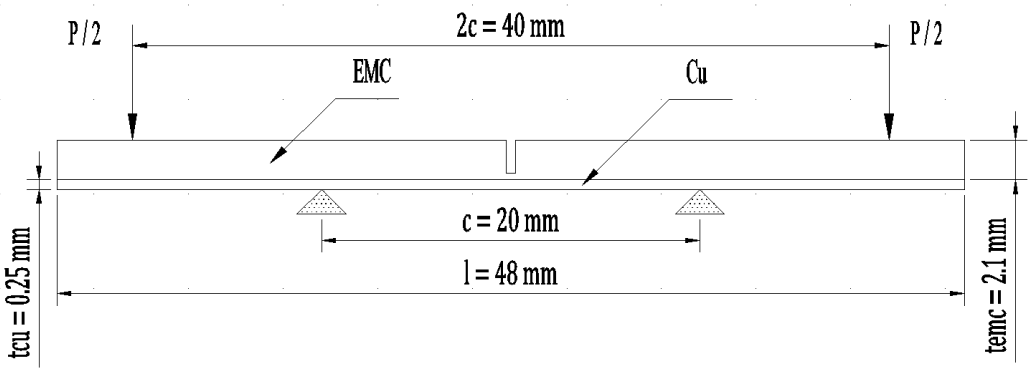

Figure 5.1 4PB delamination test set-up. Credit (Tran et al. 2014).

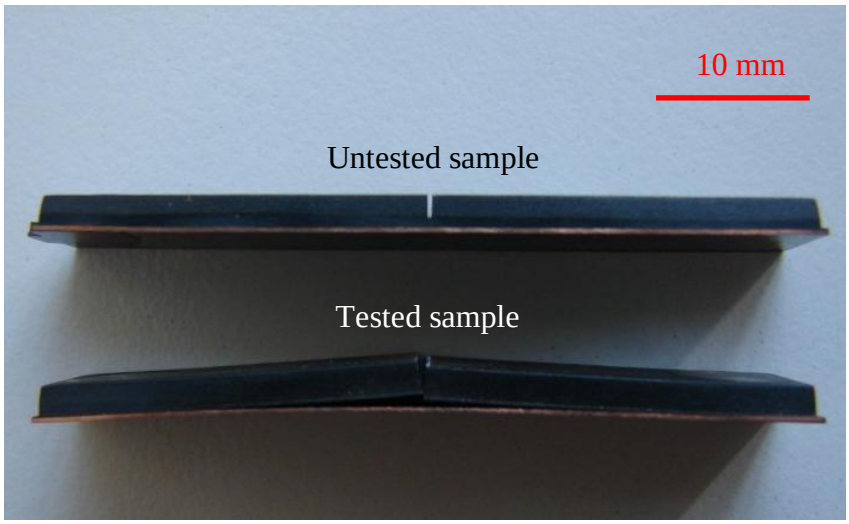

Figure 5.2 4PB delamination specimen before and after the test. Credit (Tran et al. 2014).

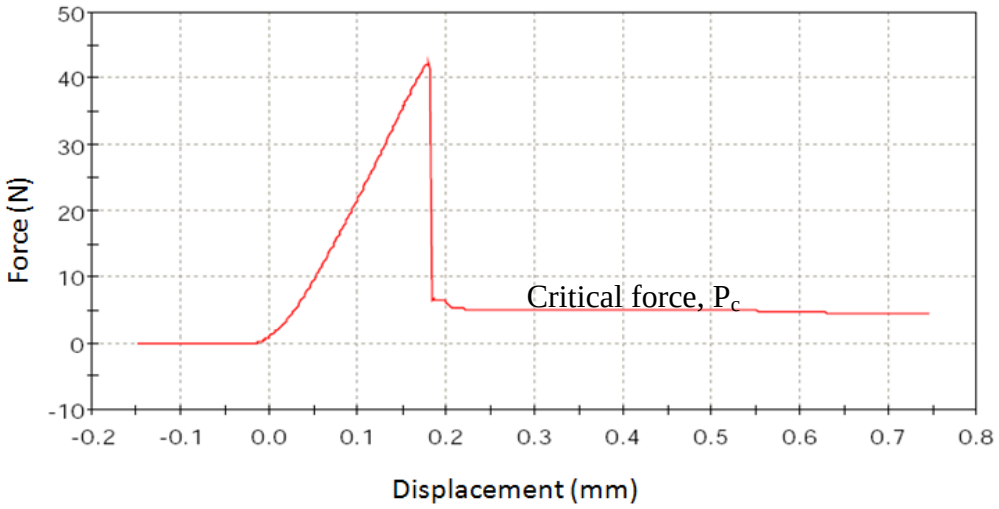

Figure 5.3 The force – displacement curve of a 4PB delamination test at room temperature. Credit (Tran et al. 2014).

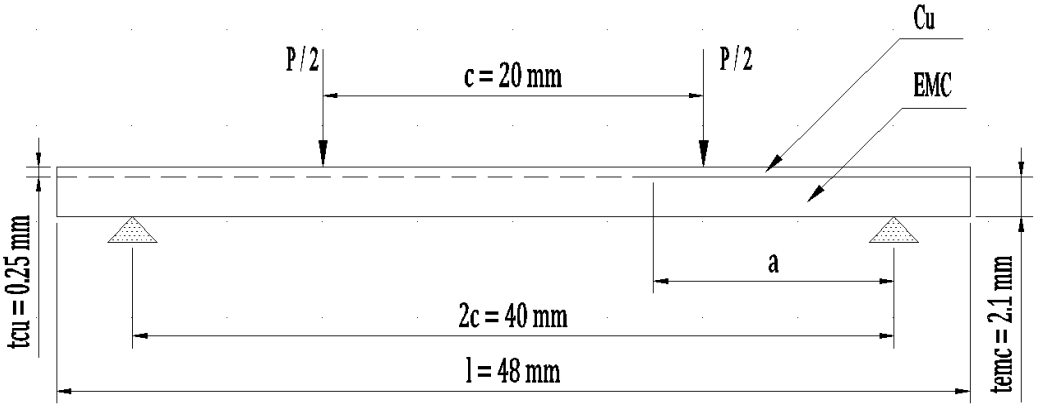

Figure 5.4 4ENF set-up. Credit (Tran et al. 2014).

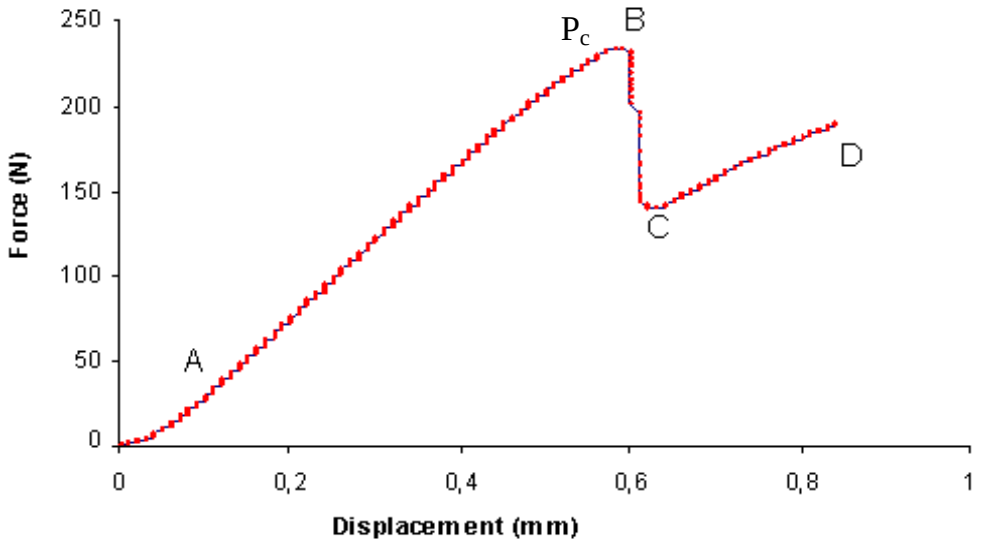

Figure 5.5 The force – displacement graph of the 4ENF delamination test at room temperature. Credit (Tran et al. 2014).

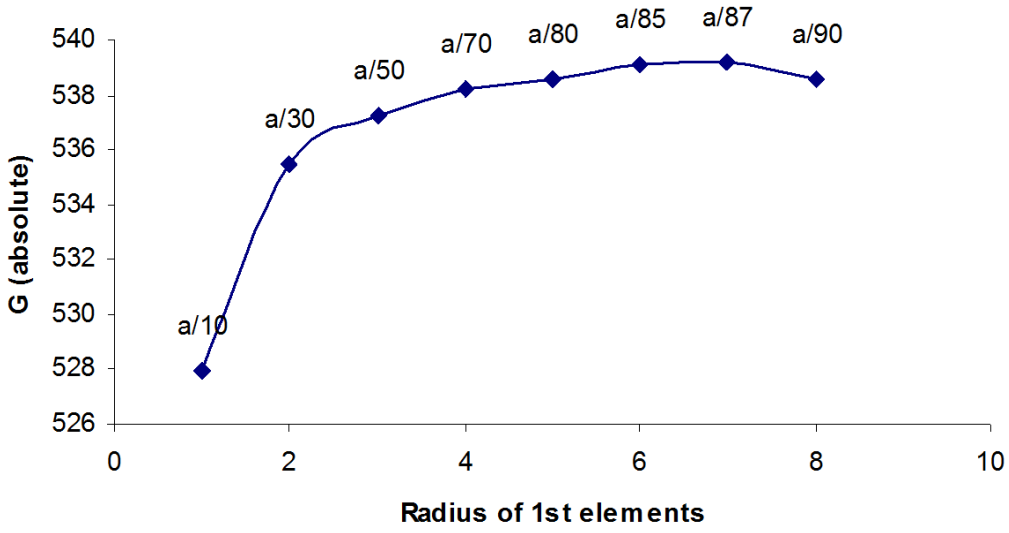

(a) Optimal parameter is a/85.

Figure 5.6 Mesh-convergence analysis on three meshing parameters including (a) the radius of first row elements at the crack tip, (b) the number of elements in circumferential direction and (c) the defined maximum element size. *a* is the crack length.

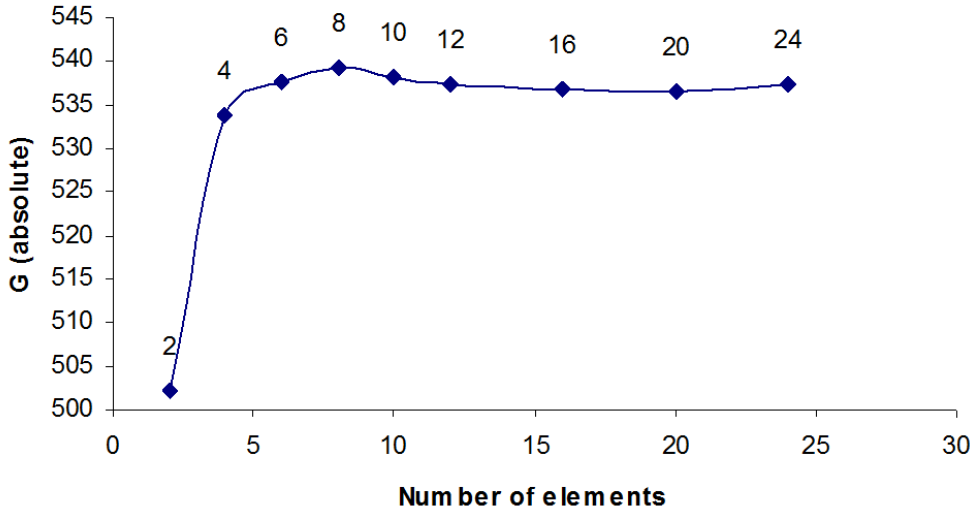

(b) Optimal parameter is 10.

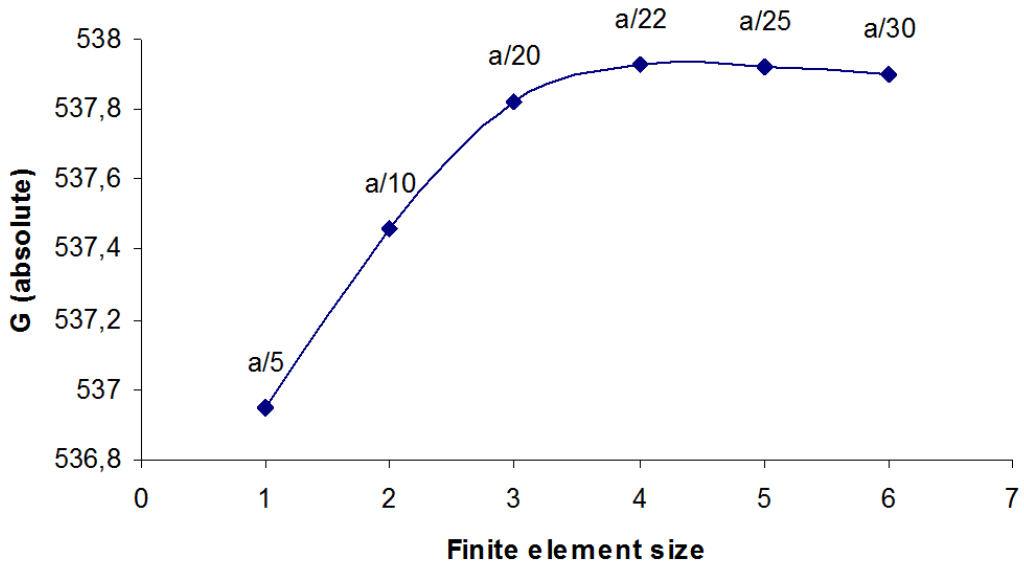

(c) Optimal parameter is a/22.

Figure 5.6 (continued).

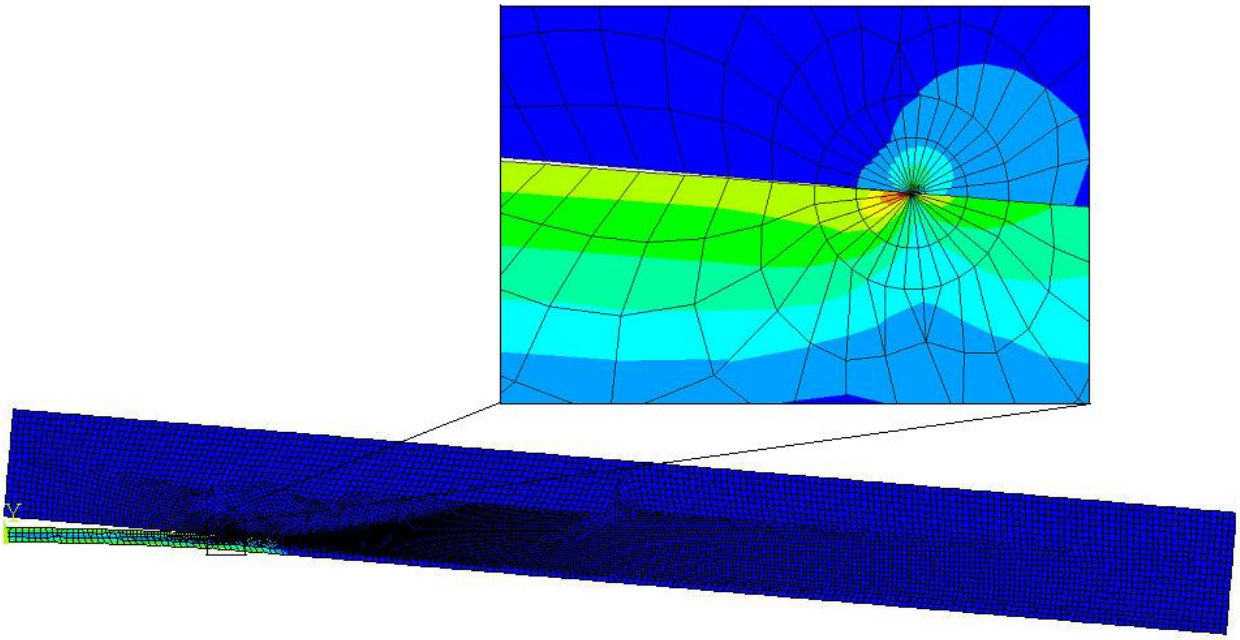

Figure 5.7 Equivalent stress distribution in deformed shape of the 4PB model with optimal mesh, using singularity elements at the crack tip. Credit (Tran et al. 2014).

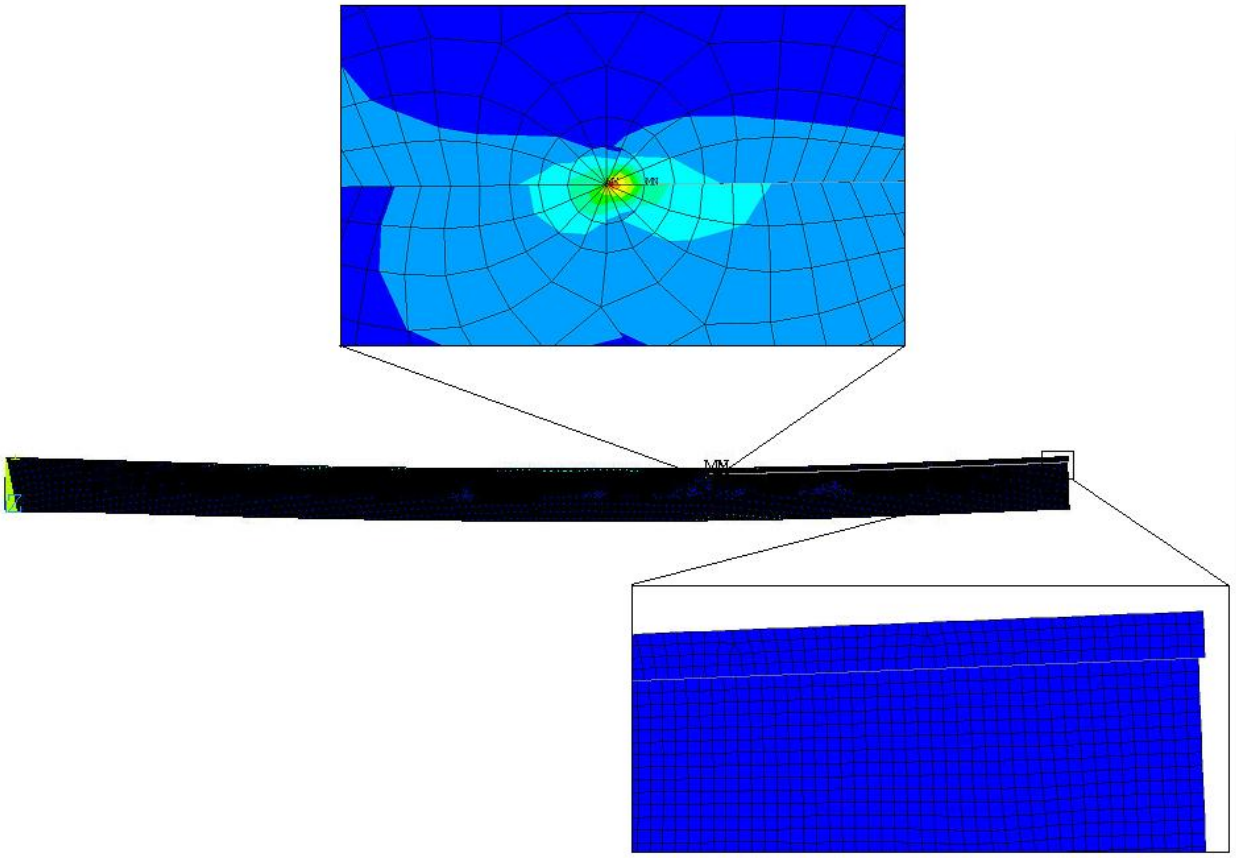

Figure 5.8 Deformation shape of the 4ENF model with optimal mesh using singularity elements at the crack tip. Credit (Tran et al. 2014).

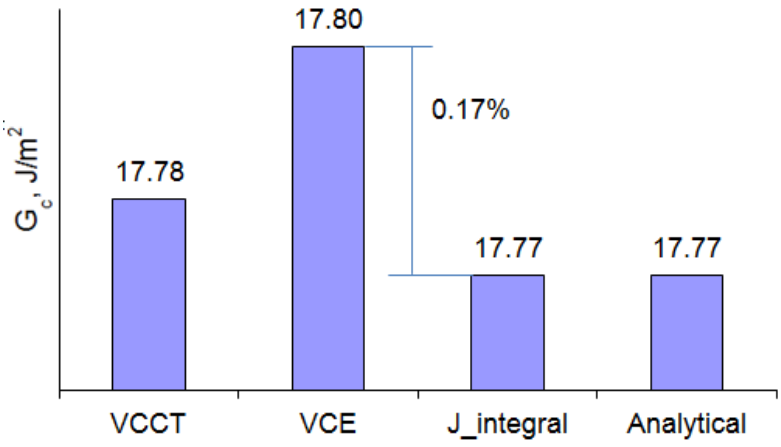

Figure 5.9 Critical ERRs calculated by the four methods. Credit (Tran et al. 2014).

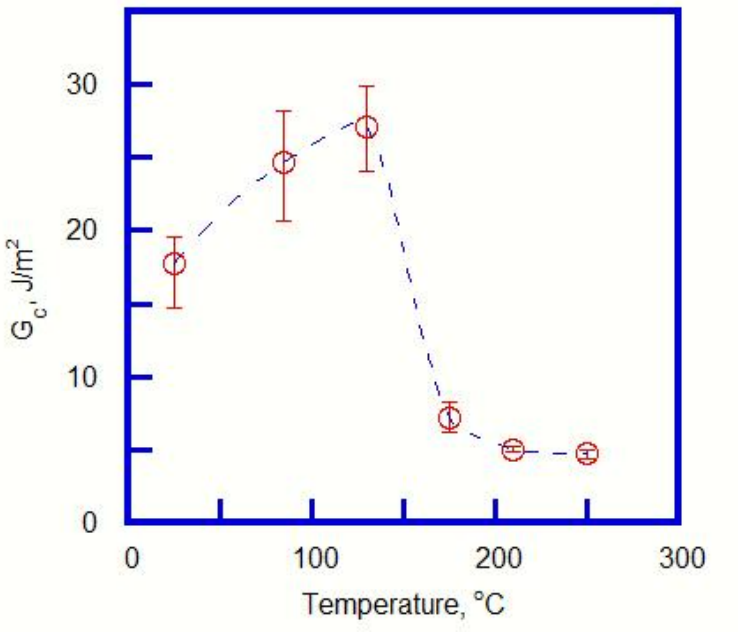

Figure 5.10 G_c calculated by VCCT using experimental critical force at different temperatures. Credit (Tran et al. 2014).

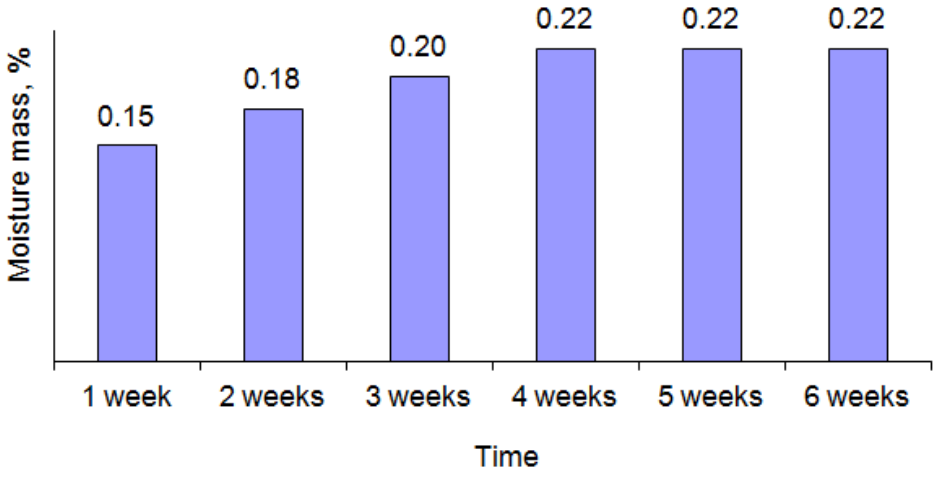

Figure 5.11 The average moisture mass absorbed by EMC. Credit (Tran et al. 2014).

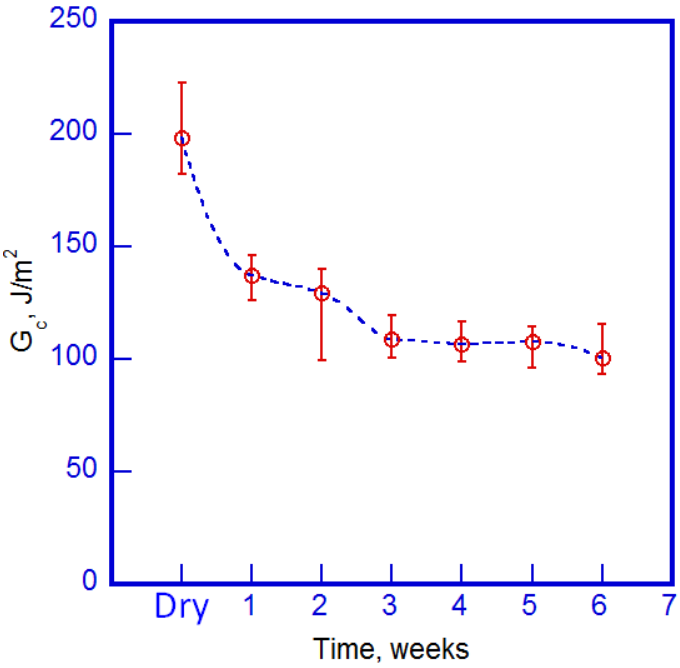

Figure 5.12 G_c calculated by VCCT using experimental critical forces of the moisture absorbed specimens. Credit (Tran et al. 2014).

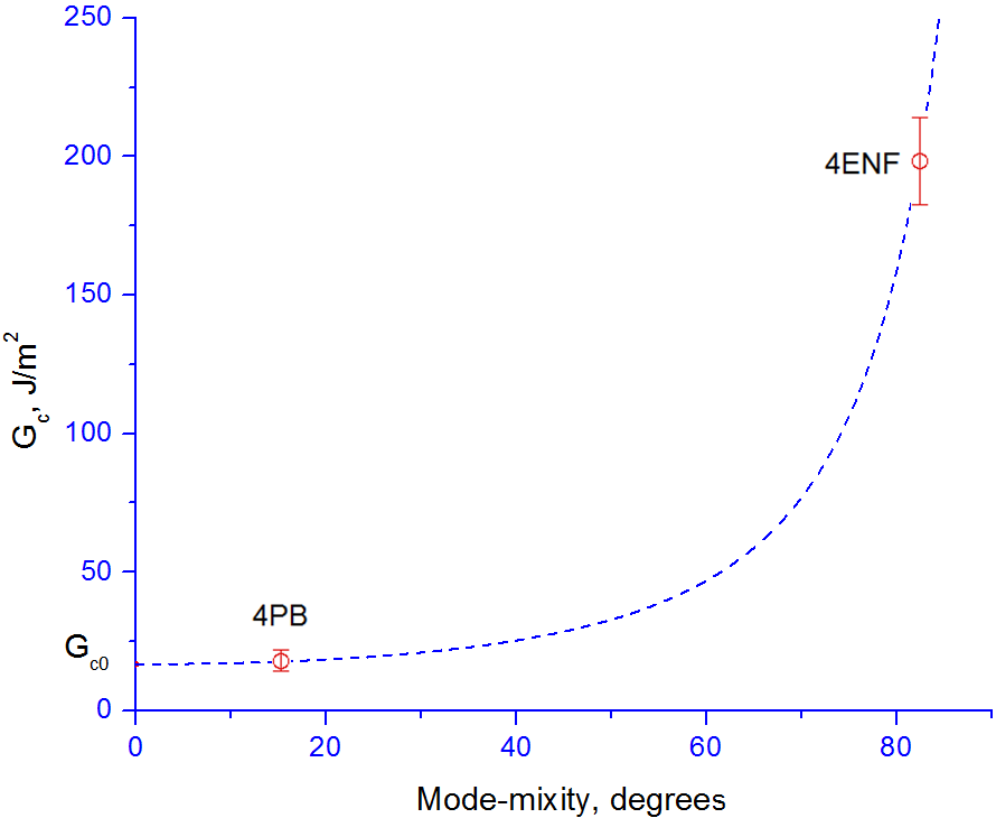

Figure 5.13 Interfacial fracture toughness as a function of the phase angle for the 4PB and 4ENF tests, along with the empirical fit of equation (5.7). Credit (Tran et al. 2014).

CHAPTER 6: CONCLUSIONS AND FUTURE WORK

6.1 Conclusions

6.1.1 Al-Mn Alloy Thin Films Coated on Polyimide Substrates Structures

Mechanical properties of monolithic and multilayered Al-Mn thin films coated on PI substrates were studied by tensile testing and FEA with the following conclusions.

a. Fracture Behavior of Monolithic Samples with Various Mn Concentrations

Among the monolithic films, the amorphous Al-Mn (Al-20.5 at.% Mn, sample M20) possesses the highest fracture toughness, but limited ductility compared to its crystalline counterparts (Al-5.2 at.% Mn and Al-11.5 at.% Mn).

b. Optimizing Ductility and Fracture Properties Using Multilayer Schemes

To improve the stretchability of the amorphous Al-Mn (Al-20.5 at.% Mn, sample M20) system without compromising the fracture toughness, bilayered and trilayered films were designed by adding Cu buffer layers to the system. It was found that the bilayered structure with 50 nm Cu buffer layer (Cu|Al-20.5 at.% Mn, sample B1) improves the ductility of amorphous Al-Mn by more than ten times while the trilayered structure (Cu|Al-20.5 at.% Mn|Cu, sample S) optimizes both ductility and fracture toughness. Analytical modeling and FEA show that in the trilayered structure, the topmost Cu layer retards crack initiation, while the inner Cu layer dissipates strain energy and improves film/PI adhesion. In this case, the elongation was enhanced more than ten times and the interfacial fracture toughness twenty four times with a limited sacrifice of fracture toughness (less than 18%).

c. Effects of the Buffer Layer Material Properties on the Interface Adhesion

The interface adhesion of the structure was improved by adding a buffer layer (Al or Cr with variety of thicknesses) in between and roughening the substrates. Among the flat substrate samples with a 20 nm buffer layer, the one with Al buffer layer (MAl20) has an interfacial adhesion of three times stronger than that with Cr (MCr20). It is postulated that in order to improve the interface adhesion of the system (without roughing the PI), a thin (e.g. 20 nm) ductile buffer layer (e.g. Al) of smaller yield strength (than the fracture strength of the amorphous film) should be added in between the film and the substrate.

d. Effects of the Substrate Roughness on the Interface Adhesion

Among the rough substrate samples, the interfacial adhesion of MCr20-R is nine times stronger than the flat one (MCr20). Moreover, in the comparison with other rough counterparts, i.e. M-R and MAl20-R, it is about 5 and 1.5 times stronger, respectively. Hence, it can be predicted that with the condition of the rough PI substrate, higher adhesion of an amorphous brittle film/PI interface can be obtained by having a 20 nm buffer layer with higher strength and stiffness (than the brittle film).

e. Effects of the Buffer Layer Thickness on the Interface Adhesion

When increasing the buffer layer thickness, while MAlx and MAlx-R (x = 20, 50, 75 and 100) samples show their independence on buffer layer thicknesses, the MCrx and MCrx-R samples reach their J-integral maximums at x = 75 nm. Particularly, MCr75-R improves the interface adhesion of the base sample M to almost 20 times and is therefore the most beneficial case. That is the result of the fact that the Cr buffer layer reaches its highest amount of strain energy dissipation ability at the thickness of 75 nm maximizing the ability of preserving the ductility and then delaying the final failure of the whole system.

6.1.2 Copper Leadframe/Epoxy Molding Compound Structures

The interface delamination propagation and the fracture toughness of the interface between Cu leadframe and EMC under monotonic loading were studied by experiments and numerical simulations. Moreover, a systematic investigation and characterization of the interfacial fracture toughness of the bi-material Cu leadframe/EMC, including the testing temperature dependence of the interfacial fracture toughness, the moisture diffusion effect on the fracture toughness and the relationship between the fracture toughness and the mode-mixity was carried out.

a. Computational Methods in Fracture Mechanics

Within the framework of fracture mechanics, the energy approach was applied in which the ERR is the key parameter. Two dimensional simulations with the methods, such as VCCT, VCE and J-integral have been proven accurate and computationally cheap to find the ERRs. Together with critical force obtained by experiments (4PB and 4ENF tests), the interfacial fracture toughness of the bimaterial structure was calculated.

b. Temperature effects on the interfacial fracture toughness

After an initial increase at the early stages of the temperature rise, the interfacial fracture toughness significantly decreases with the test temperature. Because of the glass transition temperature of the EMC is about 130 °C, the interfacial fracture toughness suffers a significant change around this temperature.

c. Moisture Effects on the Interfacial Fracture Toughness

The effect of moisture on the interfacial fracture toughness is strong enough to put it into consideration when the device is in service in a humid environment. However, the moisture effect is minimal after a certain time of around three weeks at 85 °C and 85% relative humidity and the interfacial fracture toughness decreases by a factor of two in 6 weeks of moisture exposure comparing to the dry conditions. The interfacial fracture toughness hardly changed when the system was exposed to moisture from 3 weeks and more.

d. Mode-mixity Effects on the Interfacial Fracture Toughness

By fitting the results with an analytical formula, the interfacial fracture toughness and the mode-mixity relationship for the bimaterial Cu leadframe/EMC was achieved.

The results of this chapter can be generally applied to predict the delamination, as well as to characterize the interfacial fracture toughness between two layers of dissimilar materials under different environmental conditions.

6.2 Future Work

In chapter 3, the bilayered and trilayered samples were buffered with Cu layers due to the relatively high ductility and tensile strength of Cu. Specifically, some studies have shown that if the strength of the well-adhered crystalline layer is similar or higher than that of the amorphous counterpart, the amorphous layer will be constrained by the crystalline one, making the whole multilayered film fail at a larger strain (Chen et al. 2011b; Li et al. 2007b; Nieh et al. 1999). This work can be extended to other buffer materials rather than Cu such as Cr, Fe, Ti or metallic alloys which show high strength and stiffness as well as good adhesion to the selected polymers.

To increase the interface adhesion of amorphous Al-Mn/PI, one of the strategies is roughening the PI substrate with 100 nm Ra. Because of the limited time, the effects of the PI

roughness were not investigated. This consideration can be done in such a way that the optimum roughness patterns with respect to the variation of buffer layer's mechanical properties can be systemized. Moreover, the results of chapter 4 is just simulation, therefore the author calls for further experimental studies to verify the predictions.

Regarding the Cu leadframe/EMC system, mode II fracture toughness should be studied in future to get better results. During the 4ENF tests, the effect of friction is significant, when Cu and EMC layers slide on each other. As a result, 4ENF tests normally over estimate the interfacial fracture toughness. However, due to the lack of data regarding friction coefficient, this factor was neglected when investigating the effects of moisture diffusion.

This study showed the effects of environmental factors such as testing temperature, moisture diffusion and mode-mixity on the interfacial fracture toughness. Nevertheless, the moisture condition was restricted to moisture sensitivity level 1 which is the worst case of reliability testing in electronics package engineering. Future work can consider different moisture sensitivity levels which widen the application of the study.

Moreover, the models can be applied to investigate other factors affecting the reliability of the electronics packaging systems such as thermal aging, loading rates and fatigue loading conditions. The results might fulfill the picture of the delamination in such system under variety environmental conditions.

REFERENCES

Agrawal A, Karlsson AM (2006). Obtaining mode mixity for a bimaterial interface crack using the virtual crack closure technique. International Journal of Fracture 141:75-98

Agrawal A, Karlsson AM (2007). On the Reference Length and Mode Mixity for a Bimaterial Interface. Journal of Engineering Materials and Technology 129:580-587

Alfano G, Crisfield MA (2001). Finite element interface models for the delamination analysis of laminated composites: mechanical and computational issues. International Journal for Numerical Methods in Engineering 50:1701-1736

Anderson PM, Li C (1993). Crack-Dislocation Modeling of Ductile-To-Brittle Transitions in Multilayered Materials. MRS Online Proceedings Library 308

Anderson TL (2005). Fracture mechanics: fundamentals and applications. CRC Press, Boca Raton, Florida, USA

Ansys (2016). Ansys 17 user's manual. Ansys Inc, Canonsburg, Pennsylvania, USA

Barenblatt GI (1962). The Mathematical Theory of Equilibrium Cracks in Brittle Fracture. Advances in Applied Mechanics 7:55-129

Beuth JL (1996). Separation of crack extension modes in orthotropic delamination models. International Journal of Fracture 77:305-321

Beuth Jr JL (1992). Cracking of thin bonded films in residual tension. International Journal of Solids and Structures 29:1657-1675

Bing P, Kemao Q, Huimin X, Anand A (2009). Two-dimensional digital image correlation for in-plane displacement and strain measurement: a review. Measurement Science and Technology 20

Bonderover E, Wagner S (2004). A woven inverter circuit for e-textile applications. Electron Device Letters, IEEE 25:295-297

Brabec CJ (2004). Organic photovoltaics: technology and market. Solar Energy Materials and Solar Cells 83:273-292

Camacho GT, Ortiz M (1996). Computational modelling of impact damage in brittle materials. International Journal of Solids and Structures 33:2899-2938

Camanho PP, Davila CG, Pinho ST (2004). Fracture analysis of composite co-cured structural joints using decohesion elements. Fatigue & Fracture of Engineering Materials & Structures 27:745-757

Cardarelli F (2008) Materials Handbook: A Concise Desktop Reference. London: Springer–Verlag

Chan EKL, Yuen MMF (2009). Study of Interfacial Moisture Diffusion at Epoxy/Cu Interface. Journal of Adhesion Science and Technology 23:1253-1269

Charalambides PG, Lund J, Evans AG, McMeeking RM (1989). A Test Specimen for Determining the Fracture Resistance of Bimaterial Interfaces. Journal of Applied Mechanics 56:77-82

Chen A, Li D, Zhang J, Song H, Lu J (2008). Make nanostructured metal exceptionally tough by introducing non-localized fracture behaviors. Scripta Materialia 59:579-582
Chen AY, Ruan HH, Zhang JB, Liu XR, Lu J (2011a). Introducing a hierarchical structure for fabrication of a high performance steel. Materials Chemistry and Physics 129:1096-1103
Chen W, Chan KC, Guo SF, Yu P (2011b). Plasticity improvement of an Fe-based bulk metallic glass by geometric confinement. Materials Letters 65:1172-1175
Cherepanov GP (1979). Mechanics of Brittle Fracture. McGraw Hill New York
Chu CW, Jang JSC, Chiu SM, Chu JP (2009). Study of the characteristics and corrosion behavior for the Zr-based metallic glass thin film fabricated by pulse magnetron sputtering process. Thin Solid Films 517:4930-4933
Chu JP, Huang JC, Jang JSC, Wang YC, Liaw PK (2010). Thin film metallic glasses: Preparations, properties, and applications. JOM 62:19-24
Cordill MJ, Taylor A, Schalko J, Dehm G (2010). Fracture and Delamination of Chromium Thin Films on Polymer Substrates. Metallurgical and Materials Transactions A 41A:870-875
Cotterell B (2002). The past, present, and future of fracture mechanics. Engineering Fracture Mechanics 69:533-553
Cox BN, Marshall DB (1991). The determination of crack bridging forces. International Journal of Fracture 49:159-176
Dauskardt RH, Lane M, Ma Q, Krishna N (1998). Adhesion and debonding of multi-layer thin film structures. Engineering Fracture Mechanics 61:141-162
Davies P, Casari P, Carlsson LA (2005). Influence of fibre volume fraction on mode II interlaminar fracture toughness of glass/epoxy using the 4ENF specimen. Composites Science and Technology 65:295-300
Dugdale DS (1960). Yielding of steel sheets containing slits. Journal of the Mechanics and Physics of Solids 8:100-104
Dupont (2004). Physical and Thermal Properties of Kapton® polyimide films. Available from: http://wwwdupontcom/content/dam/assets/products-and-services/membranes-films/assets/DEC-Kapton-summary-of-properties.pdf
Eberl C (2010) Digital Image Correlation and Tracking. Matlab center. https://www.mathworks.com/matlabcentral/profile/authors/502139-christoph-eberl.
Erdogan F (2000). Fracture mechanics. International Journal of Solids and Structures 37:171-183
Espinosa HD, Zavattieri PD (2003). A grain level model for the study of failure initiation and evolution in polycrystalline brittle materials. Part I: Theory and numerical implementation. Mechanics of Materials 35:333-364
Evans AG, Hutchinson JW (1989). Effects of non-planarity on the mixed mode fracture resistance of bimaterial interfaces. Acta Metallurgica 37:909-916
Evans AG, Hutchinson JW (1995). The thermomechanical integrity of thin films and multilayers. Acta Metallurgica et Materialia 43:2507-2530
Evans AG, Rühle M, Dalgleish BJ, Charalambides PG (1990). The fracture energy of bimaterial interfaces. Materials Science and Engineering: A 126:53-64
Fan HB, Chung PWK, Yuen MMF, Chan PCH (2005). An energy-based failure criterion for delamination initiation in electronic packaging. Journal of Adhesion Science and Technology 19:1375-1386
Fan XJ, Wang HB, Lim TB Investigation of the underfill delamination and cracking in flip-chip modules under temperature cyclic loading. Electronic Components and Technology Conference 49th, 1999. pp 994-1000

Fors F (2010) Analysis of Metal to Composite Adhesive Joints in Space Applications, Ph.D Thesis. Linköping University, Sweden
Fosdick R, Truskinovsky L (2003). About Clapeyron's Theorem in Linear Elasticity. Journal of Elasticity 72:145-172
Frank S, Gruber PA, Handge UA, Spolenak R (2011). In situ studies on the cohesive properties of alpha- and beta-Ta layers on polyimide substrates. Acta Materialia 59:5881-5892
Frank S, Handge UA, Olliges S, Spolenak R (2009). The relationship between thin film fragmentation and buckle formation: Synchrotron-based in situ studies and two-dimensional stress analysis. Acta Materialia 57:1442-1453
Freund L, Suresh S (2003) Thin Film Materials: Stress, Defect Formation, and Surface Evolution. Cambridge University Press,
Gan Z, Mhaisalkar SG, Chen Z, Zhang S, Chen Z, Prasad K (2005). Study of interfacial adhesion energy of multilayered ULSI thin film structures using four-point bending test. Surface and Coatings Technology 198:85-89
George M, Coupeau C, Colin J, Grilhe J (2005). Mechanical behaviour of metallic thin films on polymeric substrates and the effect of ion beam assistance on crack propagation. Acta Materialia 53:411-417
Haodan J (2010) Cohesive Zone Model for Carbon Nanotube Adhesive Simulation and Fracture-Fatigue Crack Growth. University of Akron
Harries RJ, Sitaraman SK (1999). Numerical study of copper-encapsulant interfacial delamination propagation in a peripheral array package. Proceeding Advanced Electronics Packaging 2:1755–1762
He MY, Heredia FE, Wissuchek DJ, Shaw MC, Evans AG (1993). The mechanics of crack growth in layered materials. Acta Metallurgica et Materialia 41:1223-1228
Hofmann DC, Suh J-Y, Wiest A, Duan G, Lind M-L, Demetriou MD, Johnson WL (2008). Designing metallic glass matrix composites with high toughness and tensile ductility. Nature 451:1085-1089
Högberg JL, Stigh U (2006). Specimen proposals for mixed mode testing of adhesive layer. Engineering Fracture Mechanics 73:2541-2556
Horsley DJ (2003). Background to the use of CTOA for prediction of dynamic ductile fracture arrest in pipelines. Engineering Fracture Mechanics 70:547-552
Hsia KJ, Suo Z, Yang W (1994). Cleavage due to dislocation confinement in layered materials. J Mech Phys Solids 42:877-896
Hu KX, Yeh CP, Wu XS, Wyatt K (1996). An Interfacial Delamination Analysis for Multichip Module Thin Film Interconnects. Journal of Electronic Packaging 118:206-213
Huang R, Prévost JH, Huang ZY, Suo Z (2003). Channel-cracking of thin films with the extended finite element method. Engineering Fracture Mechanics 70:2513-2526
Hutchinson JW, Suo Z (1991) Mixed Mode Cracking in Layered Materials. In: John WH, Theodore YW (eds) Advances in Applied Mechanics, vol Volume 29. Elsevier, pp 63-191
Inoue A (2001). Bulk amorphous and nanocrystalline alloys with high functional properties. Materials Science and Engineering: A 304–306:1-10
Inoue A, Shen B, Koshiba H, Kato H, Yavari AR (2003). Cobalt-based bulk glassy alloy with ultrahigh strength and soft magnetic properties. Nature Materials 2:661-663
Irwin GR (1957). Analysis of stresses and strains near the end of a crack traversing a plate. Journal of Applied Mechanics 24:361–364

Jensen HM, Thouless MD (1993). Effects of residual stresses in the blister test. International Journal of Solids and Structures 30:779-795
Kamer A, Larson-Smith K, Pingree LSC, Dauskardt RH (2011). Adhesion and degradation of hard coatings on poly (methyl methacrylate) substrates. Thin Solid Films 519:1907-1913
Kim SH, Cho SH, Lee NE, Kim HM, Nam YW, Kim Y-H (2005a). Adhesion properties of Cu/Cr films on polyimide substrate treated by dielectric barrier discharge plasma. Surface and Coatings Technology 193:101-106
Kim SH, Na SW, Lee NE, Nam YW, Kim Y-H (2005b). Effect of surface roughness on the adhesion properties of Cu/Cr films on polyimide substrate treated by inductively coupled oxygen plasma. Surface and Coatings Technology 200:2072-2079
Komori S, Sakamoto Y (2009) Development Trend of Epoxy Molding Compound for Encapsulating Semiconductor Chips. In: Lu D, Wong CP (eds) Materials for Advanced Packaging. Springer US, Boston, MA, pp 339-363
Kou H, Lu J, Li Y (2014). High-Strength and High-Ductility Nanostructured and Amorphous Metallic Materials. Advanced Materials 26:5518-5524
Krueger R (2004). Virtual crack closure technique: History, approach, and applications. Applied Mechanics Reviews 57:109-143
Kuan SY, Chou HS, Huang JC (2013). Mechanical characteristics of Mg–Cu–Zr thin film metallic glasses. Surface and Coatings Technology 231:58-61
Li S, Thouless MD, Waas AM, Schroeder JA, Zavattieri PD (2005a). Use of a cohesive-zone model to analyze the fracture of a fiber-reinforced polymer–matrix composite. Composites Science and Technology 65:537-549
Li T, Huang Z, Suo Z, Lacour SP, Wagner S (2004). Stretchability of thin metal films on elastomer substrates. Applied Physics Letters 85:3435-3437
Li T, Huang ZY, Xi ZC, Lacour SP, Wagner S, Suo Z (2005b). Delocalizing strain in a thin metal film on a polymer substrate. Mechanics of Materials 37:261-273
Li T, Suo Z (2007a). Ductility of thin metal films on polymer substrates modulated by interfacial adhesion. International Journal of Solids and Structures 44:1696-1705
Li XF, Zhang KF, Wang GF (2007b). Preparation and tensile properties of amorphous Fe78Si9B13/nano-Ni laminated composite. Materials Letters 61:4901-4905
Liechti KM, Chai YS (1991). Biaxial Loading Experiments for Determining Interfacial Fracture Toughness. Journal of Applied Mechanics 58:680-687
Lin YS, Liu HM (2008). Enhanced adhesion of plasma-sputtered copper films on polyimide substrates by oxygen glow discharge for microelectronics. Thin Solid Films 516:1773-1780
Lu K, Lu J (2004). Nanostructured surface layer on metallic materials induced by surface mechanical attrition treatment. Materials Science and Engineering: A 375–377:38-45
Lu N, Suo Z, Vlassak JJ (2010). The effect of film thickness on the failure strain of polymer-supported metal films. Acta Materialia 58:1679-1687
Lu N, Wang X, Suo Z, Vlassak J (2007). Metal films on polymer substrates stretched beyond 50%. Applied Physics Letters 91:221909
Lu N, Wang X, Suo Z, Vlassak J (2009). Failure by simultaneous grain growth, strain localization, and interface debonding in metal films on polymer substrates. Journal of Materials Research 24:379-385
Lumelsky VJ, Shur MS, Wagner S (2001). Sensitive skin. Sensors Journal, IEEE 1:41-51

Ma Q, Fujimoto H, Flinn P, Jain V, Adibi-Rizi F, Moghadam F, Dauskardt RH (1995). Quantitative Measurement of Interface Fracture Energy in Multi-Layer Thin Film Structures. MRS Online Proceedings Library Archive 391:91

Macionczyk F, Brückner W (1999). Tensile testing of AlCu thin films on polyimide foils. Journal of Applied Physics 86:4922-4929

McHenry ME, Willard MA, Laughlin DE (1999). Amorphous and nanocrystalline materials for applications as soft magnets. Progress in Materials Science 44:291-433

Mello AW, Liechti KM (2004). The Effect of Self-Assembled Monolayers on Interfacial Fracture. Journal of Applied Mechanics 73:860-870

Misra A, Hirth JP, Hoagland RG (2005). Length-scale-dependent deformation mechanisms in incoherent metallic multilayered composites. Acta Materialia 53:4817-4824

Moffat TP, Stafford GR, Hall DE (1993). Pitting Corrosion of Electrodeposited Aluminum-Manganese Alloys. Journal of The Electrochemical Society 140:2779-2786

Mraied H, Cai W, Sagüés A (2016a). Corrosion resistance of Al and Al–Mn thin films. Thin Solid Films 615:391-401

Mraied H, Tran TH, Cai WJ (2016b). Fabrication and deformation of aluminum-manganese microsandwich structure. Journal of Materials Research 31:480-487

Mukai T, Kanahashi H, Miyoshi T, Mabuchi M, Nieh TG, Higashi K (1999). Experimental study of energy absorption in a close-celled aluminum foam under dynamic loading. Scripta Materialia 40:921-927

Newman Jr JC, James MA, Zerbst U (2003). A review of the CTOA/CTOD fracture criterion. Engineering Fracture Mechanics 70:371-385

Nieh TG, Barbee TW, Wadsworth J (1999). Tensile properties of a free-standing Cu/Zr nanolaminate (or compositionally-modulated thin film). Scripta Materialia 41:929-935

Niu RM, Liu G, Wang C, Zhang G, Ding XD, Sun J (2007). Thickness dependent critical strain in submicron Cu films adherent to polymer substrate. Applied Physics Letters 90:-

Odette GR, Chao BL, Sheckherd JW, Lucas GE (1992). Ductile phase toughening mechanisms in a TiAl・TiNb laminate composite. Acta Metallurgica et Materialia 40:2381-2389

Oh H (2004). Accurate mode-separated energy release rates for delamination cracks. Journal of Computational Physics 193:86-114

Ortiz M, Pandolfi A (1999). Finite-deformation irreversible cohesive elements for three-dimensional crack-propagation analysis. International Journal for Numerical Methods in Engineering 44:1267-1282

Pandya KC, Williams JG (2000a). Cohesive zone modelling of crack growth in polymers Part 1 –Experimental measurement of cohesive law. Plastics, Rubber and Composites 29:439-446

Pandya KC, Williams JG (2000b). Measurement of cohesive zone parameters in tough polyethylene. Polymer Engineering & Science 40:1765-1776

Park IS, Ahn EC, Yu J, Lee HY (2000). Cohesive failure of the Cu/polyimide system. Materials Science and Engineering: A 282:137-144

Park IS, Yu J (1998). An X-ray study on the mechanical effects of the peel test in a Cu/Cr/polyimide system. Acta Materialia 46:2947-2953

Park K, Paulino GH (2013). Cohesive Zone Models: A Critical Review of Traction-Separation Relationships Across Fracture Surfaces. Applied Mechanics Reviews 64:060802-060802

Pei HJ, Lee CJ, Du XH, Chang YC, Huang JC (2011). Tension behavior of metallic glass coating on Cu foil. Materials Science and Engineering: A 528:7317-7322

Phan M, Peng H (2008). Giant magnetoimpedance materials: Fundamentals and applications. Progress in Materials Science 53:323-420
Rice JR (1988). Elastic Fracture Mechanics Concepts for Interfacial Cracks. Journal of Applied Mechanics 55:98-103
Rice JR, Sih GC (1965). Plane Problems of Cracks in Dissimilar Media. Journal of Applied Mechanics 32:418-423
Rice JR, Thomson R (1974). Ductile versus brittle behaviour of crystals. Philos Mag 29:73-97
Ritchie RO (2011). The conflicts between strength and toughness. Nat Mater 10:817-822
Ruan SY, Schuh CA (2009). Electrodeposited Al-Mn alloys with microcrystalline, nanocrystalline, amorphous and nano-quasicrystalline structures. Acta Materialia 57:3810-3822
Ruan SY, Torres KL, Thompson GB, Schuh CA (2011). Gallium-enhanced phase contrast in atom probe tomography of nanocrystalline and amorphous Al-Mn alloys. Ultramicroscopy 111:1062-1072
Scheider I, Brocks W (2003). Simulation of cup-cone fracture using the cohesive model. Engineering Fracture Mechanics 70:1943-1961
Schuh CA, Hufnagel TC, Ramamurty U (2007). Mechanical behavior of amorphous alloys. Acta Materialia 55:4067-4109
Shindo Y, Sato T, Narita F, Sanada K (2008). Mode II Interlaminar Fracture and Damage Evaluation of GFRP Woven Laminates at Cryogenic Temperatures using the 4ENF Specimen. Journal of Composite Materials 42:1089-1101
Shirangi MH, Gollhardt A, Fischer A, Müller WH, Michel B (2008). Investigation of fracture toughness and displacement fields of Copper/Polymer interface using image correlation technique. Proc 41st International Symposium on Microelectronics
Sørensen BF (2002). Cohesive law and notch sensitivity of adhesive joints. Acta Materialia 50:1053-1061
Sørensen BF, Jacobsen TK (2003). Determination of cohesive laws by the J integral approach. Engineering Fracture Mechanics 70:1841-1858
Sun CT, Qian W (1997). The use of finite extension strain energy release rates in fracture of interfacial cracks. International Journal of Solids and Structures 34:2595-2609
Swallowe GM (1999). Mechanical properties and testing of polymers. Springer Science and Business Media Dordrecht
Tran HT et al. (2016). Anisotropic Mechanical and Giant Magneto-Impedance Properties of Cobalt-Rich Amorphous Ribbons. Journal of Electronic Materials 45:2278-2285
Tran HT, Shirangi MH, Pang X, Volinsky AA (2013). Temperature, moisture and mode-mixity effects on copper leadframe/EMC interfacial fracture toughness. International Journal of Fracture 185:115-127
Tran HT, Shirangi MH, Pang X, Volinsky AA (2014). Temperature, moisture and mode-mixity effects on copper leadframe/EMC interfacial fracture toughness. International Journal of Fracture 185:115-127
Trias D (2012). Fracture mechanics. Universitat de Girona, Catalonia, Spain
Tummala R (2001). Fundamentals of Microsystems Packaging. McGraw Hill, New York
Tvergaard V (1990). Effect of fiber debonding in a whisker-reinforced metal. Materials Science and Engineering A 125:203-213

Tvergaard V, Hutchinson JW (1992). The relation between crack growth resistance and fracture process parameters in elastic-plastic solids. Journal of the Mechanics and Physics of Solids 40:1377-1397

Tvergaard V, Hutchinson JW (1993). The influence of plasticity on mixed-mode interface toughness. Journal of the Mechanics and Physics of Solids 41:1119-1135

van Hal BAE, Peerlings RHJ, Geers MGD, van der Sluis OD (2007). Cohesive zone modeling for structural integrity analysis of IC interconnects. Microelectronics Reliability 47:1251-1261

Varias AG, Suo Z, Shih CF (1991). Ductile failure of a constrained metal foil. Journal of the Mechanics and Physics of Solids 39:963-986

Verhulp E, Rietbergen Bv, Huiskes R (2004). A three-dimensional digital image correlation technique for strain measurements in microstructures. Journal of Biomechanics 37:1313-1320

Volinsky AA, Tymiak NI, Kriese MD, Gerberich WW, Hutchinson JW (1998). Quantitative Modeling and Measurement of Copper Thin Film Adhesion. MRS Proceedings 539

Wada T, Zhang T, Inoue A (2002). Formation, Thermal Stability and Mechanical Properties in Zr-Al-Co Bulk Glassy Alloys. MATERIALS TRANSACTIONS 43:2843-2846

Wagner S, Lacour SP, Jones J, Hsu P-hI, Sturm JC, Li T, Suo Z (2004). Electronic skin: architecture and components. Physica E: Low-dimensional Systems and Nanostructures 25:326-334

Wang CH (1996). Introduction to Fracture Mechanics. DSTO, Australia

Wang J, Anderson PM (2005). Pinch-off maps for the design of morphologically stable multilayer thin films with immiscible phases. Acta Materialia 53:5089-5099

Wang J, Huang L, Zhu S, Li Q, Guan S, Zhang T (2013). Glass-forming ability, fragility parameter, and mechanical properties of Co–Ir–Ta–B amorphous alloys. Journal of Alloys and Compounds 576:375-379

Wang JS, Suo Z (1990). Experimental determination of interfacial toughness curves using Brazil-nut-sandwiches. Acta Metallurgica et Materialia 38:1279-1290

Wang WH (2009). Bulk Metallic Glasses with Functional Physical Properties. Advanced Materials 21:4524-4544

Was GS, Foecke T (1996). Deformation and fracture in microlaminates. Thin Solid Films 286:1-31

Wattrisse B, Chrysochoos A, Muracciole JM, Némoz-Gaillard M (2001). Analysis of strain localization during tensile tests by digital image correlation. Experimental Mechanics 41:29-39

Wei Y, Hutchinson JW (1997). Nonlinear delamination mechanics for thin films. Journal of the Mechanics and Physics of Solids 45:1137-1159

Weidong X, Sitaraman SK (2003). Investigation of interfacial delamination of a copper-epoxy interface under monotonic and cyclic loading: experimental characterization. IEEE Transactions on Advanced Packaging 26:447-452

Wells AA (1963). Application of fracture mechanics at and beyond general yielding. British Welding Journal 10:563–570

Williams ML (1959). The stresses around a fault or crack in dissimilar media. Bulletin of the Seismological Society of America 49:199-204

Wittmann FH, Rokugo K, Brühwiler E, Mihashi H, Simonin P (1988). Fracture energy and strain softening of concrete as determined by means of compact tension specimens. Materials and Structures 21:21-32

Wong CKY, Gu H, Xu B, Yuen MMF (2006). A new approach in measuring Cu/EMC adhesion strength by AFM. IEEE Transactions on Components and Packaging Technologies 29:543-550

Wu K, Zhang JY, Zhang P, Wang YQ, Liu G, Zhang GJ, Sun J (2014). Fracture behavior and adhesion energy of nanostructured Cu/Mo multilayer films. Materials Science and Engineering: A 613:130-135

Xiang Y, Li T, Suo ZG, Vlassak JJ (2005). High ductility of a metal film adherent on a polymer substrate. Applied Physics Letters 87

Xu W, Lu TJ, Wang F (2010). Effects of interfacial properties on the ductility of polymer-supported metal films for flexible electronics. International Journal of Solids and Structures 47:1830-1837

Xu W, Yang JS, Lu TJ (2011). Ductility of thin copper films on rough polymer substrates. Materials & Design 32:154-161

Xu XP, Needleman A (1994). Numerical simulations of fast crack growth in brittle solids. Journal of the Mechanics and Physics of Solids 42:1397-&

Yu DYW, Spaepen F (2004). The yield strength of thin copper films on Kapton. Journal of Applied Physics 95:2991-2997

Zbib HM, Overman CT, Akasheh F, Bahr D (2011). Analysis of plastic deformation in nanoscale metallic multilayers with coherent and incoherent interfaces. International Journal of Plasticity 27:1618-1639

Zerbst U, Heinimann M, Donne CD, Steglich D (2009). Fracture and damage mechanics modelling of thin-walled structures – An overview. Engineering Fracture Mechanics 76:5-43

Zhang GP, Sun KH, Zhang B, Gong J, Sun C, Wang ZG (2008a). Tensile and fatigue strength of ultrathin copper films. Materials Science and Engineering: A 483–484:387-390

Zhang JY, Liu G, Sun J (2014). Self-toughening crystalline Cu/amorphous Cu–Zr nanolaminates: Deformation-induced devitrification. Acta Materialia 66:22-31

Zhang JY et al. (2011). Length-scale-dependent deformation and fracture behavior of Cu/X multilayers: The constraining effects of the ductile phase on the brittle phase. Acta Materialia 59:7368-7379

Zhang Z, Li T (2008b). Effects of grain boundary adhesion and grain size on ductility of thin metal films on polymer substrates. Scripta Materialia 59:862-865

Zhou J, Liu D, Shao L-Y, Wang Z-L (2013a). Application of Digital Image Correlation to Measurement of Packaging Material Mechanical Properties. Mathematical Problems in Engineering 2013:8

Zhou W, Tao Y, Liu L, Kong L, Li J, Zhou Y (2013b). Microstructure and Mechanical Properties of Cu-Zr-Al Bulk Metallic Glass with Addition of Co. Materials Transactions 54:286-290

Zhu X, Joyce J (2012). Review of fracture toughness (G, K, J, CTOD, CTOA) testing and standardization. Engineering Fracture Mechanics 85:1-46

Zhu Y, Liechti KM, Ravi-Chandar K (2009). Direct extraction of rate-dependent traction–separation laws for polyurea/steel interfaces. International Journal of Solids and Structures 46:31-51

APPENDIX A: DEFORMATION OF ALUMINUM–MANGANESE MICROSANDWICH STRUCTURE

A.1 Simulation of Aluminum–Manganese Microsandwich Structure Under Microindentation

In the paper (Mraied et al. 2016b), one-step electrodeposition procedure to synthesize Al-Mn microsandwichs using a porous polycarbonate membrane template ionic liquid in RT was proposed. Together with nano- and micro-indentation experiments, to understand more about the deformation behavior of the two microsandwich structures, FE models were utilized with the commercial software Ansys Workbench. The geometry properties were averagely taken from the experimental data. Specifically, the size of the upper and lower plates is of 70x70x11 μm and the pillars have the height of 27.6 μm and the diameter of 5 μm. The distances between the pillars are all 10 μm. The indenter was constructed as a sphere of 4 mm diameter and the material of Al_2O_3. The material properties of Al_2O_3 was taken from literature while Al-9 at.% Mn and Al-26 at.% Mn are assumed (rule of mixture) to be elastic with the elastic moduli of 81.5 GPa, 103 GPa and Poisson's ratios of 0.301, 0.318, respectively, and the above mentioned mass densities. The behaviors of the materials were assumed to be elastic-perfectly plastic with the yield strength of 863 MPa and 2050 MPa (measured by nanoindentation), respectively. The material properties used in the simulations are listed in Table A.1.

The two structures were loaded and unloaded with the same force of 0.81 N, which corresponds to the experimental loading with the same size. The fine mesh was created at the

contact area between the indenter and the top plates of the micro-pillar structures. Convergence analysis was performed to get the most accurate results with the least computational expense. The number of elements in the two structures are 92387 for Al-9 at.% Mn and 131185 for Al-26 at.% Mn. The FEA results presented in Fig. A.2 show that under the same loading, the Al-9 at.% Mn structure experienced a large plastic deformation (Fig. A.2(a)) while the Al-26 at.% Mn structure was elastically deformed and mainly on the top face (Fig. A.2(b)). In both crystalline and amorphous structures, the maximum equivalent stresses and the maximum shear strains (not shown here) occur at the face/core interface, which is in agreement with the pillar delamination location observed in experiments (Fig. A.1). Moreover, the absorption energy per unit volume of the Al-9 at.% Mn structure was estimated 43.2 MJ/m^3 which is much higher than that of aluminum foams (e.g. $\approx$ 4 MJ/m^3 in reference (Mukai et al. 1999)), aluminum honeycomb foam (e.g. $\approx$ 12 MJ/m^3 in reference (Ruan et al. 2011)) and new lattice structures (e.g. 1–20 MJ/m^3 in reference (Ruan et al. 2009; Ruan et al. 2011)) under the same range of strains.

A.2 Tables and Figures

Table A.1 Summary of composition and properties of microsandwiches used in FEA. Elastic constants were estimated from rule of mixture. Credit (Mraied et al. 2016b).

Microsandwich composition	Elastic modulus (GPa)	Poisson's ratio	Yield strength (MPa)	Plastic zone size (μm)	Core yield load (N)	Skin fracture load (N)
Al–9 at.% Mn	81.1	0.34	863	300	18.2	23.4
Al–26 at.% Mn	101.6	0.32	2050	300	43.1	55.6

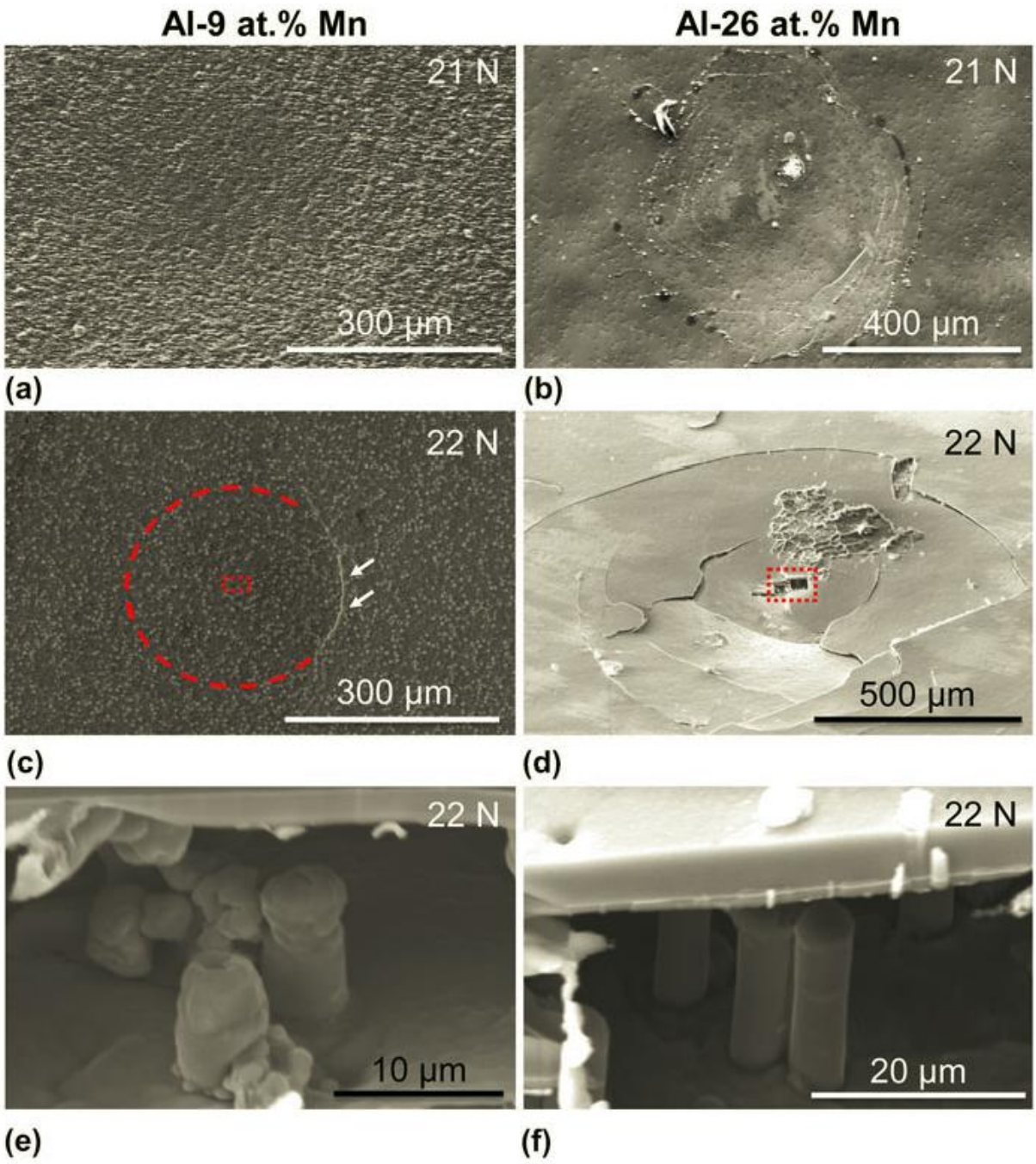

Figure A.1 SEM images of (a) and (b) surface and (c) and (d) cross-section of Al–9 at.% Mn and Al–26 at.% Mn microsandwiches after microindentation. Images (e) and (f) are taken from the box areas in (c) and (d), respectively. Credit (Mraied et al. 2016b).

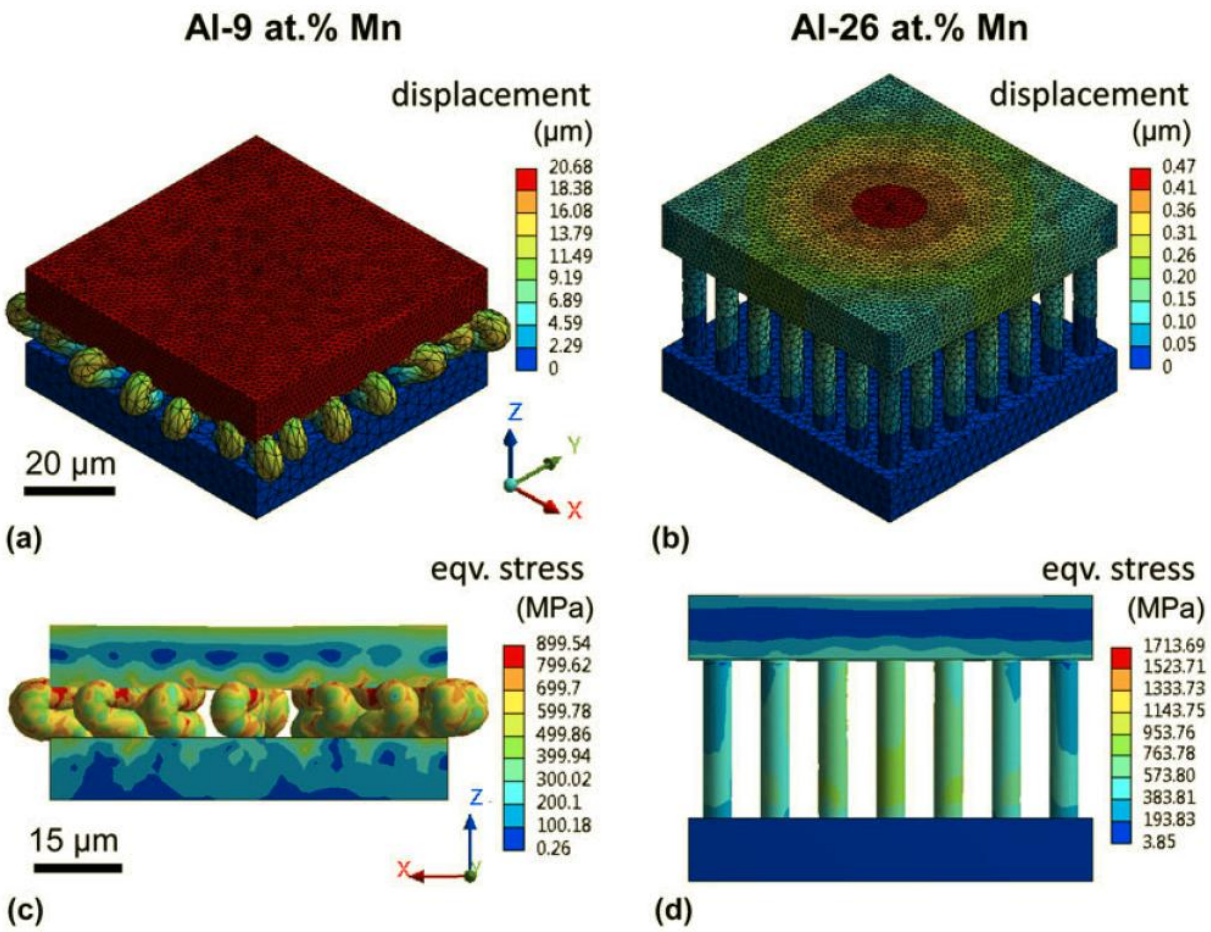

Figure A.2 FEA predicted (a) and (b) displacement, and (c) and (d) equivalent stress of Al–9 at.% Mn and Al–26 at.% Mn microsandwiches after microindentation. Credit (Mraied et al. 2016b).

APPENDIX B: ANISOTROPIC MECHANICAL AND GIANT MAGNETO-IMPEDANCE PROPERTIES OF COBALT-RICH AMORPHOUS RIBBONS

B.1 Mechanical Properties of $Co_{69}Fe_4Ni_1Mo_2B_{12}Si_{12}$ Amorphous Ribbons

A comparative study was performed on the mechanical and giant magneto-impedance (GMI) properties in the longitudinal and transverse directions of $Co_{69}Fe_4Ni_1Mo_2B_{12}Si_{12}$ amorphous ribbons. Both mechanical and GMI properties were found to be anisotropic. Kerr microscopy shows the presence of a stripe-type domain structure with the magnetic easy axis parallel to the longitudinal direction. The fracture strength, elastic modulus, and fracture toughness in the transverse direction was higher than those in the longitudinal direction. A larger GMI response was achieved in the transverse direction at a frequency range where both the domain wall motion and spin rotation dominantly contributed to the effective permeability and hence the magneto-impedance. The current study paves the way for designing Co-rich amorphous ribbons as desirable components in electronics such as magnetic sensors.

Mechanical properties of the ribbon were obtained from tensile testing using a delamination testing system (DTS from National Instruments group) under a constant strain rate of 1.67×10^{-4} s^{-1} at room temperature. Two different sample geometries, dog-bone and pre-cracked rectangle, were used for the tensile testing. Dog-bone samples with 2×20 mm^2 gauge area were used to measure ductility, fracture strength, and elastic modulus. Fracture toughness was measured using rectangular samples with 2 mm edge cracks at the middle of the gauge area (4×40 mm^2). Prior to the tensile testing, the pre-cracked samples were gripped with flat clamps

on both ends to ensure uniform stress distribution along the width of the specimen. This step is critical to prevent buckling that may appear due to the high stress concentration at the crack tip.

All results reported here were obtained by averaging from four separate tests. DIC method was used to obtain an accurate measurement of the strain. All samples were sprayed with fine ink speckles on the surface prior to testing. The movements of these markers were then tracked with a high definition camera at a frame rate of ~ 30 FPS. The strain was then calculated using a Matlab routine developed by Christoph Eberl et al. at Johns Hopkins University, USA (Bing et al. 2009; Verhulp et al. 2004; Wattrisse et al. 2001; Zhou et al. 2013a). Fig. B.1 shows the typical stress-strain curves of longitudinal and transverse dog-bone samples with snapshots of the transverse sample at different stages of the test. From these tests, the elongation, fracture strength and elastic modulus of the longitudinal and transverse samples were measured, as plotted in Fig. B.3(a-c). It can be seen that while the two samples exhibit comparable elongation, both the fracture strength and elastic modulus is higher in the transverse direction.

Fig. B.2 shows typical force-displacement curves of longitudinal and transverse pre-cracked samples, where the location of the pre-crack is marked by the red ellipse on the inserted images. Since the material is brittle in both directions, the fracture toughness of the ribbon was determined using linear elastic fracture mechanics. The mode I SIF K_{Ic} (fracture toughness) is calculated as (Anderson 2005):

$$K_{\mathrm{Ic}} = 1.12 * \sigma\sqrt{\pi a}, \tag{B.1}$$

where σ is the fracture stress and a is the pre-crack length, as shown in Fig. B.3(d). It can be seen that both the fracture stress and fracture toughness were higher in the transverse sample than the longitudinal one.

Mechanical properties of Fe- or Co-based amorphous ferromagnetic materials are commonly obtained by compression or hardness tests, while those from tensile tests are few (Inoue et al. 1995; Inoue et al. 2003; Kuan et al. 2013; Wada et al. 2002; Wang et al. 2013; Wang et al. 2014; Zhou et al. 2013b). From Fig. B.3, in comparison with the longitudinal configuration, the transverse configuration has the dominance in almost all the mechanical properties namely fracture strength (2,689 MPa and 2,592 MPa) (tensile strength of $Co_{68.15}Fe_{4.35}Si_{12.25}B_{15.25}$ (at%) amorphous microwires was reported from 1,145 to 2,457 MPa (Wang et al. 2014)), elastic modulus (177 GPa and 165 GPa) except the comparable elongation (1.57% and 1.61%). Moreover, from the fracture strength and elongation data in Fig. B.3, it can be clearly seen that the toughness (different from fracture toughness) of the transverse configuration is also higher than that of the longitudinal one.

B.2 Tables and Figures

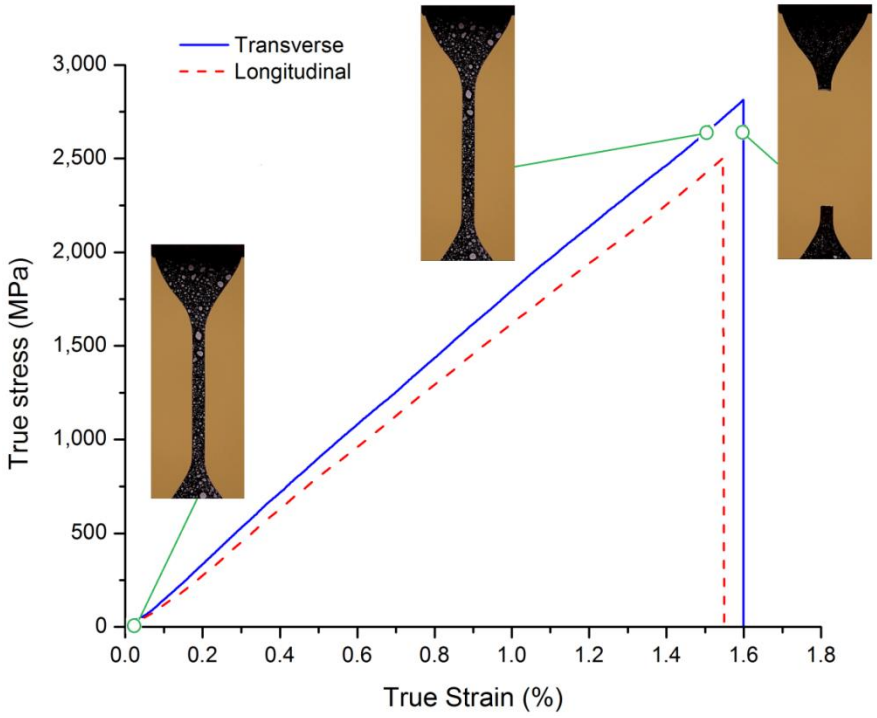

Figure B.1 Typical stress-strain curves of longitudinal and transverse dog-bone samples. Inset images show snapshots of transverse sample at different stages of the test. Credit (Tran et al. 2016).

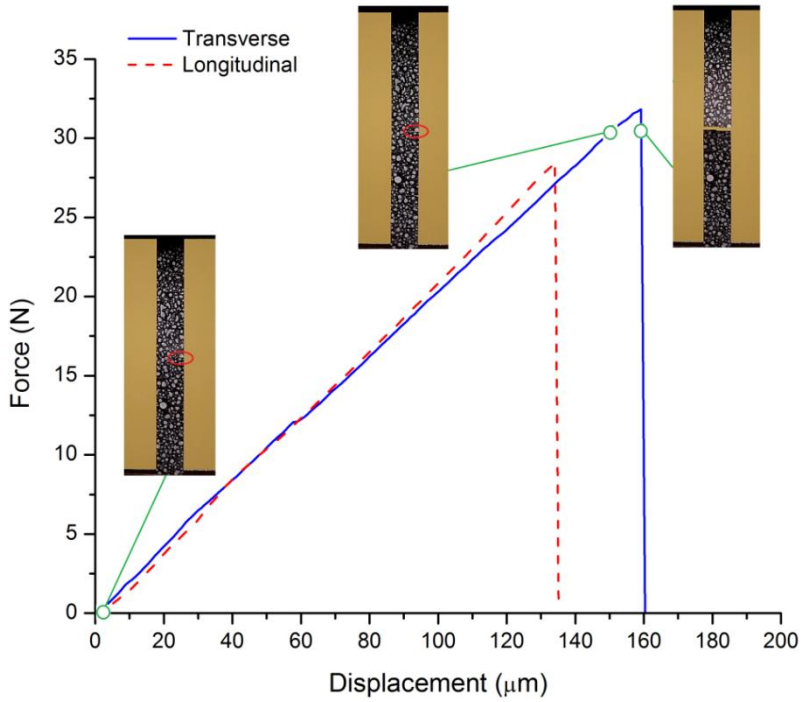

Figure B.2 Force-displacement curves of a longitudinal and a transverse pre-cracked rectangular samples with insets being the images of the sample at the indicated times (the ellipses indicate the pre-crack). Credit (Tran et al. 2016).

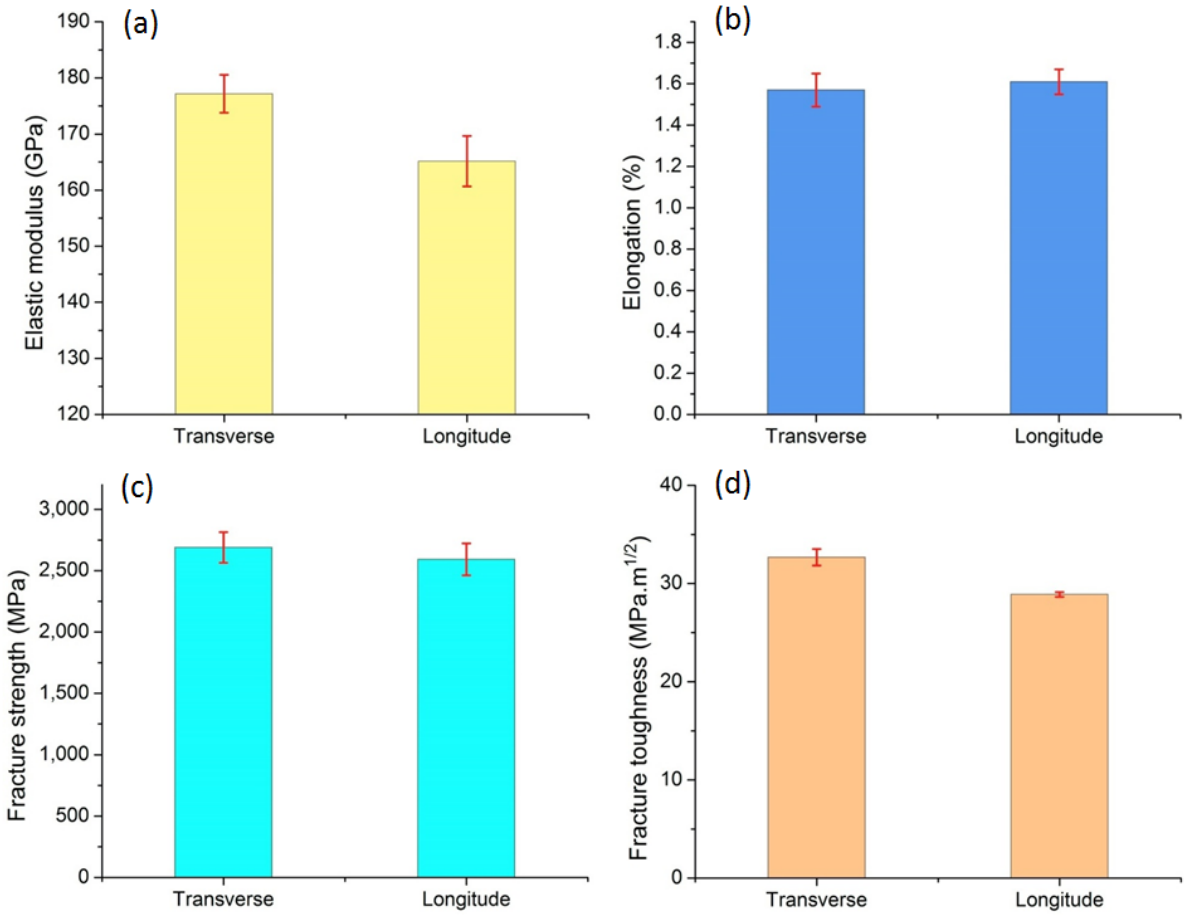

Figure B.3 Mechanical properties of the ribbon in the two configurations. Credit (Tran et al. 2016).

APPENDIX C: ABBREVIATIONS

Unless otherwise specified, the following abbreviations are used in this dissertation:

4ENF	four point-bend end-notched flexure
4PB	four point bending
APDL	Ansys parametric design language
CZM	cohesion zone model
DIC	digital image correlation
EDS	energy dispersive spectra
EMC	epoxy molding compound
ERR	energy release rate
EPFM	elasto-plastic fracture mechanics
FEA	finite element analysis
FEM	finite element method
GMI	giant magneto-impedance
LEFM	linear elastic fracture mechanics
PI	polyimide
SAD	selected area diffraction
SEM	scanning electron microscopy
SIF	stress intensity factor
TEM	transmission electron microscopy

VCE	virtual crack extension
VCCT	virtual crack closure technique

APPENDIX D: COPYRIGHT PERMISSIONS

Excerpts from the license agreements for use of materials from previously published articles are listed as the followings. The first copyright permission is for figures 2.8, 2.9, 2.10, 2.11, 2.12 and 2.14. The second copyright permission is for tables 5.1, 5.2, 5.3 and figures 5.1, 5.2, 5.3, 5.4, 5.5, 5.7, 5.8, 5.9, 5.10, 5.11, 5.12, 5.13. The third copyright permission is for table A.1 and figures A.1, A.2. The last copyright permission is for figures B.1, B.2 and B.3.

Dear Mr. Tran:
It is our pleasure to grant you permission to use the ASME figures only:

- **Figures 3,4,7** from "Virtual crack closure technique: History, approach, and applications," by Ronald Krueger, Appl. Mech. Rev 57(2), 2004

- **Figures 1,2** from "Cohesive Zone Models: A Critical Review of Traction-Separation Relationships Across Fracture Surfaces," by Kyoungsoo Park and Glaucio H. Paulino, Appl. Mech. Rev 64(6), 2013

cited in your letter for inclusion in a PhD Dissertation entitled Experimental and computational study on fracture mechanics of multilayered structures to be published by University of South Florida.

Permission is granted for the specific use as stated herein and does not permit further use of the materials without proper authorization. Proper attribution must be made to the author(s) of the materials. As is customary, we request that you ensure full acknowledgment of this material, the author(s), source and ASME as original publisher.

Many thanks for your interest in ASME publications.

Sincerely,

Beth Darchi
Publishing Administrator
ASME
2 Park Avenue, 6th Floor
New York, NY 10016-5990
Tel 1.212.591.7700
darchib@asme.org

SPRINGER LICENSE
TERMS AND CONDITIONS

Oct 29, 2016

This Agreement between Hai T Tran ("You") and Springer ("Springer") consists of your license details and the terms and conditions provided by Springer and Copyright Clearance Center.

License Number	3978011084244
License date	Oct 29, 2016
Licensed Content Publisher	Springer
Licensed Content Publication	International Journal of Fracture
Licensed Content Title	Temperature, moisture and mode-mixity effects on copper leadframe/EMC interfacial fracture toughness
Licensed Content Author	Hai T. Tran
Licensed Content Date	Jan 1, 2013
Licensed Content Volume Number	185
Licensed Content Issue Number	1
Type of Use	Thesis/Dissertation
Portion	Full text
Number of copies	1
Author of this Springer article	Yes and you are the sole author of the new work
Order reference number	
Title of your thesis / dissertation	Experimental and computational study on fracture mechanics of multilayered structures
Expected completion date	Oct 2016
Estimated size(pages)	150
Requestor Location	Hai T Tran 14217 Les Palms Circle A. 201 TAMPA, FL 33613 United States Attn: Hai T Tran
Billing Type	Invoice
Billing Address	Hai T Tran 14217 Les Palms Circle A. 201 TAMPA, FL 33613 United States Attn: Hai T Tran

CAMBRIDGE UNIVERSITY PRESS LICENSE
TERMS AND CONDITIONS

Sep 17, 2016

This Agreement between Hai T Tran ("You") and Cambridge University Press ("Cambridge University Press") consists of your license details and the terms and conditions provided by Cambridge University Press and Copyright Clearance Center.

License Number	3951181203749
License date	Sep 17, 2016
Licensed Content Publisher	Cambridge University Press
Licensed Content Publication	Journal of Materials Research
Licensed Content Title	Fabrication and deformation of aluminum–manganese microsandwich structure
Licensed Content Author	Hesham Mraied, Thanh Hai Tran, Wenjun Cai
Licensed Content Date	Feb 11, 2016
Licensed Content Volume Number	31
Licensed Content Issue Number	4
Start page	480
End page	487
Type of Use	Dissertation/Thesis
Requestor type	Author
Portion	Text extract
Number of pages requested	2
Author of this Cambridge University Press article	Yes
Author / editor of the new work	Yes
Order reference number	
Territory for reuse	North America Only
Title of your thesis / dissertation	Experimental and computational study on fracture mechanics of multilayered structures
Expected completion date	Oct 2016
Estimated size(pages)	150
Requestor Location	Hai T Tran 14217 Les Palms Circle A. 201 TAMPA, FL 33613 United States Attn: Hai T Tran
Publisher Tax ID	GB823847609
Billing Type	Invoice

Billing Address	Hai T Tran 14217 Les Palms Circle A. 201 TAMPA, FL 33613 United States Attn: Hai T Tran
Total	0.00 USD

Terms and Conditions

TERMS & CONDITIONS

Cambridge University Press grants the Licensee permission on a non-exclusive non-transferable basis to reproduce, make available or otherwise use the Licensed content 'Content' in the named territory 'Territory' for the purpose listed 'the Use' on Page 1 of this Agreement subject to the following terms and conditions.

1. The License is limited to the permission granted and the Content detailed herein and does not extend to any other permission or content.
2. Cambridge gives no warranty or indemnity in respect of any third-party copyright material included in the Content, for which the Licensee should seek separate permission clearance.
3. The integrity of the Content must be ensured.
4. The License does extend to any edition published specifically for the use of handicapped or reading-impaired individuals.
5. The Licensee shall provide a prominent acknowledgement in the following format: author/s, title of article, name of journal, volume number, issue number, page references, , reproduced with permission.

Other terms and conditions:
v1.0

Questions? customercare@copyright.com or +1-855-239-3415 (toll free in the US) or +1-978-646-2777.

SPRINGER LICENSE
TERMS AND CONDITIONS

Sep 17, 2016

This Agreement between Hai T Tran ("You") and Springer ("Springer") consists of your license details and the terms and conditions provided by Springer and Copyright Clearance Center.

License Number	3951190125947
License date	Sep 17, 2016
Licensed Content Publisher	Springer
Licensed Content Publication	Journal of Electronic Materials
Licensed Content Title	Anisotropic Mechanical and Giant Magneto-Impedance Properties of Cobalt-Rich Amorphous Ribbons
Licensed Content Author	H. T. Tran
Licensed Content Date	Jan 1, 2016
Licensed Content Volume Number	45
Licensed Content Issue Number	4
Type of Use	Thesis/Dissertation
Portion	Figures/tables/illustrations
Number of figures/tables /illustrations	3
Author of this Springer article	Yes and you are the sole author of the new work
Order reference number	
Original figure numbers	Figures 2, 3, 4
Title of your thesis / dissertation	Experimental and computational study on fracture mechanics of multilayered structures
Expected completion date	Oct 2016
Estimated size(pages)	150
Requestor Location	Hai T Tran 14217 Les Palms Circle A. 201 TAMPA, FL 33613 United States Attn: Hai T Tran
Billing Type	Invoice
Billing Address	Hai T Tran 14217 Les Palms Circle A. 201 TAMPA, FL 33613 United States Attn: Hai T Tran